GEODESY IN ANTARCTICA: A PILOT STUDY BASED ON THE TAMDEF GPS NETWORK, VICTORIA LAND, ANTARCTICA

by

Guadalupe Esteban Vazquez Becerra

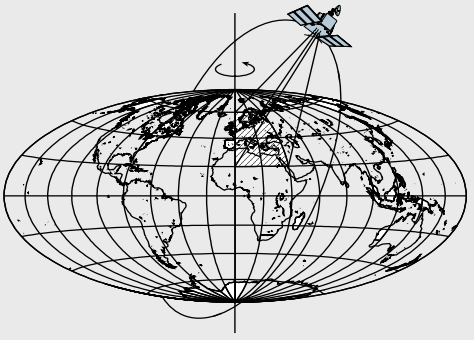

Report No. 492

Geodetic Science and Surveying

The Ohio State University
Columbus, Ohio 43210

July 2009

GEODESY IN ANTARCTICA: A PILOT STUDY BASED ON THE TAMDEF GPS NETWORK, VICTORIA LAND, ANTARCTICA

by

Guadalupe Esteban Vázquez Becerra

Report No. 492

Geodetic Science and Surveying

The Ohio State University
Columbus, Ohio 43210

July 2009

ABSTRACT

The objective of the research presented in this report is a combination of practical and theoretical problems to investigate unique aspects of GPS (Global Positioning System) geodesy in Antarctica. This is derived from a complete analysis of a GPS network called TAMDEF (Trans Antarctic Mountains Deformation), located in Victoria Land, Antarctica. In order to permit access to the International Terrestrial Reference Frame (ITRF), the McMurdo (MCM4) IGS (The International GNSS Service for Geodynamics, formerly the International GPS Service) site was adopted as part of the TAMDEF network. The following scientific achievements obtained from the cited analysis will be discussed as follows:

(1) The GPS data processing for the TAMDEF network relied on the PAGES (Program for Adjustment of GPS Ephemerides) software that uses the double-differenced iono-free linear combination, which helps removing partial of bias (mm level) in the final positioning. (2) To validate the use of different antenna types in TAMDEF, an antenna testing experiment was conducted using the National Geodetic Survey (NGS) antenna calibration data, appropriate for each antenna type. Sub-daily and daily results from the antenna testing are at the sub-millimeter level, based on the fact that 24-hour solutions were used to average any possible bias. (3) A potential contributor that might have an impact on the TAMDEF stations positioning is the pseudorange multipath effect; thus, the root mean squared variations were estimated and analyzed in order to identify the most and least affected sites. MCM4 was found to be the site with highest multipath, and this is not good at all, since MCM4 is the primary ITRF access point for this part of Antarctica. Additionally, results from the pseudorange multipath can be used for further data cleaning to improve positioning results. (4) The Ocean Tide Modeling relied on the use of two models: CATS02.01 (Circum Antarctic Tidal Simulation) and TPXO6.2 (TOPEX/Poseidon) to investigate which model suits the Antarctic conditions best and its effect on the vertical coordinate component at the TAMDEF sites. (5) The scatter for the time-series results of the coordinate components for the TAMDEF sites are smaller when processed with respect to the Antarctic tectonic plate (Case I), in comparison with the other tectonic plates outside Antarctica (Case II-IV). Also, the seasonal effect due to the time-series seen in the TAMDEF sites with longer data span are site dependent; thus, data processing is not the reason for these effects. (6) Furthermore, the results coming from a homogeneous global network with coordinates referred and transformed to the ITRF2000 at epoch 2005.5 reflect the quality of the solution, obtained when processing TAMDEF network data with respect to the Antarctic tectonic plate. (7) An optimal data reduction strategy was developed, based on three different troposphere models and mapping functions, tested and used to estimate the total wet zenith delay (TWZD) which later was transformed to precipitable water vapor (PWV). PWV was estimated from GPS measurements and validated with a numerical weather model, AMPS (Antarctic Mesoscale Prediction System) and radiosonde PWV. Additionally, to validate the TWZD estimates at the MCM4 site before their conversion into the GPS PWV, these estimates were directly compared to TWZD computed by the CDDIS (Crustal Dynamics Data Information System) analysis center. (8) The results from the Least-Squares

adjustment with Stochastic Constraints (SCLESS) as performed with PAGES are very comparable (mm-level) to those obtained from the alternative adjustment approaches: MINOLESS (Minimum-Norm Least-Squares adjustment); Partial-MINOLESS (Partial Minimum-Norm Least-Squares adjustment), and BLIMPBE (Best Linear Minimum Partial-Bias Estimation). Based on the applied network adjustment models within the Antarctic tectonic plate (Case I), it can be demonstrated that the GPS data used are clean of bias after proper care has been taken of ionosphere, troposphere, multipath, and some other sources that affect GPS positioning.

Overall, it can be concluded that no suspected of bias was present in the obtained results, thus, GPS is indeed capable of capturing the signal which can be used for further geophysical interpretation within Antarctica.

PREFACE

This report was prepared by Guadalupe Esteban Vázquez Becerra, a graduate student, Department of Civil and Environmental Engineering and Geodetic Science, under the supervision of Professor Dorota A. Grejner Brzezinska and Burkhard Schaffrin.

This research was supported by the National Council for Science and Technology (CONACYT) and partially supported by a grant from the National Science Foundation.

This report was also submitted to the Graduate School of The Ohio State University as a thesis in partial fulfillment of the requirements for the degree Doctor of Philosophy.

ACKNOWLEDGMENTS

I wish to deeply thank my adviser, Dr. Dorota A. Grejner-Brzezinska, for her intellectual support, encouragement and enthusiasm, all of which made this research possible. Her patience in correcting both my stylistic and scientific errors was invaluable.

I want to thank Dr. B. Schaffrin for his many stimulating discussions that helped to guide my application of his Least-Squares Adjustment Theorems to this research.

I thank Dr. Terry Wilson for her contribution on the geophysical aspects of this research, and Dr. Mike Willis, both from the School of Earth Sciences at OSU, and the USGS Antarctic Mapping Group for providing the TAMDEF data used for the processing and analysis.

Thanks also go to Dr. Mark Schenewerk of General Positioning LLC for his invaluable comments about optimal dealing with the various aspects of this research, which pertain to PAGES, the software he developed.

I am also grateful to Dr. Matt King of the University of Newcastle, UK and Dr. C.K. Shum (OSU) for contributing much of the Ocean Tide Modeling data used in this research.

I want to thank Dr. Matthew A. Lazzara, Meteorologist of the Space Science and Engineering Center (SSEC), University of Wisconsin-Madison (UW-Madison), and Shelley L. Knuth for providing the radiosonde-PWV data series for the McMurdo (IGS site) used in this research.

I would like to thank Dr. Ryan Fogt from Polar Meteorology group, OSU for stimulating intellectual discussions on data processing and analysis of water vapor—a topic described in this research.

I want to thank Kyle Snow for letting me use his network adjustment software for the alternative network approach addressed in this research.

I am very grateful to my sponsor “The National Council for Science and Technology” (CONACYT), for all the support they have provided for my studies.

Finally, I want to thank my wife Araceli, and my wonderful sons Paul, Derek and Dael for their support and patience. Without them and their love this work would not have been possible.

TABLE OF CONTENTS

CHAPTER 1

INTRODUCTION

1.1 Geodesy in Antarctica

Geodesy in Antarctica plays a key role in our attempt to understand a variety of factors that may have an impact on the deformation of the Antarctic continent—a topic that has been investigated for many years. In particular, there are unique geodetic aspects in the Antarctic region that merit a detailed investigation. For example, optimum measurement and data processing schemes under Antarctic conditions, selection of appropriate ocean tide model and troposphere mapping function which suits Antarctic conditions best, together with an extremely dry atmosphere characterizes Antarctica, which results in a reduction of large water vapor gradients that can cause problems in measuring height components, elsewhere.

Long-term vertical and horizontal displacement of Antarctic bedrock is driven by viscoelastic isostatic adjustment following the last glacial maximum, as well as by active rifting and volcanism in West Antarctica Rift System (WARS). Instantaneous elastic motions are also present, caused by changes in the mass balance of the East and West Antarctic ice sheets. Discriminating between these kinematic signals is essential to providing constraints for ice sheet models and for global tectonic models. While Global Positioning System (GPS) should be able to measure total bedrock motion, it is crucial to implement strategies to distinguish the various motion components in the GPS-sensed total displacement. Only when the crustal motion patterns arising from present-day ice sheet mass balance, past ice-sheet changes and tectonics can be distinguished from each other, one will be able to realize the promise of using GPS measurements to constrain the modeling of ice sheet evolution.

1.2 Motivation and background

The motivation for this research was to identify important aspects of GPS geodesy in the Antarctic continent, as well as to implement appropriate methodologies for quality assessment and optimum data processing for this unique environment. The focus of this research is to evaluate the various factors and requirements together with the development and testing of pertinent atmospheric models that may possibly have an impact on the Trans Antarctic Mountains Deformation (TAMDEF) (period 1996-2005) GPS network, located in the region throughout southern Victoria Land.

In this research the impact of these special Antarctic conditions on GPS measurement accuracy is systematically assessed. Also investigated are the sources of biases and dependence on aspects, such as incorrect determination of phase ambiguities

in fixed integer solutions, adequacy of antenna models using appropriate calibration parameters in the Antarctic environment, ocean tide modeling, multipath effects, tropospheric conditions and modeling, water vapor modeling and estimation, and time-varying phenomena associated with the global reference frame (i.e., ITRF). This research also focuses on evaluating a variety of factors that may have an impact on refining the height component of GPS positions, and investigating whether GPS-determined heights are substantially affected by meteorological events in the Antarctic region.

The outcome of these investigations will improve positional accuracy for the TAMDEF strain network. This includes analysis of the optimal mix of campaign and quasi-continuous GPS stations, the optimal duration and timing of campaign measurements, and other strategies to improve GPS results in TAMDEF. TAMDEF had the potential to be a source of meteorological information (used by the U.S. Antarctic Program Air Operations), which is useful for atmospheric modeling and weather prediction (e.g., Bevis *et al.* 1992), to improve geodetic reference control for Antarctic mapping purposes, and to be used as Differential GPS (DGPS) base stations for field parties working in surrounding areas. Furthermore, some of the TAMDEF sites are now part of the related POLar Earth observing NETwork (POLENET) which is expected to be an ambitious international project to understand geophysical aspects at very remote high-latitude such as the Antarctic continent (http://www.polenet.org/).

The Scientific Committee on Antarctic Research (SCAR) has been working on linking Antarctica to the ITRF (Dietrich *et al.* 2001). However, Boucher *et al*. (1998, 1999, and 2001) indicate that the current status of the ITRF is described in such a way that the distribution of control stations is still far from uniform in the Antarctic area. Considering the difficulties of access to most of the Antarctic continent, densification of the ITRF network throughout Antarctica is a demanding task (Boucher *et al.* 2001). The progress made in recent years indicates that the number of continuous GPS Antarctic stations has been increasing, and some of them are part of the IGS network (Beutler *et al.* 1996). In addition, POLENET will also contribute with deployment at very remote sites spanning much of the Antarctic continent using new and established technologies for Global Navigation Satellite System (GNSS) stations (Willis, 2008a).

Horizontal rates of motion had been validated for Antarctica by James and Ivins (1998) within 0-2 mm/yr. Dietrich *et al.* (2004) indicate that relative motion between the Antarctic Peninsula and East Antarctica is no larger than 1–2 mm/year. Consequently, Rülke *et al.* (2008) have found vertical deformation values (-4mm to +18mm) for the Antarctic continent. Furthermore, the horizontal GPS motions record Antarctic plate motion of ~15 mm/yr to the southeast (Willis, 2008b).

1.3 Chapter descriptions

The investigations and outcomes of this research are organized as follows:

Chapter 2 illustrates several aspects of GPS geodesy in Antarctica, specifically for the TAMDEF network. Besides TAMDEF location, monumentation and instrumentation, a description and analysis of GPS data availability and data processing, including a detailed procedure for calibrating the GPS antennas used in the TAMDEF network, is

presented. Possible influences of pseudorange multipath and ocean tide loading on the vertical coordinate components for the TAMDEF network are also analyzed.

Chapter 3 discusses the least-squares algorithm with stochastic constraints for network adjustment, used in PAGES (Program for Adjustment of GPS Ephemerides), and it describes in detail the alternative adjustment algorithms proposed for the TAMDEF network. Outlier detection and hypothesis testing are also addressed in this chapter, as well as the link of the TAMDEF network to ITRF00 by using the Helmert blocking least-squares adjustment and the GPSCOM processing tool subroutine built with PAGES software.

Chapter 4 presents a complete description of the tropospheric modeling methodology for the TAMDEF sites. A detailed procedure is described to estimate the total wet zenith delay (TWZD); this is later transformed to atmospheric precipitable water vapor (PWV) content by employing three selected mapping functions with two different tropospheric models. Estimates of PWV are compared and analyzed with numerical weather prediction models and physical radiosonde measurements.

Chapter 5 presents the assessment and analysis of results for the various topics investigated in this research, such as the antenna testing, site multipath detection and analysis, PWV estimates, ocean tide loading and least-squares adjustment for the TAMDEF network.

Chapter 6 summarizes the results and the conclusions of this study. It also includes discussions and the future outlook.

CHAPTER 2

TAMDEF GPS NETWORK, VICTORIA LAND, ANTARCTICA

2.1 Introduction

The Antarctic continent contains the West Antarctic rift system and the TransAntarctic Mountains, one of the highest and longest uplifted rift flanks in the world. The TAMDEF (TransAntarctic Mountains Deformation) network in the region throughout southern Victoria Land was established in 1996 to detect bedrock motions caused by possible changes in the mass of the Antarctic Ice Sheets (http://www.geology.ohio-state.edu/TAMDEF/). TAMDEF network succeeded in measuring crustal motion based on a campaign-style surveying by using precise GPS measurements separated over a 10-year period (1996-2006). A complete description of the TAMDEF network is presented in the following sections, together with a thorough analysis of the network measurement data.

2.2 TAMDEF GPS network

The TAMDEF network used to be an average baseline GPS array (see Figure 2.1) deployed on bedrock sites throughout southern Victoria Land, established by The Ohio State University (OSU) and the US Geological Survey (USGS), and sponsored by the National Science Foundation (NSF) (http://www.geology.ohio-state.edu/TAMDEF/). The original idea of the TAMDEF network was to provide baselines for repeated surveys over the entire period, to measure any detectable crustal motions.

During the first field season (1996-1997), 23 campaign sites were set up; four more sites were installed during the second season (1997-1998). These two seasons were characterized by using the classical short-duration campaign style occupations of multiple stations deployed to span key baselines simultaneously. The 28th site was installed during the third field season (1998-1999). Almost all 28 sites were reoccupied during the fourth field season (1999-2000) in collaboration with the USGS and the Italian Antarctic Program (PNRA). During the following two field seasons (2000-2001 and 2001-2002) quasi-continuous running remote stations were installed. Hence, a substantial improvement was achieved in the duration of measurements logged at each site, increasing from 2-3 days up to four weeks at a 30-second sampling rate. This was also possible due to the memory upgrades and improved power efficiency of the GPS receivers. Prior to the seventh field season (2002-2003), some of the TAMDEF stations began recording quasi-continuous data throughout the year (i.e., Fishtail Point, FTP1; Cape Roberts, ROB1; and Mount Fleming 2, FLM2), allowing large multi-day data sets to be collected. The long campaign data sets improved the precision and accuracy of the results, and so the goal of employing a measurement strategy that combined a longer duration of measurements at a large number of sites (some of which record nearly continuously throughout the year). Finally, OSU installed three more CORS

(Continuously Operating Reference Stations) sites (namely, Franklin Island East, FIE0; Lonewolf Nunatak, LWN0; and Westhaven Nunatak, WHN0), in the seventh (2002-2003) and eighth (2003-2004) field seasons, to further improve and expand the TAMDEF network.

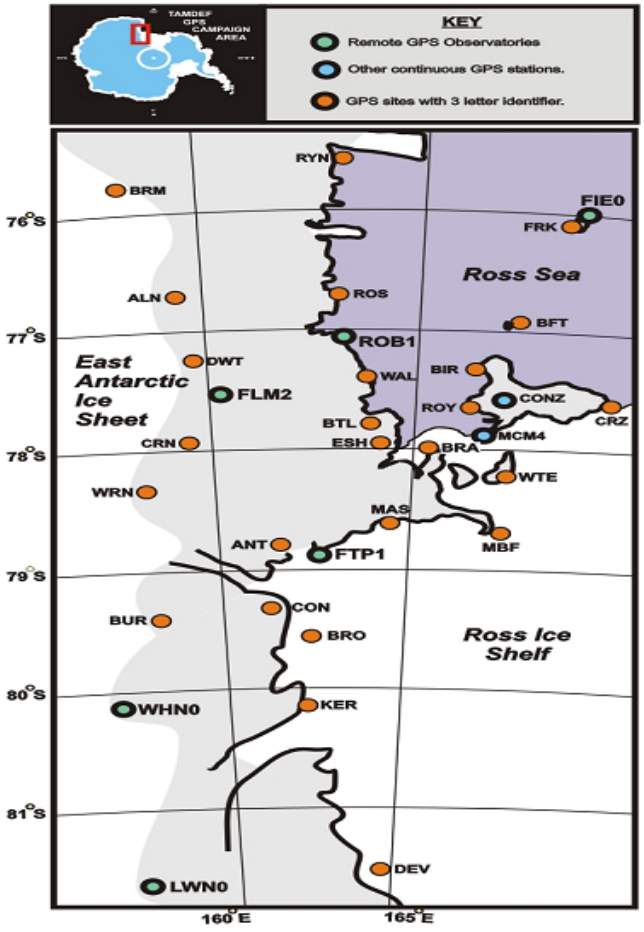

Figure 2.1: TAMDEF network, Victoria Land, Antarctica, 2004.

Ten field seasons were completed since 1996, resulting in a TAMDEF GPS network consisting of 25 primary campaign sites (usually located on bedrock), six quasi-continuous sites and two continuous sites deployed to span different crustal blocks defined by faults or crustal lineaments (see Figure 2.2).

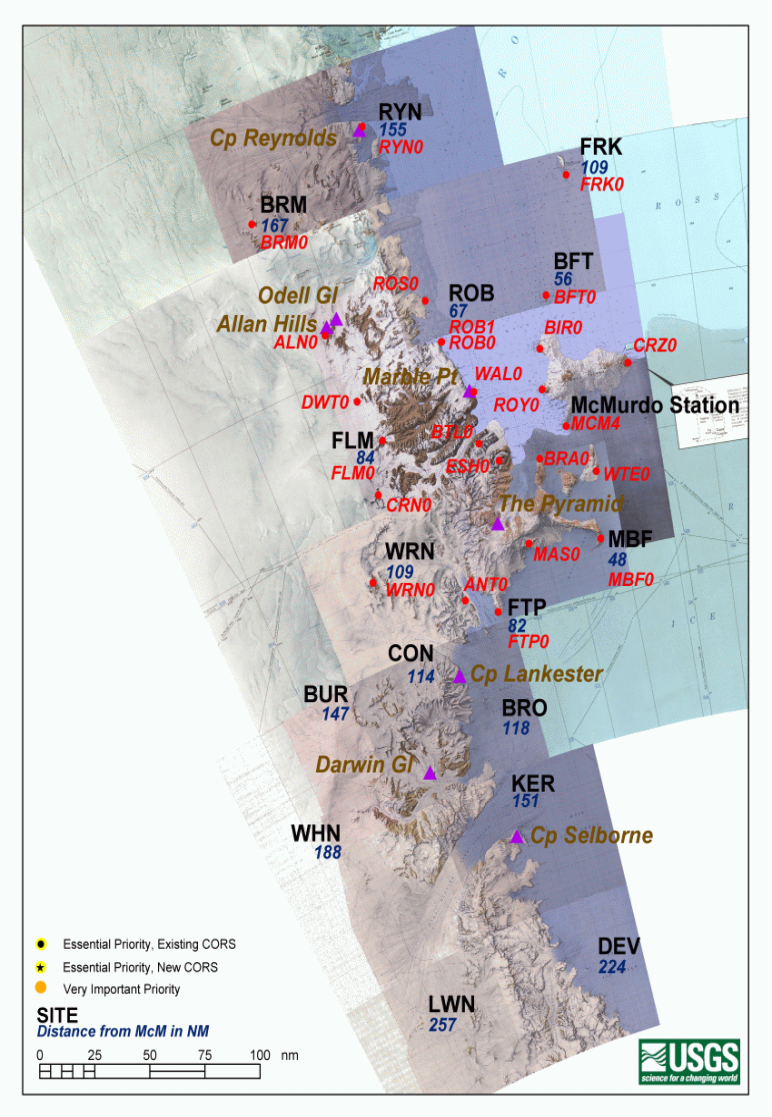

Figure 2.2: TAMDEF network, Victoria Land, Antarctica, 2006.

2.2.1 TAMDEF sites location

The decision on where to locate the TAMDEF sites was based on geological information (e.g., sites were established on bedrock) and by inspection of satellite imagery and aerial photographs. The collaborative geodetic field teams staffed by the USGS and OSU surveyed potential GPS sites. The actual sites were later selected and GPS receivers and antennas deployed, based on the analysis of all the previous information. The OSU GSD (Geological Science Department) participated in the site selection by documenting the geological structure of the sites and ensuring suitable bedrock structural integrity.

2.2.2 TAMDEF sites monumentation

The ground monumentation for the TAMDEF network consists of very stable geodetic steel pins (8 inch long, stainless steel, 5/8-inch diameter) sunk directly into bedrock (see Figure 2.3), with metal force-centered fixed-height (0.0794m) level mounts to guarantee accurate re-centering of the GPS antenna at each site each year (Zhang *et al.* 1997). The bottom of the divot (which is on the top of the rock pin) is then considered as the reference point for the measurement results.

Figure 2.3: Rock pin and the force-centered fixed-height level-mount.

2.2.3 TAMDEF GPS instrumentation

TAMDEF hardware consists of a wide variety of dual-frequency, 12-20 channel, geodetic-grade GPS receivers, kept in insulated boxes and powered from 60W solar panels and 80 amp-hours gel-cell batteries. The GPS receivers used in the TAMDEF network are: Trimble 5700/R7, Ashtech Z-Surveyors, DL4-NovAtel, Leica RS500, Javad Legacy and Javad Euro-80. The GPS receivers, supplied through cooperation with USGS, OSU and UNAVCO (University NAVstar COnsortium), are usually set to record data every 30 seconds in the field without any replacement of their memory cards. To allow for consistency, the TAMDEF team places the same antenna type at each site each year. TAMDEF almost exclusively uses Ashtech/Thales Dorne-Margolin (D&M) choke-ring antenna designed to reduce L1 multipath. This type of antenna is used because it accepts a wide range of input voltages. It has also been tested to be consistent for possible phase center variations when using the antenna calibration parameters provided by the National Geodetic Survey (NGS) http://www.grdl.noaa.gov/ANTCAL/. Refer to Section

2.5 for the NGS antenna calibration procedure. In addition, an effort was made by the TAMDEF team to test other antenna types in the Antarctic environment; for descriptions of the test refer to Section 2.6.

2.3. GPS data availability

As mentioned in Section 2.2, when the TAMDEF network was first established, only campaign data could be collected and analyzed. However, this has improved over the past few years and data from some quasi-continuous and continuous trackers are now available for further processing. The Figure 2.4 illustrates TAMDEF station data availability with up to 355-day duration of collected data from 1996 to 2005. The rest of the sites and their availability are shown in Appendix A (Figures A.1, A.2 and A.3).

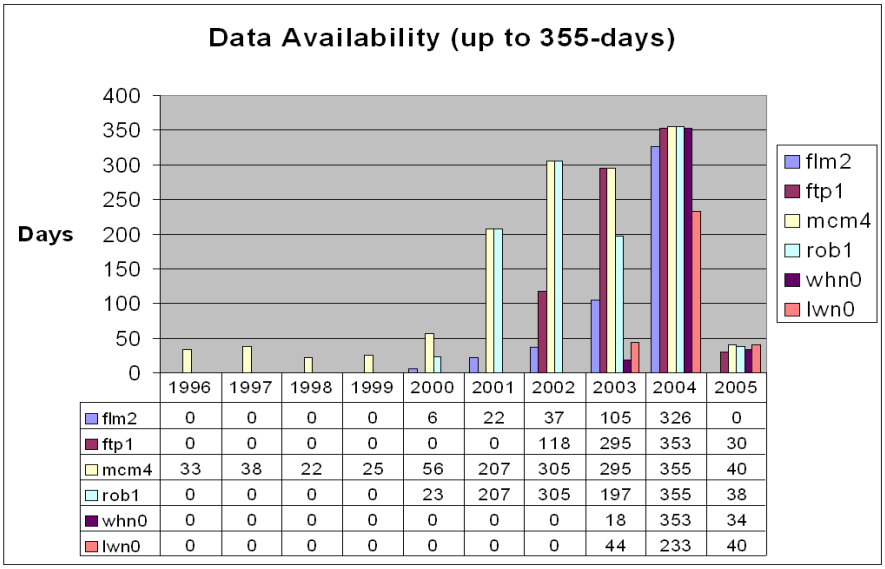

	1996	1997	1998	1999	2000	2001	2002	2003	2004	2005
flm2	0	0	0	0	6	22	37	105	326	0
ftp1	0	0	0	0	0	0	118	295	353	30
mcm4	33	38	22	25	56	207	305	295	355	40
rob1	0	0	0	0	23	207	305	197	355	38
whn0	0	0	0	0	0	0	0	18	353	34
lwn0	0	0	0	0	0	0	0	44	233	40

Figure 2.4: GPS data availability for the TAMDEF network.

2.4 GPS data analysis and data quality assessment

GPS data processing, data analysis and data quality assessment are essential tasks in any GPS survey when precise geodetic results are desired. The TAMDEF GPS data were converted and archived to the RINEX (Receiver INdependent EXchange) format (ftp://igscb.jpl.nasa.gov/igscb/data/format/rinex210.txt). The TEQC software (Test of Quality Check), provided by UNAVCO and available for public use at (http://www.unavco.org/facility/software/teqc/teqc.html), was used to verify the quality and integrity of the RINEX files (i.e., cycle slips, receiver multipath, and receiver clock drift). After that verification, the GPS data were processed with the PAGES software, (Mader *et al.* 1995; Eckl *et al.* 2001; Schenewerk *et al.* 2001; http://www.ngs.noaa.gov/GRD/GPS/DOC/pages/pages.html) considered the newest generation of orbit/baseline estimation software. This GPS processing package was

developed at the NGS and it has been shown by Schenewerk (2004) that this powerful GPS software is suitable for a variety of projects requiring the highest accuracy. The main specifications for the GPS data processing included the use of a 30-sec sampling rate, 10° cut-off angle and ambiguity fixing (with an ambiguity resolution success rate of ~90-95%) in most cases. In order to produce an optimal solution, the ionosphere-free double-differenced (DD) carrier phase method (see Section 2.4.1) was employed, using the precise final orbits disseminated by IGS. Similarly, to average out the effects of short duration fluctuations in the ionosphere, local multipath, and ocean loading, 24-hour data sets were used.

2.4.1 Ionosphere-free double-differenced carrier phase method

PAGES uses ionosphere-free and wide-lane linear combinations to convert the L1 and L2 carrier phase ambiguities to their integer values. The reasons for using both iono-free and wide-lane linear combinations rather than the L1 and L2 phase observations are: (1) the L1 and L2 phase observations include ionospheric bias, which can cause variations larger than one cycle; (2) the iono-free combination is free of ionospheric bias; and (3) the wide-lane observation has such a long wavelength (~86 cm) that only very rarely does ionospheric variation exceed one wide-lane wavelength, making it very effective in the ambiguity-resolution process (Schenewerk, 2004). Hence, these two observations are largely resistant to the effects of the ionosphere, and simultaneously facilitate the evaluation of integer phase ambiguities. Equations (2.1) and (2.2) give the mathematical expressions for iono-free and wide-lane observations (in cycles), respectively:

$$Ionofree = \frac{c}{(f_1^2 - f_2^2)}(f_1\Phi_1 - f_2\Phi_2) \tag{2.1}$$

$$Widelane = \frac{c}{(f_1 - f_2)}(\Phi_1 - \Phi_2) \tag{2.2}$$

where:

Φ_1 and Φ_2 are the observed L_1 and L_2 phase measurements (in cycles),

f_1 and f_2 are the carrier frequencies,

c is the speed of light.

Equations (2.1) and (2.2) can be used to define the L1 and L2 observations in terms of the iono-free and wide-lane observations (in cycles) as:

$$\Phi_1 = (Ionofree)\frac{(f_1 + f_2)}{c} - (Widelane)\frac{f_2}{c} \tag{2.3}$$

$$\Phi_2 = \Phi_1 - (Widelane)\frac{(f_1 - f_2)}{c} = (Ionofree)\frac{(f_1 + f_2)}{c} - (Widelane)\frac{f_1}{c} \tag{2.4}$$

The disadvantage of using this linear combination is that wide-lane and the iono-free combinations become mathematically correlated (Schaffrin and Bock, 1988). The computed carrier phase values on L1 and L2 will still not be integers, but they will be very close to integers. Thus, to obtain integer ambiguities, PAGES is configured to use

the iono-free DD carrier phase combination (Equation (2.1)) whose model, after conversion to length unit, is given by Equation (2.5):

$$\Phi_{ij,12}^{kl} = \rho_{ij}^{kl} + T_{ij}^{kl} + \alpha_1\lambda_1 N_1 + \alpha_2\lambda_2 N_2 + \alpha_1\varepsilon_{ij,1}^{kl} + \alpha_2\varepsilon_{ij,2}^{kl} \quad (2.5)$$

with

$$\alpha_1 = \frac{f_1^2}{f_1^2 - f_2^2} \text{ and } \alpha_2 = -\frac{f_2^2}{f_1^2 - f_2^2}$$

where:

i and j are subscripts that denote receivers,

k and l are superscripts that denote satellites,

ρ_{ij}^{kl} is the DD-geometric distance between the respective satellites and receivers,

$1, 2$ indicate that the carriers L_1 and L_2 are involved in the combination,

T_{ij}^{kl} is the DD tropospheric refraction term,

$\lambda_1 \approx 19$ cm and $\lambda_2 \approx 24$ cm are the wavelengths of the signals on the L_1 and L_2 carriers, respectively,

N_1 and N_2 are the integer ambiguities associated with the phase measurements (in cycles) on L_1 and L_2, respectively,

$\varepsilon_{ij,1}^{kl}$ and $\varepsilon_{ij,2}^{kl}$ are the random DD measurement noise terms (in meters) for the observed phases on L_1 and L_2, respectively.

2.5 NGS antenna calibration procedure

The L1 or L2 antenna phase centers are the theoretical points in space where the carrier phase of the GPS signals are received. The actual location where the signal is received, however, varies as a function of the direction of the incoming GPS signal, the electrical characteristics of the GPS antenna, and the antenna environment. The antenna Phase Center Variations (PCVs), if not properly accounted for, are aliased into the tropospheric correction, which, in turn, corrupts the station height estimate. Hence, the PCVs must be compensated for in the GPS data processing. These relative PCVs are measurable and available in the form of the standard relative antenna calibration models provided by NGS. If the highest quality positioning results are expected, it is necessary to account for the PCVs. A failure to do so could lead to errors of up to 10 cm in height when processing GPS data for a baseline involving two different antenna types (Mader, 1999). The NGS calibrated many GPS antennas to determine how the location of the L1 and L2 phase centers vary with respect to the Antenna Reference Point (ARP, a specified physical point on the antenna). NGS makes both relative and absolute PCVs available for public use via the http://www.grdl.noaa.gov/ANTCAL/ website, and the description of the antenna calibration procedure can be found in Mader (1999).

The NGS calibration takes place at NGS's Instrumentation and Methodologies Branch located in Corbin, VA. At this test facility, two stable, 15 cm diameter, 1.8 m tall concrete piers located in a flat grassy field, separated by 5 m, aligned along the north-south direction, with permanently attached antenna-mounting plates on top, are used for

antenna calibration (see Figure 2.5). The GPS antennas are connected to the Ashtech Z12 GPS receivers; usually set to track to an elevation cut-off of 10° (Mader, 1999). The atmospheric conditions for both piers at the test facility are similar under the local environment. On the other hand, the Antarctic atmospheric conditions for the TAMDEF antennas are significantly different from those at NGS calibration facility. The TAMDEF antennas are mounted very close to the Earth's surface (see Table 2.2), and it can be expected that this may affect the electromagnetic characteristics of the antennas, which may in turn generate unexpected variations in the site height estimate. It has been shown by NGS that this effect appears to be negligible when the antenna is more than a meter above the ground (Mader, 1999). So, in general, this is not a serious consideration in most traditional surveys, but it may be an issue in the Antarctic environment and, in particular, for the TAMDEF network.

Figure 2.5: Antenna testing facility in Corbin, VA.

2.6 Testing antenna calibration parameters in the Antarctic environment: Experiment description

The antenna test was conducted at the Arrival Heights (ARR) site on Ross Island, above the McMurdo Station (also the location of the IGS station, MCM4), where two new markers, AHT1 and AHT2, separated by 28.1 m, were established (see Figures 2.6 - 2.8). The location, monumentation and the weather conditions of AHT1 and AHT2 are very similar to those within the TAMDEF network. The primary objectives of the antenna test were as follows.

1) With the reference ASH700936D_M Rev E antenna placed at AHT1, verify a possible change in the vertical coordinate of AHT2 after changing its antenna from

ASH701945D_M Rev D, to TRM29659.00, then to TRM41249.00, and to the NOV702_3.00 Rev 3 antenna.

2) Based on the results of (1), verify the applicability of the tested antenna types to any future TAMDEF (or other Antarctic) campaigns.

3) Test the accuracy of the standard relative antenna calibration models in the Antarctic environment.

Figure 2.6: AHT1 *reference site*, (see AHT2 in the background).

Figure 2.7: AHT2 *test site*, (see AHT1 in the background).

The length of the antenna cable used at AHT1 was 3.4 m at AHT2, the following antenna cables were used with the antennas tested: AHT2/1 = 11 m, AHT2/2 = 11 m, AHT2/3 = 10 m, AHT2/4 = 3 m (see Table 2.1 for details of antenna designation); no adapters, external attenuators or amplifiers were used. The site monumentation, typically used within TAMDEF, is illustrated in Figure 2.3; it is a UNAVCO fixed-height, force-centered level-mount, which has a constant antenna offset. It consists of a 8 inch long, stainless steel, 5/8-inch diameter threaded bolt, normally placed in the bedrock, with a metal forced-centered fixed-height level-mount placed on the pin. The bottom of the divot on the top of the rock pin is the reference point for the measurement results. This antenna/mount/pin set-up has proved to be extremely stable (Zhang *et al.* 1997).

Figure 2.8: MCM4 IGS site.

The coordinates of the *reference site* (AHT1) were determined *a priori* with respect to the MCM4 (AOA SNR-12 ACT) benchmark receiver with a AOAD/M_T antenna (see Figure 2.8), using 72 hours of continuously collected GPS data, while the coordinates of the *test site* (AHT2) were determined with respect to AHT1, based on 72 hours of data. The separation between AHT1 and MCM4 was 194.2 m**.** A summary of the hardware used is presented in the Table 2.1, including the date and the time span for each site occupation. The antenna height for the four sessions was the same 0.0794 m.

Table 2.2 shows the antenna height from ARP and the distance from the phase center to ARP (see also Figure 2.9). Table 2.3 gives the technical parameters, such as antenna gain (on L1 and L2 carriers) and input voltage specifications of each antenna type used in the experiment.

Site/ Session	Receiver Type	Antenna Type and Model	IGS Designator	Start date and time [UTC]	End date and time [UTC]	Comments
AHT1/1-4	JPS Legacy	Ashtech choke ring D&M	ASH700936D_M Rev E	Nov. 17, 19:43:10	Dec.1, 19:43:40	Four 3-day sessions
AHT2/1	JPS Legacy	Ashtech choke ring D&M	ASH701945D_M Rev D	Nov. 17, 19:46:55	Nov. 20, 19:39:00	3-day session
AHT2/2	JPS Legacy	Trimble choke ring	TRM29659.00	Nov. 20, 19:43:45	Nov. 23, 19:43:40	3-day session
AHT2/3	JPS Legacy	Trimble zephyr geodetic	TRM41249.00	Nov. 24, 19:43:45	Nov. 26, 19:43:40	2-day session
				Nov. 27, 19:43:45	Nov. 28, 19:43:40	1-day session
AHT2/4	JPS Legacy	NovAtel GPS-702 Rev3	NOV702_3.00 Rev 3	Nov. 28, 19:49:35	Dec. 1 19:49:30	3-day session

Table 2.1: Hardware used and test description.

Site/ Session	Antenna type	Height from the reference mark to ARP [m]	Distance from the phase center to ARP [m]
AHT1/1-4	Ashtech choke ring D&M	0.0794	0.095 (L1) and 0.121 (L2)
AHT2/1	Ashtech choke ring D&M	0.0794	0.095 (L1) and 0.121 (L2)
AHT2/2	Trimble choke ring	0.0794	0.11 (to nominal phase center)
AHT2/3	Trimble zephyr geodetic	0.0794	0.053 (to nominal phase center)
AHT2/4	NovAtel GPS-702 Rev3	0.0794	0.083 (L1) and 0.077 (L2)

Table 2.2: Antenna height specifications.

Site/Session	Antenna type	LNA gain (typical) [dB]	Input voltage [VDC]
AHT1/1-4	Ashtech choke ring D&M	38±3 (L1) and 39±3 (L2)	5 – 15
AHT2/1	Ashtech choke ring D&M	38±3 (L1) and 39±3 (L2)	5 – 15
AHT2/2	Trimble choke ring	50 (L1) and 48 (L2)	7 – 28
AHT2/3	Trimble zephyr geodetic	50 (on L1 and L2)	4.8 – 22
AHT2/4	NovAtel GPS-702 Rev3	27	4.5 – 18

Table 2.3: Antenna gain and voltage specifications.

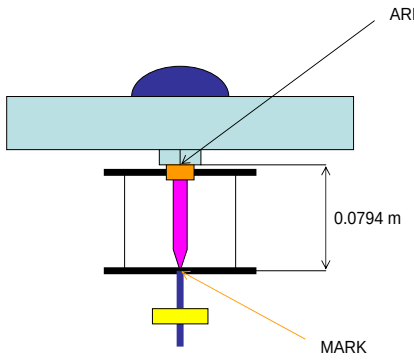

Figure 2.9: Location of the antenna reference point (ARP) and the actual mark (choke ring antenna shown as an example).

2.6.1 Field procedure and data processing

Dual-frequency geodetic-grade JPS Legacy receivers were used for the GPS data collection in static mode at the sites AHT1 and AHT2. Both receivers were programmed to collect 24-hour sessions (partial files were collected when the initial epoch was different from the GPS midnight, i.e., local 1:00 pm), with an elevation cut-off angle of 15 deg and data sampling rate of 5 s. The AHT1 *reference site* collected data in four consecutive 72-hour sessions, with no change in the hardware during the test. The AHT2 *test site* collected the data in four consecutive 72-hour sessions, each session with different antenna, as listed in the Table 2.1. The antennas at AHT2 were swapped at approximately the same time of day after the end of a three-day test period; however, because of severe weather conditions, the third session was split to a 2-day session (Nov. 24-26) and a 1-day session (Nov. 27-28). For this test, as well as for all TAMDEF network observations, all antennas tested were oriented to true north in order to be consistent with the NGS antenna calibration (i.e., antenna cable attachment point should be oriented to true north).

The quality and integrity of data stored in the RINEX files were also checked with TEQC software, and the data processing was performed using the PAGES software. However, since the test baseline was very short (28.1 m), the L1-fixed solution was here used (with the ambiguity resolution success rate of ~99%), with the elevation cut-off angle of 15º, data sampling interval of 5 sec, and precise IGS ephemeris. Under the assumption that for a baseline of 28.1 m atmospheric effects at both ends of the baseline were identical, the tropospheric parameters were not estimated. The NGS standard relative antenna calibration parameters for each type of antenna tested were used in the data reduction process. The results of this test are presented in Section 5.2.

2.7 Multipath detection and analysis

Despite their careful selection, the TAMDEF GPS sites are, to some extent, affected by the presence of local multipath (see Figure 2.10). This effect may vary slowly on a seasonal basis, or abruptly due to such natural events as snowfall. Studies of multipath effects and suitable processing techniques are given, for example, by Han and Rizos (1997), Rizos (1999), Meertens (2000), Ge *et al.* (2000), Dodson *et al.* (2001), Roberts *et al.* (2002), Ge *et al.* (2002) and Satirapod *et al.* (2003). It is important to indicate here that all of the methods cited above have their advantages and limitations; however, it is been shown in the above-cited literature that the multipath error in the pseudoranges is significantly larger (up to several meters) than for carrier phases (usually, millimeter to centimeter level).

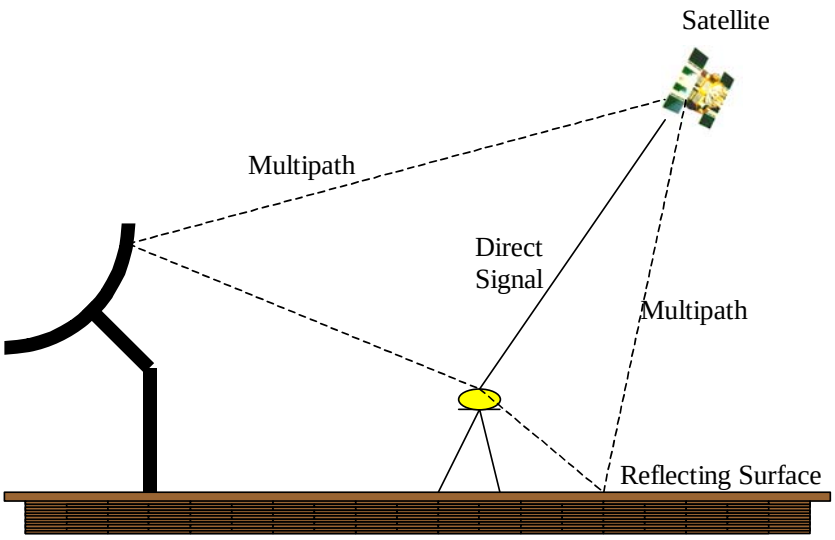

Figure 2.10: Multipath effect on GPS signals.

Since the multipath effect depends on the satellite geometry and the surrounding environment of the GPS antenna (as well as the antenna type), the effect is practically the same after one sidereal day under similar atmospheric conditions. In other words, with the current GPS orbit design, the entire satellite configuration normally advances about 4 minutes between two consecutive days. Thus, the positioning solution of data derived from the repetition of the GPS satellite constellation between two sidereal days ought to be affected by "systematic" multipath. This effect can be used to extract the multipath signature from the positioning time-series (Ge *et al.* 2000, Roberts *et al.* 2002). Hilla and Cline (2002) pointed out that the significance of analyzing pseudorange multipath is that the accuracy of any GPS application relies to a large extent on pseudorange measurements (e.g., differential pseudorange, kinematic and rapid static surveying, and ionospheric monitoring). Therefore, in order to identify the effective level of multipath, the daily root mean squared (MP1-RMS and MP2-RMS) variations were estimated and analyzed at each TAMDEF site. A detailed description of the procedure (Estey and Meertens (1999); Hilla and Cline (2002); http://www.unavco.org QC V3 Users Guide, UNAVCO 1994), used to estimate the pseudorange multipath, is given in the following section.

2.7.1 Pseudorange multipath estimation

It is important to point out, that in the one-way observation equations used for the multipath estimation, the inter-channel bias and the non-integer initial phase terms for the satellite and the receiver were neglected.

The pseudorange measurements on L_1 and L_2 are described as:

$$P_{L1} = R + c(\Delta t^S - \Delta t_R) + I_{L1} + T + MP_{P1} \tag{2.6}$$

$$P_{L2} = R + c(\Delta t^S - \Delta t_R) + I_{L2} + T + MP_{P2} \tag{2.7}$$

and the carrier phase measurements as:

$$\Phi_{L1} = R + c(\Delta t^S - \Delta t_R) + \lambda_{L1} N_{L1} - I_{L1} + T + MP_{\Phi_{L1}} \tag{2.8}$$

$$\Phi_{L2} = R + c(\Delta t^S - \Delta t_R) + \lambda_{L2} N_{L2} - I_{L2} + T + MP_{\Phi_{L2}} \tag{2.9}$$

where:

P_{L1} and P_{L2} are the pseudorange observations (in meters),

R is the geometric distance between the satellite and the receiver (in meters),

c is the constant speed of light (in meters/sec),

Δt^S is the satellite clock correction (in sec),

Δt_R is the receiver clock correction (in sec),

I_{L1} and I_{L2} are the ionospheric range errors (in meters),

T is the tropospheric range error (in meters),

N_{L1} and N_{L2} are the integer ambiguities (in cycles),

MP_{P1}, MP_{P2}, $MP_{\Phi_{L1}}$ and $MP_{\Phi_{L2}}$ are the corresponding pseudorange and carrier phase multipath, respectively (including the observational noise),

$\lambda_{L1} \approx 19$ cm and $\lambda_{L2} \approx 24$ cm are the wavelengths of the signals on L_1 and L_2,

$f_1 \approx 1.5754\ GHz$ and $f_2 \approx 1.2276\ GHz$ are frequencies of signals L_1 and L_2, respectively.

Taking the advantage of the relationship between the ionospheric delay for L_1 and L_2 leads to:

$$I_{L2} = \alpha \cdot I_{L1} \tag{2.10}$$

with

$$\alpha = \left(\frac{f_1}{f_2} \right)^2 .$$

Subtracting Equation (2.9) from (2.8) gives:

$$\Phi_{L1} - \Phi_{L2} = \lambda_{L1} N_{L1} - I_{L1} + MP_{\Phi_{L1}} - \lambda_{L2} N_{L2} + I_{L2} - MP_{\Phi_{L2}} \tag{2.11}$$

and substituting (2.10) into (2.11), grouping and simplifying yields:

$$\frac{(\Phi_{L1} - \Phi_{L2})}{(\alpha - 1)} = I_{L1} + \frac{(\lambda_{L1} N_{L1} - \lambda_{L2} N_{L2})}{(\alpha - 1)} + \frac{(MP_{\Phi_{L1}} - MP_{\Phi_{L2}})}{(\alpha - 1)} \tag{2.12}$$

Combining (2.12) with (2.8) to eliminate I_{L1} term, results in:

$$\begin{aligned} \Phi_{L1} + \frac{(\Phi_{L1} - \Phi_{L2})}{(\alpha - 1)} &= R + c(\Delta t^S - \Delta t_R) + T + \lambda_{L1} N_{L1} + \frac{(\lambda_{L1} N_{L1} - \lambda_{L2} N_{L2})}{(\alpha - 1)} \\ &\quad + MP_{\Phi_{L1}} + \frac{(MP_{\Phi_{L1}} - MP_{\Phi_{L2}})}{(\alpha - 1)} \\ &= R + c(\Delta t^S - \Delta t_R) + T + b_1 + m_{\Phi_1} \end{aligned} \tag{2.13}$$

Equation (2.13) is a linear combination of observed L_1 and L_2 carrier phases, where the ambiguity bias term b_1 is introduced as:

$$b_1 = \lambda_{L1} N_{L1} + \frac{(\lambda_{L1} N_{L1} - \lambda_{L2} N_{L2})}{(\alpha - 1)} \tag{2.14}$$

while the phase multipath effect is now defined by:

$$m_{\Phi_1} = MP_{\Phi_{L1}} + \frac{(MP_{\Phi_{L1}} - MP_{\Phi_{L2}})}{(\alpha - 1)} \tag{2.15}$$

Combining (2.6), (2.12) and (2.13) gives:

$$P_{L1} - [1 + \frac{2}{(\alpha - 1)}]\Phi_{L1} + [\frac{2}{(\alpha - 1)}]\Phi_{L2} = MP_{P1} - \frac{(\lambda_{L1} N_{L1} - \lambda_{L2} N_{L2})}{(\alpha - 1)} - b_1 + MP_{\Phi_{L1}} - 2m_{\Phi_1} \tag{2.16}$$

The new ambiguity bias term is now defined by:

$$B_1 = -\frac{(\lambda_{L1} N_{L1} - \lambda_{L2} N_{L2})}{(\alpha - 1)} - b_1 = -[1 + \frac{2}{(\alpha - 1)}]\lambda_{L1} N_{L1} + [\frac{2}{(\alpha - 1)}]\lambda_{L2} N_{L2} \tag{2.17}$$

and the new phase multipath effect is introduced as:

$$\begin{aligned} M_{\Phi 1} &= -(MP_{\Phi_{L1}} - MP_{\Phi_{L2}}) - m_{\Phi_1} \\ &= -[1 + \frac{2}{(\alpha - 1)}]MP_{\Phi_{L1}} + [\frac{2}{(\alpha - 1)}]MP_{\Phi_{L2}} = MP_{\Phi_{L1}} - 2m_{\Phi_1} \end{aligned} \tag{2.18}$$

The pseudorange multipath MP_1 is then expressed as the linear combination from (2.16), namely:

$$MP_1 = P_{L1} - [1 + \frac{2}{(\alpha - 1)}]\Phi_{L1} + [\frac{2}{(\alpha - 1)}]\Phi_{L2} = MP_{P1} + B_1 + M_{\Phi_1} \tag{2.19}$$

Similar derivations are performed to express MP_2 as a linear combination:

$$MP_2 = P_{L2} - [\frac{2 \cdot \alpha}{(\alpha - 1)}]\Phi_{L1} + [\frac{2 \cdot \alpha}{(\alpha - 1)} - 1]\Phi_{L2} = MP_{P2} + B_2 + M_{\Phi 2} \tag{2.20}$$

with:

MP_{P2}, B_2, and $M_{\Phi 2}$ are defined similarly to MP_{P1}, B_1, and $M_{\Phi 1}$.

2.8 Ocean tide modeling

Tides are mainly generated by the gravitational attraction of the Sun and the Moon over the elastic Earth causing a periodic deformation. Ocean tides are responsible for a significant part of the variable deformation of the sea surface. For many years this effect has been observed and studied with the objective of understanding its behavior. Because of the distribution of mass within the Earth, the gravitational attraction of the Sun or Moon generates a variation of the Earth's geopotential, in which the tide-generating potential U at the Earth's surface caused by the attraction of the Sun or Moon can be given according to Wang (2004) by:

$$U(R_e, \phi, \lambda) = \frac{GM}{R} \sum_{l=2}^{\infty} \left(\frac{R_E}{R} \right)^l P_l(\cos\theta) \tag{2.21}$$

where:

GM is the gravitational constant times the mass of the attracting Sun or Moon,

R_E is the mean radius of the Earth,

R and θ are the geocentric distance and zenith distance from the point (R_e, ϕ, λ) of the attracting Sun or Moon, respectively,

$P_l(\cos\theta)$ is the Legendre polynomial of degree l.

The effect of ocean tides can be computed from available models, which will be introduced in the Sections 2.8.1.1 and 2.8.1.2. However, polar ocean tide models remain poorly understood, despite the success of global tide modeling in deep oceans (King *et al.* 2005).

2.8.1 Effect of different ocean tide models on the TAMDEF network

Originally, the PAGES software was designed to use Schwiderski's Hydrodynamic model (Schwiderski, 1980). This is a global model that is dependent upon the quality of the bathymetry observations used, which in some cases it has produced large errors. Due to its limitations, however, alternative ocean tide models (OTMs) recently have been developed and validated for specific areas, such as Antarctica (King *et al.* 2005). However, these models were, minimally tested against independent data.

OTM validation plays an important role in Antarctic GPS comparisons as it ensures that GPS measurements in and across the region can be reduced to measuring crustal motion. Since these measurements are to be of high precision and accuracy, the ocean tides and the resulting displacement of the solid Earth caused by ocean tide loading (OTL) must be modeled accurately. The contribution of this research to understanding the effects of OTL is to investigate the impact of the semidiurnal (M_2, S_2, N_2 and K_2) and diurnal (K_1, O_1, P_1 and Q_1) constituents (see Table 2.4) on TAMDEF positioning results. Consequently, the two regional OTMs listed in Table 2.5 were tested while using PAGES. The selection criteria for these two models were the extent of the model's coverage and its previous validation for Antarctica (King *et al.* 2005).

Model	Source	Limits	Type [1]	Resolution [2]
TPXO6.2	Egbert *et al.* (1994)	$86^\circ S - 90^\circ N$	H+T/P+ERS+T/G	$0.25^\circ \times 0.25^\circ$
CATS02.01	Padman *et al.* (2002)	$86^\circ S - 58^\circ S$	H	$0.25^\circ \times 0.083^\circ$

[1] H–Hydrodynamic model
T/P–TOPEX/Poseidon altimetry data assimilated
ERS–ERS altimetry data assimilated
T/G–Tide gauge data assimilated

[2] Latitude × Longitude

Table 2.4: Ocean tide models validated around Antarctica (King *et al.* 2005).

Table 2.5 shows the semidiurnal and diurnal tidal constituents as generated for the OTM-TPXO6.2 (TOPEX/Poseidon), using MCM4 as an example. Similar tidal constituents were generated for the TAMDEF sites (within the limits stated in Table 2.4) using the CATS02.01 regional OTM (which will be discussed in Section 2.8.1.2).

Significant magnitudes in Table 2.5 are mainly due to diurnal tides, strictly speaking for the principal lunar (O_1) 9.7 mm and for the luni-solar declination (K_1) 11.3 mm.

Site: MCM4	**Model: OTM-TPXO6.2 (TOPEX/Poseidon)**	
	Semidiurnal Tides	
	Amplitude (cm)	**Phase (Degrees)**
M_2 **(Principal lunar)**	0.00242	8.5
S_2 **(Principal solar)**	0.00017	-22.2
N_2 **(Major lunar ecliptic)**	0.00029	64.1
K_2 **(Luni-solar declinational)**	0.00007	-122.1
	Diurnal Tides	
O_1 **(Principal lunar)**	0.00973	-23.7
P_1 **(Principal solar)**	0.00356	-6.6
Q_1 **(Major lunar ecliptic)**	0.00197	-25.6
K_1 **(Luni-solar declinational)**	0.01139	-13.7

Table 2.5: Semidiurnal and diurnal tidal constituents (MCM4 site as an example).

Another reason for selecting the two OTMs (listed in Table 2.5) is that, according to King *et al*. (2005), the uniqueness of these OTMs was defined by the exact model domain (coastline) and bathymetry, the amount and type of data assimilated and the model grid cell interval. Furthermore, the improvement of tide models in deep oceans relies significantly on the availability (and assimilation) of TOPEX/Poseidon (T/P) altimetry data (Anderson *et al.* 1995; Shum *et al.* 1997). A brief description of the two OTMs used in this research follows.

2.8.1.1 OTM-TPXO6.2 (TOPEX/Poseidon)

OTM-TPXO6.2 is considered to be the new OTM that has assimilated additional data for the Antarctic region. In fact, this is the current version of Egbert's global tidal solution (Egbert *et al.* 1994; Egbert and Erofeeva, 2002) that uses the inverse scheme OTIS (Oregon State University Tidal Inversion Software) to assimilate observation data to the hydrodynamic equations by a represented approach. In addition, this model also incorporates improved bathymetry data for the circum-Antarctic seas; these data have been collected and used in the Circum-Antarctic Tidal Simulation (CATS02.01) and the Circum-Antarctic Data Assimilation (CADA00.10) models (L. Erofeeva, personal communication, 2003). Tides are provided to this model as complex amplitudes of earth-relative sea-surface elevation for the semidiurnal (M_2, S_2, N_2 and K_2), diurnal (K_1, O_1, P_1 and Q_1) and two long-period (M_f, M_m) harmonic constituents.

2.8.1.2 OTM-CATS02.01 (Circum-Antarctic Tidal Simulation)

OTM-CATS02.01 is a regional hydrodynamic model developed by Padman *et al.* (2002), which is relatively new and limited to the oceans in the southern hemisphere ($58^{\circ} S$). It is driven by observed TOPEX/Poseidon (TPXO.5.1) sea surface heights along the northern open boundary. It uses linear drag parameterization, which leads to a better agreement with the Antarctic tide height data than the earlier CATS01.02, which was based on quadratic drag parametrization.

In summary, the strategy for the ocean tide analysis over the TAMDEF network will rely on the ability to generate the semidiurnal (M_2, S_2, N_2 and K_2) and diurnal (K_1, O_1, P_1 and Q_1) constituents (described in Section 2.6) from the two regional OTMs.

It is gratefully acknowledged that the constituents for the OTM-TPXO.6 and OTM-CATS02.01 models (which are analyzed in this research) were provided by Dr. C.K. Shum from OSU and by Dr. M. King from the University of Newcastle in the UK. An alternative and valuable source of these constituents is the International Earth Rotation Service (IERS) (http://www.oso.chalmers.se/~loading/). Once these models have been generated, they are tested using PAGES to analyze their effect on TAMDEF positioning results. The challenge of estimating the corrections for these OTM parameters over the TAMDEF region would also be an important issue to take into account in further research.

CHAPTER 3

LEAST–SQUARES ADJUSTMENT FOR THE TAMDEF NETWORK

3.1 Introduction

This chapter focuses on the selection and application of the network adjustment approach to process the TAMDEF network measurements with respect to other IGS sites inside and outside the Antarctic continent. In preliminary computations, TAMDEF was processed with respect to all possible Antarctic IGS sites in order to verify and quantify how TAMDEF behaves with respect to the Antarctic tectonic plate itself. Next, a similar process was investigated with respect to other IGS sites, outside Antarctica, located on the South American, African and Australian tectonic plates. At least four IGS stations from each of these tectonic plates were incorporated to the adjustment process.

3.2 Network adjustment strategy

The network adjustment strategy followed in this research involved the careful selection and application of the appropriate approach to process the TAMDEF network, based on the data from the campaign, quasi-continuous and continuous trackers (see Chapter 2). In order to accomplish this, the PAGES software (see Section 2.4) was employed. PAGES was set up to automatically design the connections or baselines, which form a minimal spanning tree (i.e,. there is only one path between any two sites). Furthermore, the software allows for changes in the network from session to session.

Four cases (Cases I-IV) were investigated for the TAMDEF network processing with respect to the IGS sites inside and outside Antarctica, and they are as follows.

Case I: The GPS data from the TAMDEF stations, six IGS stations: Casey, CAS1; Davis, DAV1; Kerguelen Islands, KERG; Mawson, MAW1; Syowa, SYOG; Veleskarvet, VESL, and one non-IGS station (Palmer, PALM) in Antarctica, were processed as GPS network I (see Figure 3.1). From the GPS network I, the six IGS and one non-IGS stations were stochastically constrained to provide a solution for the TAMDEF sites. The results generated from this processing provide verification and quantification of the behavior of the TAMDEF network with respect to the Antarctic tectonic plate itself.

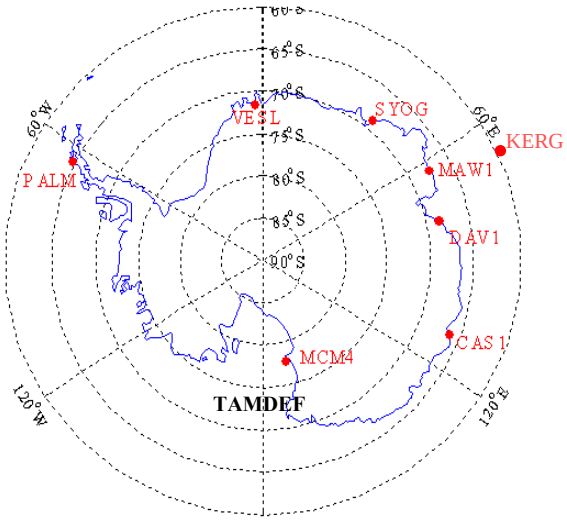

Figure 3.1: GPS Network I (Case I).

Case II: The GPS data from the TAMDEF stations, five IGS stations: Antuco, ANTC; Copiapó, COPO; Iquique, IQQE; Punta Arenas, PARC; Santiago, SANT, and one non-IGS station (Puerto Williams, PWMS) in South America were processed as GPS network II (see Figure 3.2).

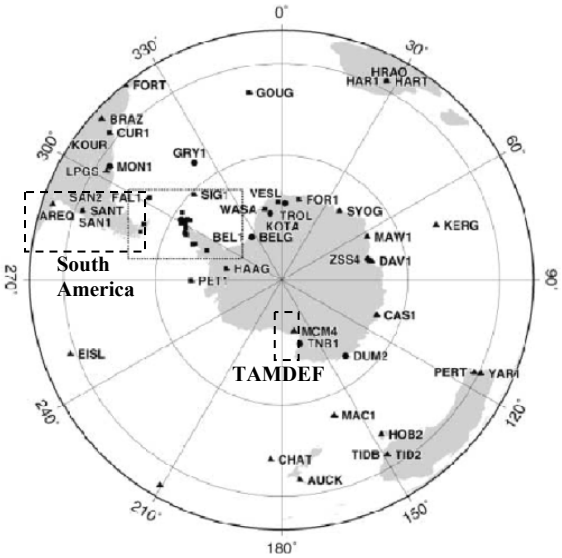

Figure 3.2: GPS Network II (Case II).

Case III: The GPS data from the TAMDEF stations and four IGS stations: Gough Island, GOUG; Hartebeesthoek, HARB; Hartebeesthoek Rao, HRAO; and Sutherland, SUTH in Africa were processed as GPS Network III (see Figure 3.3).

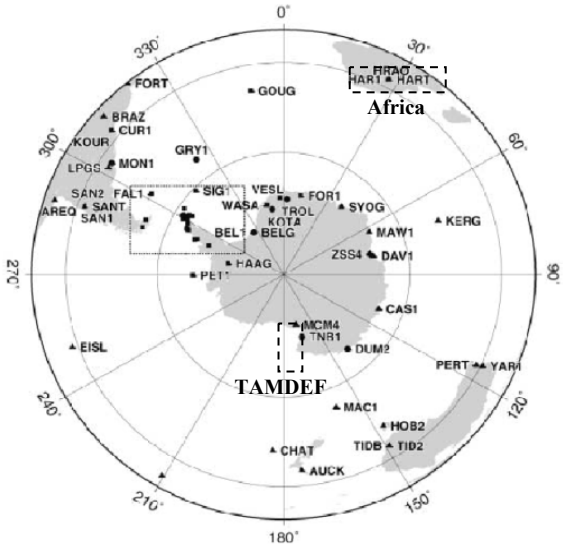

Figure 3.3: GPS Network III (Case III).

Case IV: The GPS data from the TAMDEF stations and four IGS stations: Alice Spring Avoir, ALIC; Ceduna AU019, CEDU; Karratha AU013, KARR; and Perth, PERT in Australia were processed as GPS Network IV (see Figure 3.4).

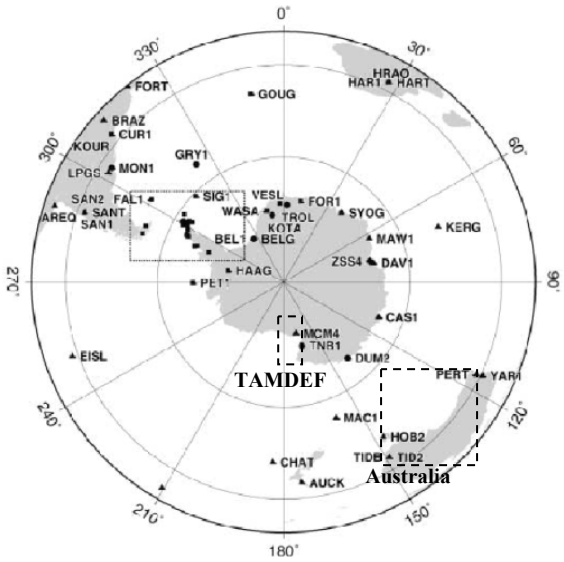

Figure 3.4: GPS Network IV (Case IV).

For GPS Networks II-IV, all the IGS and one non-IGS stations were stochastically constrained to provide solutions for the TAMDEF sites, including MCM4 (a common IGS and TAMDEF site). Again, the results generated from this processing are expected to provide verification and quantification of the TAMDEF network's behavior with respect to these tectonic plates. The decision to select the stations (IGS

and non-IGS) for the four cases above was made based on GPS data availability and consistency; the data with the extended periods of simultaneous GPS logging times with respect to the TAMDEF data were selected. The coordinates and velocities, with their corresponding standard deviations, for the IGS sites (ITRF00) were obtained from the IGS website http://itrf.ensg.ign.fr/ITRF_solutions/2000/ITRF2000.php and are listed in the Tables 3.1-3.4.

IGS Site	Coordinate/Velocity			St. Dev. Coord. / St. Dev. Vel.		
	$X\ [m]$	$Y\ [m]$	$Z\ [m]$	$\sigma_X\ [m]$	$\sigma_Y\ [m]$	$\sigma_Z\ [m]$
	$V_X\ [m/yr]$	$V_Y\ [m/yr]$	$V_Z\ [m/yr]$	$\sigma_{V_X}\ [m/yr]$	$\sigma_{V_Y}\ [m/yr]$	$\sigma_{V_Z}\ [m/yr]$
CAS1	-901776.1620	2409383.4190	-5816748.4200	0.001	0.002	0.003
	0.0001	-0.0077	-0.0073	0.0004	0.0005	0.0010
DAV1	486854.5480	2285099.3020	-5914955.6830	0.001	0.001	0.003
	0.0008	-0.0032	-0.0057	0.0004	0.0004	0.0006
KERG	1406337.3360	3918161.1000	-4816167.3550	0.001	0.002	0.002
	-0.0053	0.0028	-0.0058	0.0005	0.0007	0.0008
MAW1	1111287.1660	2168911.279	-5874493.595	0.002	0.003	0.008
	0.0014	-0.0023	-0.0036	0.0008	0.0012	0.0028
MCM4	-1311703.2500	310815.1040	-6213255.1250	0.001	0.001	0.003
	0.0088	-0.0120	-0.0033	0.0004	0.0004	0.0013
SYOG	1766207.8410	1460290.3500	-5932297.6800	0.003	0.002	0.007
	0.0038	-0.0015	-0.0015	0.0008	0.0008	0.0018
VESL	2009329.7130	-99741.4740	-6033158.4720	0.003	0.002	0.005
	0.0102	0.0018	0.0048	0.0009	0.0009	0.0011
PALM	1192671.7730	-2450887.5810	-5747096.0450	0.002	0.003	0.006
	0.0165	-0.0052	0.0029	0.0008	0.0012	0.0024

Table 3.1: ITRF00 coordinates for IGS Sites in Antarctica at epoch 1997.

IGS Site	Coordinate/Velocity			St. Dev. Coord. / St. Dev. Vel.		
	$X\ [m]$	$Y\ [m]$	$Z\ [m]$	$\sigma_X\ [m]$	$\sigma_Y\ [m]$	$\sigma_Z\ [m]$
	$V_X\ [m/yr]$	$V_Y\ [m/yr]$	$V_Z\ [m/yr]$	$\sigma_{V_X}\ [m/yr]$	$\sigma_{V_Y}\ [m/yr]$	$\sigma_{V_Z}\ [m/yr]$
ANTC	1608539.4770	-4816370.0100	-3847799.0100	0.001	0.003	0.005
	0.0144	-0.0002	0.0094	0.0004	0.0007	0.0010
COPO	1907041.0036	-5337379.0040	-2916335.0002	0.001	0.001	0.003
	0.0206	-0.0022	0.0145	0.0004	0.0002	0.0006
IQQE	2034208.3400	-5629172.2810	-2196142.0030	0.001	0.002	0.002
	0.0243	-0.0011	0.0139	0.0002	0.0007	0.0008
PARC	1255992.4075	-3622975.0829	-5079719.3282	0.002	0.003	0.008
	0.0056	-0.0081	0.0092	0.0008	0.0012	0.0018
SANT	1769693.3370	-5044574.1480	-3468321.0480	0.001	0.002	0.002
	0.0221	-0.0059	0.0111	0.0004	0.0005	0.0005
PWMS	1400423.3700	-3395146.9093	-5197233.1151	0.003	0.002	0.007
	0.0095	-0.0068	0.0078	0.0006	0.0007	0.0017

Table 3.2: ITRF00 coordinates for IGS Sites in South America at epoch 1997.

IGS Site	Coordinate/Velocity			St. Dev. Coord. / St. Dev. Vel.		
	$X\ [m]$	$Y\ [m]$	$Z\ [m]$	$\sigma_X\ [m]$	$\sigma_Y\ [m]$	$\sigma_Z\ [m]$
	$V_X\ [m/yr]$	$V_Y\ [m/yr]$	$V_Z\ [m/yr]$	$\sigma_{V_X}\ [m/yr]$	$\sigma_{V_Y}\ [m/yr]$	$\sigma_{V_Z}\ [m/yr]$
GOUG	4795578.5410	-835299.5370	-4107634.0650	0.009	0.004	0.008
	0.0140	0.0181	0.0152	0.0039	0.0018	0.0034
HARB	5084657.6317	2670324.9606	-2768481.2804	0.001	0.001	0.001
	-0.0019	0.0224	0.0181	0.0001	0.0001	0.0001
HRAO	5085352.4890	2668395.6700	-2768731.6760	0.003	0.002	0.002
	-0.0012	0.0198	0.0159	0.0005	0.0003	0.0004
SUTH	5041274.8080	1916053.9920	-3397076.0740	0.006	0.003	0.004
	0.0057	0.0197	0.0146	0.0022	0.0012	0.0015

Table 3.3: ITRF00 coordinates for IGS Sites in Africa at epoch 1997.

IGS Site	Coordinate/Velocity			St. Dev. Coord. / St. Dev. Vel.		
	$X\ [m]$	$Y\ [m]$	$Z\ [m]$	$\sigma_X\ [m]$	$\sigma_Y\ [m]$	$\sigma_Z\ [m]$
	$V_X\ [m/yr]$	$V_Y\ [m/yr]$	$V_Z\ [m/yr]$	$\sigma_{V_X}\ [m/yr]$	$\sigma_{V_Y}\ [m/yr]$	$\sigma_{V_Z}\ [m/yr]$
ALIC	-4052051.8300	4212836.1000	-2545105.8360	0.008	0.008	0.005
	-0.0437	0.0009	0.0497	0.0029	0.0030	0.0019
CEDU	-3753472.2310	3912740.9840	-3347960.8600	0.009	0.009	0.008
	-0.0455	0.0066	0.0461	0.0033	0.0034	0.0029
KARR	-2713832.2580	5303935.0870	-2269515.0120	0.006	0.0010	0.005
	-0.0458	0.0058	0.0512	0.0022	0.0037	0.0018
PERT	-2368686.9680	4881316.5170	-3341796.1610	0.001	0.002	0.002
	-0.0483	0.0101	0.0490	0.0004	0.0007	0.0006

Table 3.4: ITRF00 coordinates for IGS Sites in Australia at epoch 1997.

3.3 Least–squares adjustment

From all the estimates considered in this dissertation, several versions of the LESS (Least-Squares Solution) will be discussed in greater detail. At this point, only the important characteristics of each underlying model (e.g., rank of the normal equation matrix, constraints imposed or bias properties of the solutions) will be provided. The cited models will be presented in their linearized forms, in terms of incremental parameters and observations.

3.3.1 LEast–Squares Solution (LESS) in the Gauss Markov Model with full column rank

The LESS is usually the traditional approach for adjustment and is given within a Gauss-Markov Model as follows (Koch, 1999):
Linear model (Gauss-Markov with full column rank):

$$\underset{n\times 1}{y} = \underset{n\times m}{A}\ \underset{m\times 1}{\xi} + \underset{n\times 1}{e} \tag{3.1}$$

where

$\underset{n\times 1}{y}$ is the $(n\times 1)$ observation vector,

$\underset{n\times m}{A}$ is the $(n\times m)$ "Jacobian" or design matrix,

$\underset{m\times 1}{\xi}$ is the $(m\times 1)$ unknown parameter vector,

$\underset{n\times 1}{e}$ is the $(n\times 1)$ random error vector,

with

$rank(A) = q = m < n$,

and with the stochastic model for e described by:

$$e \sim (0, \sigma_0^2 P^{-1})$$

where:

σ_0^2 is the unknown variance component,

P is the corresponding weight matrix.

Normal equations:

$$N\hat{\xi} = c \tag{3.2}$$

with

$$[N,\ \ c] = A^T P\ \ [A,\ \ y]$$

Estimated parameters (LESS of ξ):

$$\hat{\xi} = N^{-1}c \tag{3.3}$$

Predicted errors or residuals:

$$\tilde{e} = y - A\hat{\xi} \tag{3.4}$$

Dispersion matrix of the estimated parameters:

$$D\{\hat{\xi}\} = \sigma_0^2 N^{-1} \tag{3.5}$$

Dispersion matrix of the predicted errors:

$$D\{\tilde{e}\} = \sigma_0^2 (P^{-1} - AN^{-1}A^T) \tag{3.6}$$

Estimated variance component:

$$\hat{\sigma}_0^2 = \frac{\tilde{e}^T P \tilde{e}}{n-m} \tag{3.7}$$

where:

$\hat{\sigma}_0^2$ is the estimated (reference) variance component,

n is the number of observations, and

m is the number of unknowns, equaling the rank of A.

Estimated dispersion matrices result from replacing σ_0^2 by $\hat{\sigma}_0^2$ in Equations (3.5) and (3.6).

3.3.2 Least–squares adjustment in the Gauss-Markov Model with stochastic constraints (SCLESS)

The main adjustment approach used in this research involves the use of prior information for the parameters, coordinates and velocities, with their corresponding variances for the IGS sites (all of which are tied to the ITRF00). Such an approach is described as the LESS in a Gauss-Markov Model with Stochastic Constraints (SCLESS). Here, the positive definite weight matrix P_0 is formed by the *a priori* variances (for IGS sites) obtained from a previous least-squares adjustment. Recall that the coordinates and velocities of these IGS sites are given with respect to ITRF00 at epoch 1997.0 (refer to Tables 3.1-3.4). For a detail derivation of the formulas, see Schaffrin and Snow (2007).

Linear model (Gauss-Markov with stochastic constraints):

$$\begin{aligned} y_{n\times 1} &= A_{n\times m}\xi_{m\times 1} + e_{n\times 1} \\ z_{0l\times 1} &= K_{l\times m}\xi_{m\times 1} + e_{0l\times 1} \end{aligned} \tag{3.8}$$

with

$$rank(A) = q \le \{m, n\};\ rank(K) = l \ge m - q;\ rank([A^T \quad K^T]) = m,$$

and with the stochastic model for e and e_0 described by:

$$\begin{bmatrix} e \\ e_0 \end{bmatrix} \sim \left(\begin{bmatrix} 0 \\ 0 \end{bmatrix},\ \sigma_0^2 \cdot \begin{bmatrix} P^{-1} & 0 \\ 0 & P_0^{-1} \end{bmatrix} \right)$$

Normal equations:

$$\begin{bmatrix} N & K^T \\ K & -P_0^{-1} \end{bmatrix} \cdot \begin{bmatrix} \hat{\xi} \\ \hat{\lambda} \end{bmatrix} = \begin{bmatrix} c \\ z_0 \end{bmatrix} \tag{3.9}$$

with $\hat{\lambda}$ as the $l \times l$ vector of estimated Lagrange multiplier.

Estimated parameters (if $q = m$) of type SCLESS:

$$\begin{bmatrix} \hat{\xi} \\ \hat{\lambda} \end{bmatrix} = \begin{bmatrix} N^{-1}c - N^{-1}K^T\hat{\lambda} \\ (P_0^{-1} + KN^{-1}K^T)^{-1}(KN^{-1}c - z_0) \end{bmatrix} = \begin{bmatrix} (N + K^T P_0 K)^{-1}(c + K^T P_0 z_0) \\ -P_0(z_0 - K\hat{\xi}) \end{bmatrix} \tag{3.10}$$

Predicted errors or residuals:

$$\begin{bmatrix} \tilde{e} \\ \tilde{e}_0 \end{bmatrix} = \begin{bmatrix} y - A\hat{\xi} \\ z_0 - K\hat{\xi} \end{bmatrix} \tag{3.11}$$

Dispersion matrix of the estimated parameters:

$$D\left\{\begin{matrix} \hat{\xi} \\ \hat{\lambda} \end{matrix}\right\} = \sigma_0^2 N^{-1} - \sigma_0^2 N^{-1}K^T(P_0^{-1} + KN^{-1}K^T)^{-1}KN^{-1} = \sigma_0^2(N + K^T P_0 K)^{-1} \tag{3.12}$$

Dispersion matrix of the predicted errors:

$$\begin{aligned} D\{\tilde{e}\} &= \sigma_0^2(P^{-1} - A(N + K^T P_0 K)^{-1}A^T) = \sigma_0^2 Q_{\tilde{e}} \\ D\{\tilde{e}_0\} &= \sigma_0^2(P_0^{-1} - K(N + K^T P_0 K)^{-1}K^T) = \sigma_0^2 Q_{\tilde{e}_0} \\ C\{\tilde{e}, \tilde{e}_0\} &= -\sigma_0^2 A(N + K^T P_0 K)^{-1}K^T \end{aligned} \tag{3.13}$$

The estimated variance component:

$$\hat{\sigma}_0^2 = \frac{\tilde{e}^T P\tilde{e} + \tilde{e}_0^T P\tilde{e}_0}{n - m + l} \tag{3.14}$$

where:

$\hat{\sigma}_0^2$ is the estimated (reference) variance component,

n is the number of observations,

m is the number of unknowns, equaling the rank of $[A^T, K^T]$ and

l is the number of stochastic constraints.

Again, estimated dispersion matrices are obtained by replacing σ_0^2 with $\hat{\sigma}_0^2$ in Equations (3.12) and (3.13).

3.4 Alternative network adjustment approaches

To strengthen the network adjustment component of this research, alternative network adjustment approaches (e.g., MINOLESS, Partial-MINOLESS and BLIMPBE) ought to be considered and compared with the SCLESS, and used in order to test algorithms and software developed in this area (by Snow and Schaffrin, 2004). In this case we may proceed as follows.

In general, in the network adjustment scenario (e.g., the TAMDEF GPS network, which is derived exclusively from the observed GPS baseline vectors) the estimation of the coordinates from a (weighted) LESS will not be unique, even though the adjusted baseline vectors are unique (Snow and Schaffrin, 2004). In such a case, if one attempts to achieve uniqueness without affecting the adjustment, two alternatives are recommended (Snow and Schaffrin, 2004): (1) introduce a minimum set of constraints for the position coordinates "datum", or (2) apply a specific objective function on the set of LESSs that fulfills the "normal equations". In both alternatives, bias control and minimization for some (or all) coordinates should be taken into account, and is investigated in this research for the TAMDEF network.

3.4.1 Singular Least–Squares Solutions (SLESS) in a rank-deficient Gauss-Markov Model

For those geodetic networks that are derived from the observed GPS baseline vectors (such as TAMDEF), the rank-deficient (singular) least-squares adjustment (SLESS) was employed because of the presence of an inherent datum deficiency of three, due to the unknown translation/shift parameters. This type of adjustment will lead to a 3-D hyperspace of the LESS for the traditional normal equations (Schaffrin and Iz, 2002; Kuang, 1996). The rank–deficient Gauss–Markov model for the analysis of GPS networks (with datum deficiency) is given as:

Linear model (Gauss-Markov with rank-deficiency):

$$\underset{n\times 1}{y} = \underset{n\times m}{A}\ \underset{m\times 1}{\xi} + \underset{n\times 1}{e} \tag{3.15}$$

with

$$rank(A) = q < \min\{m, n\}$$

where:

$\underset{n\times 1}{y}$ is the $(n\times 1)$ observation vector,

$\underset{n\times m}{A}$ is the $(n\times m)$ "Jacobian" or design matrix,

$\underset{m\times 1}{\xi}$ is the $(m\times 1)$ unknown parameters vector,

$\underset{n\times 1}{e}$ is the $(n\times 1)$ random error vector,

and with the stochastic model for e described by:

$$e \sim (0, \sigma_0^2 P^{-1})$$

with unknown variance component σ_0^2 and given (positive-definite) weight matrix P.

Normal equations:

$$N\hat{\xi} = c \Rightarrow \hat{\xi} \in \{N^- c \,|\, NN^- N = N\} \tag{3.16}$$

N^- is any generalized inverse (or g-inverse) of N, and needs to be appropriately chosen.

Estimated parameters (SLESS of ξ):

$$\hat{\xi} = N^- c = N_{rs}^- c \tag{3.17}$$

where:

$$N_{rs}^- := N^- N (N^-)^T \neq N^- \text{ (in general).}$$

Here, N_{rs}^- is a reflexive symmetric generalized inverse of N, defined by $NN_{rs}^- N = N$ and $N_{rs}^- = N_{rs}^- N N_{rs}^- = (N_{rs}^-)^T$. It always holds: $rkN_{rs}^- = rkN = rkA = q$, whereas: $q \le rkN^- \le m$ for a general g-inverse.

The predicted errors or residuals:

$$\tilde{e} = y - A\hat{\xi} = (I_n - AN^- A^T P) y \tag{3.18}$$

independent of the chosen g-inverse N^-.

Dispersion matrix for the estimated parameters:

$$D\{\hat{\xi}\} = \sigma_0^2 N^- N (N^-)^T = \sigma_0^2 N_{rs}^- \tag{3.19}$$

Dispersion matrix for the predicted errors (independent of the chosen g-inverse N^-):

$$D\{\tilde{e}\} = \sigma_0^2 (P^{-1} - AN^- A^T) = \sigma_0^2 Q_{\tilde{e}} \tag{3.20}$$

independent of the chosen g-inverse N^-.

Estimated variance component:

$$\hat{\sigma}_0^2 = \frac{\tilde{e}^T P \tilde{e}}{n - q} \tag{3.21}$$

where:

$\hat{\sigma}_0^2$ is the estimated (reference) variance component,

n is the number of observations, and

q is the number of estimable unknowns, equaling the rank of A.

Obviously, estimated dispersion matrices are obtained from replacing σ_0^2 by $\hat{\sigma}_0^2$ in Equations (3.19) and (3.20).

For the SLESS, the estimated parameters and the dispersion matrix for these estimated parameters represent a variety of solutions, whereas the predicted errors or residuals, the dispersion matrix for these predicted errors, and the estimated variance

component are quantities that result from the computations of this procedure, in a unique way (i.e., independent of any datum choice in form of a specific g-inverse N^-).

In order to overcome the rank-deficiency problem and to affect minimization of the bias for certain coordinates of the TAMDEF network a rigorous examination and investigation of further extensions of the minimum-norm solution in the least-squares solution space were performed. Among the well-known or more recent alternative approaches as considered in this research and documented by Snow and Schaffrin (2004) as well as Schaffrin and Iz (2002) are: (1) the MINOLESS (Minimum-NOrm Least-Squares Solution); (2) the Partial-MINOLESS (Partial Minimum-NOrm Least-Squares Solution), which makes use of a selection matrix; and (3) the BLIMPBE (Best LInear Minimum Partial-Bias Estimation) that employs a complementary selection matrix.

3.4.2 MInimum-NOrm LEast-Squares Solution (MINOLESS)

This approach was used to perform a free network adjustment. The target function given by $\left\|\hat{\xi}\right\|^2 = \hat{\xi}^T\hat{\xi} = \min_{\hat{\xi}}\{N\hat{\xi} = c\}$ will guarantee that the vector containing the coordinate changes possesses the minimum norm. Furthermore, Snow and Schaffrin (2004) proved that the MINOLESS adjustment will generate a minimum Mean Square Error (MSE) risk on average. Another reason for using MINOLESS as a network adjustment alternative for TAMDEF is that this method belongs to the larger class of LESSs. Thus, the adjusted observations will be an unbiased estimate of the "true" observables.

Linear model (Gauss-Markov) with rank-deficiency:

$$\underset{n\times 1}{y} = \underset{n\times m}{A}\ \underset{m\times 1}{\xi} + \underset{n\times 1}{e} \tag{3.22}$$

with

$$rank(A) = q < \min\{m, n\}$$

and with the stochastic model for e, described before by:

$$e \sim (0, \sigma_0^2 P^{-1})$$

Estimated parameters, based on $\left\|\hat{\xi}\right\|^2 = \hat{\xi}^T\hat{\xi} = \min_{\hat{\xi}}\{N\hat{\xi} = c\}$:

$$\hat{\xi}_{MINOLESS} = N(NN)^- c = N^+ c, \quad but \quad N(NN)^- \neq N^+ \tag{3.23}$$

N^+ denotes the MOORE-PENROSE or pseudo-inverse, $N^+ \in \left\{N_{rs}^-\right\}$

In contrast $N(NN)^-$ is a reflexive (but not symmetric) g-inverse.

Dispersion matrix for the estimated parameters:

$$D\{\hat{\xi}_{MINOLESS}\} = \sigma_0^2 N(NN)^- N[(NN)^-]^T N = \sigma_0^2 N^+ \tag{3.24}$$

The residual vector $\tilde{e}$, its dispersion matrix $D\{\tilde{e}\}$, and the estimated variance component $\hat{\sigma}_0^2$ follow from the equations (3.18), (3.20) and (3.21).

3.4.3 Partial MInimum–NOrm LEast–Squares Solution (Partial–MINOLESS)

This approach is referred to as the S-weighted MINOLESS, and it will also be used to adjust the TAMDEF network. The selection matrix (S) is strategically constructed to allow for the selection of the primary points; if the TAMDEF sites FTP1, MCM4 and ROB1 are selected, then the $rank(S) = 9$. Snow and Schaffrin (2004) proved that the S-weighted MINOLESS is uniquely defined whenever the matrix ($S + N$) is invertible. An additional motivation for using this approach as a network adjustment for TAMDEF is that "the Partial-MINOLESS, where $S := Diag(1,\ldots,1,0,\ldots,0)$ provides linear minimum bias estimates collectively for all those coordinates that do not participate in the "*partial minimum norm*" process" (Corollary 7 of Snow and Schaffrin, 2004). Among all the LESSs, it also minimizes the partial trace of the dispersion matrix associated with the selected parameters (Koch, 1999). However, this approach will generally not turn out to be "best" (in this class) because of the overall Mean Squared Error risk.

Linear model (Gauss-Markov) with rank-deficiency:

$$\underset{n\times 1}{y} = \underset{n\times m}{A}\,\underset{m\times 1}{\xi} + \underset{n\times 1}{e} \tag{3.25}$$

with

$$rank(A) = q < \min\{m, n\}$$

and with the stochastic model for e, described before by:

$$e \sim (0, \sigma_0^2 P^{-1})$$

Estimated parameters, based on $\left\|\hat{\xi}\right\|_S^2 = \hat{\xi}^T S \hat{\xi} = \min_{\hat{\xi}}\{N\hat{\xi} = c\}$:

$$\hat{\tilde{\xi}}_{P-MINOLESS} = (N + SE^T ES)^{-1} c \tag{3.26}$$

where:

$(N + SE^T ES)^{-1}$ is a symmetric g-inverse of N, with maximum rank (and thus not reflexive).

Dispersion matrix for the estimated parameter:

$$D\{\hat{\tilde{\xi}}_{P-MINOLESS}\} = \sigma_0^2 (N + SE^T ES)^{-1} N (N + SE^T ES)^{-1} \tag{3.27}$$

Here, S is a "standard selection matrix", and E is a particular case of the matrix K used for SCLESS, where $AE^T = 0$ and $rank(A) + rank(E) = m = rk[A^T, E^T]$.

As for all forms of LESS, the residual vector $\tilde{e}$, its dispersion matrix $D\{\tilde{e}\}$, and the estimated variance component $\hat{\sigma}_0^2$ will follow from (3.18), (3.20) and (3.21).

3.4.4 Best LInear Minimum Partial–Bias Estimation (BLIMPBE)

Schaffrin and Iz (2002) developed the BLIMPBE estimator which, generally, cannot be considered as a LESS. It is a more robust estimator and, as the "partial" term implies, it is characterized by securing a "*minimum bias*" for a given subset of estimated parameters (e.g., for a certain group of point coordinates). Furthermore, BLIMPBE relies

on the appropriate choice of the selection matrix (S), which ought to be constructed so that all the secondary points are selected, hence minimizing their bias. As can be seen, this was already done in the previous approach (Partial-MINOLESS); however, the new solution generated by the BLIMPBE will be the "*best*" among other minimum partial-bias solutions in terms of its MSE-risk. In other words, if we compare the trace of the dispersion matrix generated with the BLIMPBE, it will be smaller than the one generated with the Partial-MINOLESS.

The adjusted observations of the BLIMPBE will also differ, in general, from those of the SLESS solutions, such as the MINOLESS or Partial-MINOLESS. BLIMPBE will simply reproduce coordinates of those points that were not selected, returning a zero variance for these points. This is what is called the reproducing or zero variance property of the BLIMPBE.

Linear model (Gauss-Markov) with rank-deficiency:

$$\underset{n\times 1}{y} = \underset{n\times m}{A}\ \underset{m\times 1}{\xi} + \underset{n\times 1}{e} \tag{3.28}$$

with $rank(A) = q < \min\{m,n\}$, and with the stochastic model for e, described before by:

$$e \sim (0, \sigma_0^2 P^{-1})$$

Estimated parameters (BLIMPBE of ξ):

$$\hat{\tilde{\xi}}_{BLIMPBE} = [\bar{S}N(N\bar{S}N\bar{S}N)^{-}N\bar{S}]c \tag{3.29}$$

with $\bar{S}$ as suitable "selection matrix".

Here the double hat indicates that $\hat{\tilde{\xi}}_{BLIMPBE}$ does not belong to the class of LESSs.

Dispersion matrix for the estimated parameters:

$$D\{\hat{\tilde{\xi}}_{BLIMPBE}\} = \sigma_0^2[\bar{S}N(N\bar{S}N\bar{S}N)^{-}N\bar{S}] \tag{3.30}$$

Mean Squared Error matrix of the estimates:

$$MSE\{\hat{\tilde{\xi}}_{BLIMPBE}\} = \sigma_0^2[\bar{S}N(N\bar{S}N\bar{S}N)^{-}N\bar{S}] + \beta\beta^T \tag{3.31}$$

Bias vector:

$$\beta = -[I_m - \bar{S}N(N\bar{S}N\bar{S}N)^{-}N\bar{S}N]\xi \tag{3.32}$$

The residual vector $\tilde{\tilde{e}}$, its dispersion matrix $D\{\tilde{\tilde{e}}\}$, and the estimated variance component $\hat{\tilde{\sigma}}_0^2$ may now be derived similarly as for the LESSs. They will turn out different, however, as long as $rk(\bar{S}N) < rkN$ holds true (i.e., almost always).

3.5 Outlier detection and hypothesis testing

As a final point, it should be mentioned here that the least–squares adjustment software used in this research is capable of performing a complete outlier analysis (see Tables 3.5 and 3.6) for the *a priori* solutions (GPS coordinates) (Snow and Schaffrin, 2003). This will facilitate outlier detection, which should be conducted before the final coordinate parameters are estimated within PAGES software.

Model I (constrains the outlier vector to zero)	$\underset{n\times 1}{y} = \underset{n\times m}{A}\,\underset{m\times 1}{\xi} + \underset{n\times 3}{H_k}\,\delta^{(k)} + \underset{n\times 1}{e}$ $0 = \begin{bmatrix} 0 & I_3 \end{bmatrix} \begin{bmatrix} \xi \\ \delta^{(k)} \end{bmatrix}$
Stochastic model	$e \sim (0, \sigma_0^2 P^{-1})$
Outlier vector set to:	$\delta^{(k)} = \begin{bmatrix} 0 & 0 & 0 \end{bmatrix}^T$
H_k - is a $n \times 3$ unit matrix that has the identity matrix for its k^{th} 3×3 block and zeros elsewhere $\delta^{(k)}$ - is the 3×1 outlier vector associated with the k^{th} GPS baseline vector observation	
Model II (no constraints on the outlier)	$\underset{n\times 1}{y} = \underset{n\times m}{A}\,\underset{m\times 1}{\xi} + \underset{n\times 3}{H_k}\,\delta^{(k)} + \underset{n\times 1}{e}$
Stochastic model	$e \sim (0, \sigma_0^2 P^{-1})$
Outlier vector estimate:	$\hat{\delta}^{(k)} = \left[H_k^T (P Q_{\tilde{e}} P) H_k \right]^{-1} H_k^T P \tilde{e}$
$\tilde{e}$ - is the residual vector computed by $\tilde{e} = y - A\hat{\xi} = (I_n - AN^{-}A^T P)y$ from Model I $Q_{\tilde{e}}$ - is the cofactor matrix of $\tilde{e}$ such that $\tilde{e} = (Q_{\tilde{e}} P)y$ with $Q_{\tilde{e}} = P^{-1} - AN^{-}A^T$	

Table 3.5: Outlier detection (Snow and Schaffrin, 2003).

Deciding whether or not the k[th] GPS baseline vector observation is flagged as an outlier depends on the results from the hypothesis testing. For the TAMDEF network, the hypothesis test and the associated test statistics are given in Table 3.6.

Hypothesis test	$H_0^k : E\{\hat{\delta}^{(k)}\} = \begin{bmatrix} 0 & 0 & 0 \end{bmatrix}^T$ vs. $H_a^k : E\{\hat{\delta}^{(k)}\} \neq \begin{bmatrix} 0 & 0 & 0 \end{bmatrix}^T$
Test statistic	$T_k = \dfrac{R_k/3}{(\Omega - R_k)/(n-q-3)} \sim F(3, n-q-3)$ under H_0^k
Decision	$T_k \leq F_\alpha(3, n-q-3) \Rightarrow$ Accept H_0^k $T_k > F_\alpha(3, n-q-3) \Rightarrow$ Reject H_0^k at the chosen level of error probability (**α**)
R_k - scalars computed by $R_k := \hat{\delta}^{(k)^T} \left[H_k^T (P Q_{\tilde{e}} P) H_k \right] \hat{\delta}^{(k)} = \tilde{e}^T P H_k \hat{\delta}^{(k)}$ Ω - is the quadratic form $\tilde{e}^T P \tilde{e}$ computed from $\tilde{e} = y - A\hat{\xi} = (I_n - AN^{-}A^T P)y$, thus $\Omega = \hat{\sigma}_0^2 (n-q)$	

Table 3.6: Hypothesis testing and associated test statistics.

3.6 TAMDEF link to the International Terrestrial Reference Frame (ITRF00)

Present-day studies recognize that the variations (e.g., up, down or horizontal) of any local point on the Earth should be measured from a global point of view and with respect to a well-defined, global reference frame (http://lareg.ensg.ign.fr/ITRF.html.)

The Scientific Committee on Antarctic Research (SCAR) has been working on linking of Antarctica to the ITRF (Dietrich *et al.* 2001; Dietrich, 2001; Dietrich and Rülke, 2002; Rülke *et al.* 2007; Rülke *et al.* 2008; Dietrich and Rülke, 2008). However, any results generated by a local or regional GPS network in Antarctica (e.g., the TAMDEF network) will represent a great contribution to the SCAR team efforts. In order to establish the link between the TAMDEF Antarctic stations and other ITRF00 stations inside and outside the Antarctic tectonic plate, this research will proceed as stipulated in Cases I-IV of Section 3.2 and as explained in the following sections (Section 3.6.1 and 3.6.2).

3.6.1. Helmert blocking least–squares adjustment

The technique known among geodesist as "*Helmert blocking"* was first described by Helmert (1880). This is basically a technique for breaking up a least-squares adjustment problem by solving the normal equations (described in previous sections), which are too big to be managed in a single computation, in many smaller size portions with potentially large savings in computer storage and CPU requirements. A good description of the application of this technique was presented by Wolf (1978), including the original instructions given by Helmert for using this approach. It is well known that several other strategies exist for dividing a large survey network into pieces of manageable size for adjustment. However, the method of Helmert blocking has the crucial advantage of producing not only a set of coordinate estimates, but also a complete covariance matrix that allows relating the random errors between estimated coordinates in the network.

Consequently, Helmert blocking starts by dividing a survey network into a series of subnets or blocks. Usually, the requirements for dividing survey data into blocks are fairly simple and each observation must be included in one, and only one, block. In traditional surveying, each observation can be assigned to a block fairly arbitrarily; however, where GPS measurements are concerned, the situation is more complex because each simultaneously observed GPS baseline has, in principal, non-zero covariance terms with every other baseline observed at the same time. These off diagonal covariance terms are preserved; as they are used for all sessions processed through PAGES. This occurs because; in session processing all baselines processed from all simultaneously-logged GPS carrier phase data are, in effect, inseparable.

3.6.2. GPSCOM processing tool

GPSCOM is a program for the combined adjustment of multiple GPS data sets, initially processed by the PAGES software, described in Section 2.4 http://www.ngs.noaa.gov/GRD/GPS/DOC/gpscom/gpscom.html. GPSCOM is a simple Helmert-blocking (refer to Section 3.6.1) normal equations processor, which combines multiple GPS data sets that have initially been processed by PAGES to form and partially reduce normal equations by eliminating numerous nuisance parameters that are not generally of interest in a large global adjustment. The normal equations elements for the global parameters, i.e., those to be passed on to a combined adjustment, are written by

PAGES into a normal equations file, and these become the basic input data for the program GPSCOM (see Figure 3.5). GPSCOM combines the normal equations matrices properly, so can be considered a direct descendent of a prototype program that had originally been coded by (Dillinger, 1978). Moreover, since only GPS data will be included in the adjustment, the network is reasonably homogeneous, and determining a realistic set of weights is not considered to be a major problem. All sets of coordinates used in the processing refer to ITRF00. Thus GPSCOM, by means of the Helmert-blocking, is the routine which will realize the transformation and linkage of the TAMDEF sites to the IGS sites (see Cases I-IV), resulting in a homogeneous global network with coordinates referred to ITRF00 at a specific reference epoch.

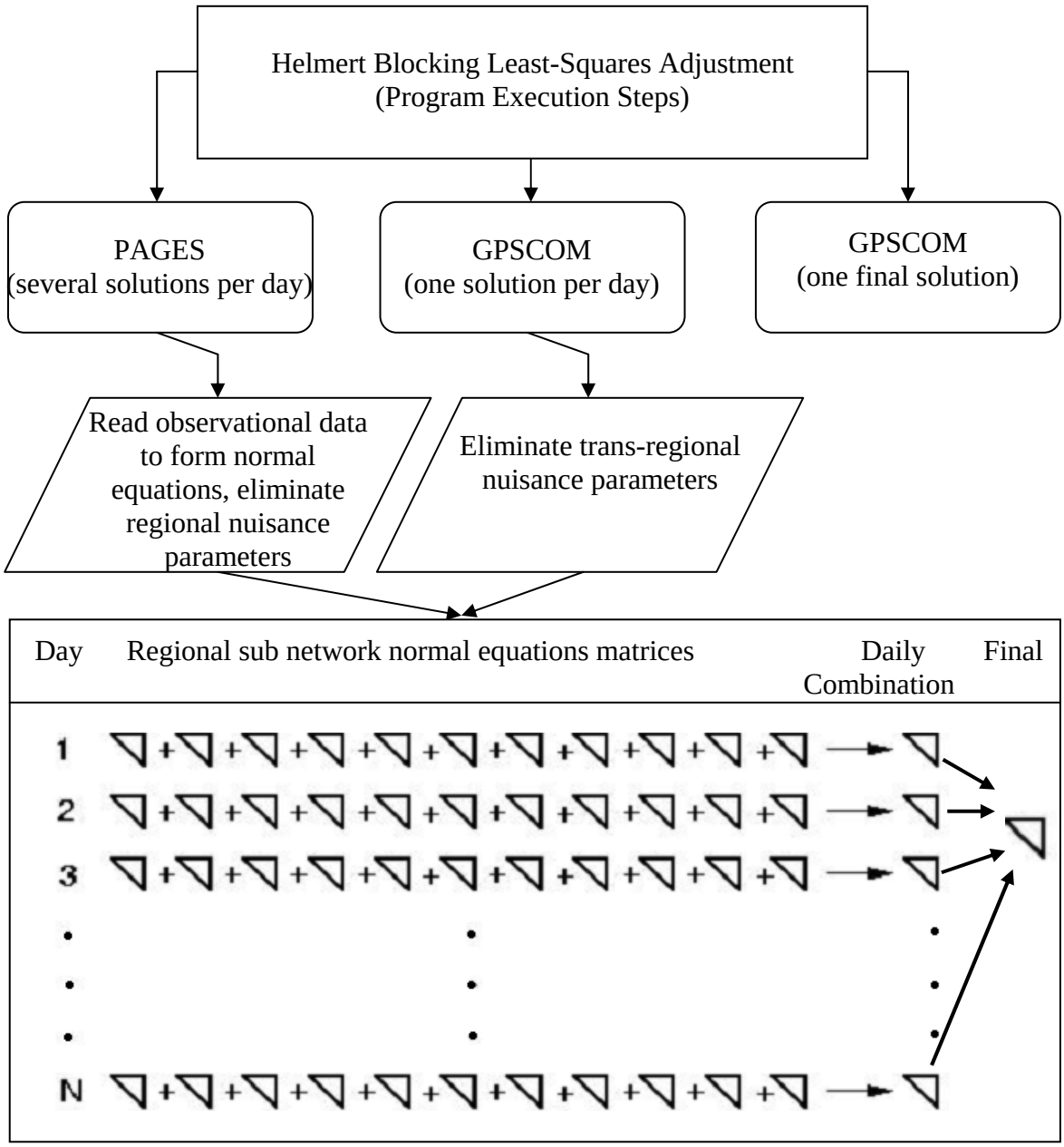

Figure 3.5: Helmert blocking least-squares adjustment by GPSCOM.

CHAPTER 4

TROPOSPHERIC ANALYSIS

4.1 Introduction

The atmospheric effects remain the main limitation to the precision of GPS in navigation (meter accuracy), surveying engineering (centimeter accuracy), geodesy and geophysics (millimeter accuracy). Atmospheric effects are present in any GPS data, and they can vary with location and the seasons as well as the time of the year. The challenge to account for them increases with the baseline length (e.g., 50 to 60 km for the troposphere and 5-10 km for ionosphere). The proposed atmospheric analysis of this research will focus on the optimal modelling of the troposphere and precipitable water vapor (PWV) by using the appropriate processing schemes inside the PAGES software (refer to Chapter 2) for the TAMDEF network. Furthermore, the use of external meteorological information, such as surface temperature and pressure, are considered in order to improve/refine the results of the tropospheric analysis.

4.2 Propagation of GPS signals

The GPS satellites (orbiting at an altitude of about 20200km) transmit signals at two different carrier frequencies in the radio band: the L1-signal (1575.42 MHz) and the L2-signal (1227.60 MHz). Notably, the atmospheric layers along the entire path from the satellite to the terrain-borne GPS antennae significantly influence the GPS signals. The ionosphere (upper part of the atmosphere) is a dispersive medium for frequencies in the radio band; that is, the delay due to ionosphere depends directly on the frequency of the GPS signal. To remedy this, the so-called iono-free linear combination of the two carriers can be formed, in order to eliminate first order of the ionospheric effects (refer to Section 2.4.1). On the other hand, the troposphere (the lower part of the atmosphere) is neutral and non-dispersive for radio frequency signals. Hence, the tropospheric delay is independent of the carrier frequency and, therefore, cannot be eliminated with multi-frequency measurements.

4.3 Neutral atmosphere and tropospheric path delay

The atmospheric layer between the earth's surface and the ionosphere is usually called the *neutral atmosphere*. The *tropospheric path delay* is defined as the ratio of the delay of the signal propagating through the neutral atmosphere to a signal propagating with the speed of light in the vacuum (see Figure 4.1). This delay is a function of the tropospheric refractive index, n (Seeber, 1993; Kaplan, 1996). The geometry of the delay can be formulated from Figure 4.1 and is described as follows:

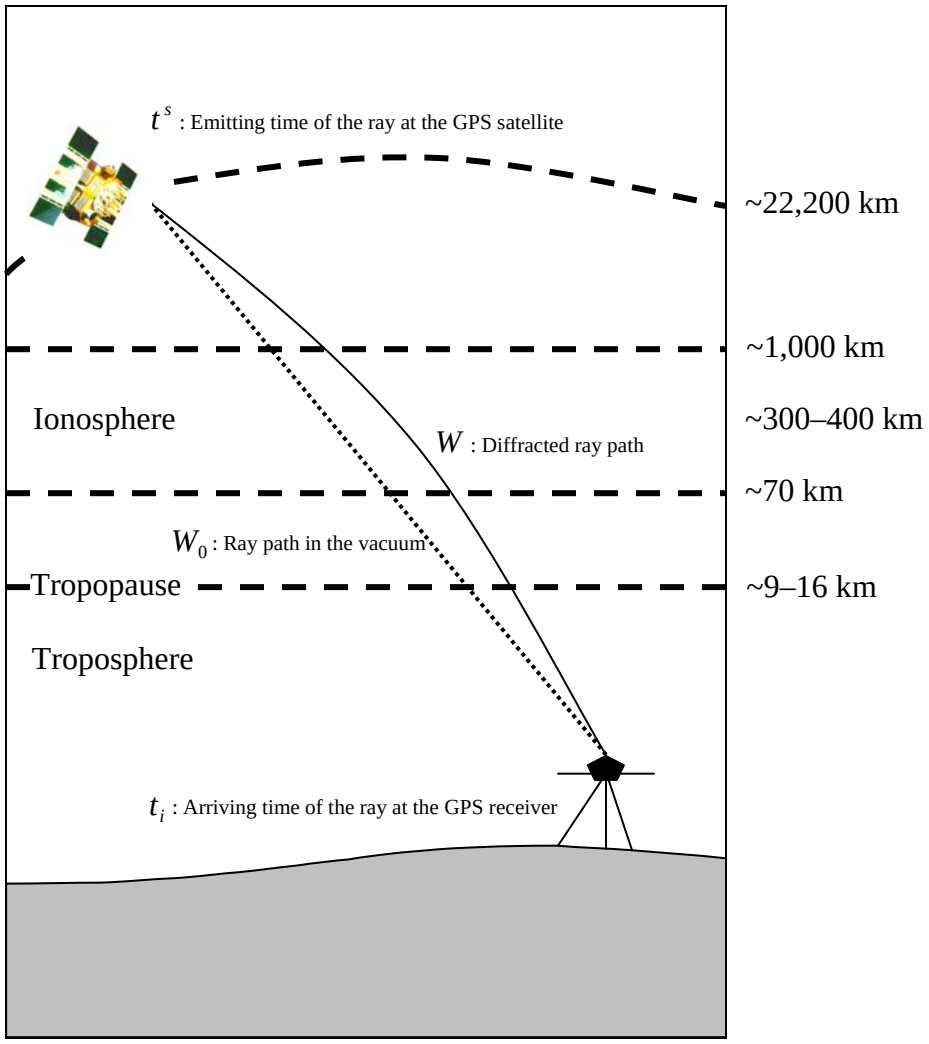

Figure 4.1: Propagation of a GPS signal through the atmosphere.

The time difference between the emission of the GPS signal from the GPS satellite and its arrival at the GPS receiver is defined by

$$\Delta t = t_i - t^s = \int_{t^s}^{t_i} dt = \int_W \frac{1}{v} ds \tag{4.1}$$

where:

t^s is the emitting time of the ray at the GPS satellite,

t_i is the arriving time of the ray at the GPS receiver,

W is the propagation path of the GPS ray,

v is the propagation velocity of the GPS ray dependent on W.

Let us consider the refractive index, n, defined by:

$$n = \frac{c}{v} \tag{4.2}$$

where:

c is the speed of light in vacuum.

Then, the time difference given by Equation (4.1) can be given as:

$$\Delta t = t_i - t^s = \frac{1}{c}\int_W n(s)ds \tag{4.3}$$

Furthermore, by means of Equation (4.3), the Radio-Distance (RD) is written as

$$RD = c(t_i - t^s) = \int_W n(s)ds \tag{4.4}$$

whereas the Euclidean-Distance (ED) is given by (see Figure 4.1):

$$ED = \int_{W_0} ds \tag{4.5}$$

Finally, the tropospheric path delay (Δ_{PD}) can be expressed in terms of the refractivity (N) by:

$$\Delta_{PD} = 10^{-6}\int_W N ds \tag{4.6}$$

with

$$N = 10^6 \cdot (n-1) \tag{4.7}$$

The tropospheric path delay (Δ_{PD}) expressed by Equation 4.6, consists of two components: (1) the hydrostatic (or *dry*) component, which is dependent on the dry air gases in the atmosphere and accounts for approximately 90% of the delay; and (2) the *wet* component that depends upon the moisture content of the atmosphere and contains significant levels of water vapor; it accounts for the remaining effect of the delay (Emardson, 1998; Dodson *et al.* 1996). Of the two tropospheric corrections, the wet component is more difficult to model and to estimate than the dry component; this is addressed in the following section.

4.3.1 Tropospheric wet delay estimation

Depending on the length of the baseline among GPS sites, Schenewerk (2004) provides some of the recommended specifications for tropospheric estimation as implemented in the PAGES software, and shown in Table 4.1.

Baseline length	Action recommended in PAGES
< 1 km	No tropospheric estimation
< 50 km	Use relative tropospheric corrections (i.e., tropo. corrections at only some sites).
> 50 km	Consider absolute tropospheric corrections (i.e., tropo. corrections at all sites, even if only one baseline exceeds this limit).

Table 4.1: Troposphere estimation corrections recommended in PAGES.

According to the specifications of Table 4.1, and considering that most of the TAMDEF baselines are longer than 50 km long, absolute tropospheric corrections were estimated with PAGES. Also, tropospheric models were used that are dependent on parameters, such as temperature, barometric pressure and relative humidity. It is recommended that these parameters should represent the mean values of an entire column of air, but regularly they are surface meteorological values (Schenewerk, 2004). Thus,

PAGES was set up to properly model the troposphere and remove the zenith dry part of the troposphere (Z_{dry}); next, the corrections for the zenith-wet delay (Z_{wet}) were only estimated to analyse their influence on the final positional results of TAMDEF.

Since GPS signals pass through more of the neutral atmosphere as the satellite elevation angle (E) decreases, usually mapping functions are used to correct the zenith delay to the slant delay following Equation (4.8)

$$T(E) = m_{Dry}(E) \cdot Z_{Dry} + m_{wet}(E) \cdot Z_{wet} \tag{4.8}$$

where:

$m_{Dry}(E)$ is the mapping function associated with Z_{dry},

$m_{wet}(E)$ is the mapping function associated with Z_{wet}.

To compare the impact of the mapping function used, three essential mapping functions coded inside PAGES software with two different tropospheric models were investigated and compared:

1) The Niell mapping function, Niell (1996) with Saastamoinen model, Saastamoinen (1973),

2) The CfA-2.2 mapping function (Davis *et al.* 1985) with Saastamoinen model, Saastamoinen (1973), and

3) The Marini mapping function with the Marini model, Marini (1972).

The SPWL (Step-Piece-Wise Linear) strategy at a 3-hour interval that considers the time-dependent behavior of the neutral atmospheric delay (refer to p. 73 of Lancaster and Salkauskas, 1986) was followed. Furthermore, the use of external surface temperature and pressure was considered via external meteorological files.

From the iono-free DD observation equation given by (2.5), the neutral atmospheric delay (nuisance) parameters associated with the ground stations (i and j), denoted by $\delta Z_{wet,i}$ and $\delta Z_{wet,j}$, appear as one-way neutral atmospheric delays, according to Marshall *et al.* (2001), namely:

$$T_{ij}^{kl} = [T(E_i^k) - T(E_i^l)] - [T(E_j^k) - T(E_j^l)] \tag{4.9}$$

By using Equation (4.9), any of the four delays (e.g., $T(E_i^k)$) can be linearized as follows:

$$T(E_i^k) = m_{Dry}(E_i^k) Z_{Dry,i} + m_{wet}(E_i^k) Z_{wet,i} + \left(\frac{\partial \Phi_{i,j}^{kl}}{\partial Z_{wet,i}} \right) \delta Z_{wet,i} \tag{4.10}$$

where $m_{Dry}(E)$ and $m_{wet}(E)$ are mapping functions defined above, and $\left(\frac{\partial \Phi_{i,j}^{kl}}{\partial Z_{wet,i}} \right) \delta Z_{wet,i}$ is the time-varying effect due to the zenith wet delay; this correction is estimated using the chosen mapping function; $m_{wet}(E)$, whereas the varying part $\delta Z_{wet,j}$ is evaluated using the corresponding tropospheric model. A similar expression on the basis of $\delta Z_{wet,i}$ can be derived for $T(E_i^l)$, while the neutral atmospheric delay parameter $\delta Z_{wet,j}$ appears in the corresponding expressions for $T(E_j^k)$ and $T(E_j^l)$.

4.4 Troposphere mapping functions

The path delay introduced in Equation (4.6) corresponds to a slant delay from the satellite to the station. Thus, the mapping function describes the transformation from the delay at zenith direction to a slant delay at different elevation angles. Hence, Equation (4.6) can be transformed to

$$\Delta_{PD} = m(E) \cdot \Delta^{o}_{PD} \tag{4.11}$$

where:

Δ_{PD} is the slant path delay,

$m(E)$ is the corresponding mapping function, and

Δ^{o}_{PD} is the zenithal path delay.

Both the parametrization type of the three mapping functions listed above and the minimum elevation of validity is shown in Table 4.2.

Mapping function	Minimum elevation (degrees)	Coefficient	
		Dry	Wet
Marini	10	(Tabulated)	-
CfA-2.2	10	(Tabulated)	-
Niell	3	Day of year, φ, H	φ

Table 4.2: Troposphere mapping functions parametrization (Troller, 2004).

From Table 4.2, one can see that the Marini and CfA-2.2 mapping functions used tabulated constants (see Sections 4.4.2 and 4.4.3), while Niell (1996) developed a mapping function completely independent of such parameters, instead depending on the season and geographic location with latitude (φ) and orthometric height (H) (see Section 4.4.1).

4.4.1 Niell mapping function with the Saastamoinen model

In the Saastamoinen model (Saastamoinen 1973), the refractivity can be deduced from the gas laws (Hofmann-Wellenhof *et al.* 1997). The Saastamoinen model can be used to find the phase changes due, in particular, to relative humidity, temperature and relative pressure. It is assumed that the atmosphere is divided spatially into columns with a certain average value of the three variables. Because of the different behavior of the lower as compared to the higher atmosphere, Niell (1996) developed a mapping function given by Equations (4.12) and (4.13):

For the dry component:

$$m_{dry}Niell(E) = \frac{1+\dfrac{a_{dry}}{1+\dfrac{b_{dry}}{1+c_{dry}}}}{\sin(E)+\dfrac{a_{dry}}{\sin(E)+\dfrac{b_{dry}}{\sin(E)+c_{dry}}}} \tag{4.12}$$

with

$$a_{dry} = \left[1.2320 + 0.0139\cdot\cos(\varphi) - 0.0209\cdot h + 0.00215\cdot(T-283)\right]\cdot 10^{-3}$$
$$b_{dry} = \left[3.1612 - 0.1600\cdot\cos(\varphi) - 0.0331\cdot h + 0.00206\cdot(T-283)\right]\cdot 10^{-3}$$
$$c_{dry} = \left[71.244 - 4.2930\cdot\cos(\varphi) - 0.1490\cdot h - 0.00210\cdot(T-283)\right]\cdot 10^{-3}$$

For the wet component:

$$m_{wet}Niell(E) = \frac{1+\dfrac{a_{wet}}{1+\dfrac{b_{wet}}{1+c_{wet}}}}{\sin(E)+\dfrac{a_{wet}}{\sin(E)+\dfrac{b_{wet}}{\sin(E)+c_{wet}}}} \tag{4.13}$$

with

$a_{wet} = 2.53\cdot 10^{-5}$; $b_{wet} = 5.49\cdot 10^{-3}$ and $c_{wet} = 1.14\cdot 10^{-3}$.

where:

a_{dry}, b_{dry}, c_{dry}, a_{wet}, b_{wet} and c_{wet} are coefficients that depend on the latitude (φ) of the site,

E is the elevation angle at the site,

h is the ellipsoidal height.

4.4.2 CfA-2.2 mapping function with the Saastamoinen model

The hydrostatic mapping function developed at the Harvard-Smithsonian Center for Astrophysics (Davis *et al.* 1985), also known as CfA-2.2, is based on the continued fraction form of Marini (Marini, 1972). Its inputs are the barometric pressure (in mb), observation elevation (in rad), ellipsoidal height (in m), relative humidity and temperature (in degrees Celsius). Even though this mapping function was developed for mapping the hydrostatic zenith delay only, it can also be used for the wet delay. This is effectively equivalent to Chao wet mapping function (Chao 1973), which only requires the observation elevation and is given by Equations (4.14) and (4.15):

For the dry component:

$$m_{dry}CfA = \frac{1}{\sin(E) + \dfrac{a_{dry}}{\tan(E) + \dfrac{b_{dry}}{\sin(E) + c_{dry}}}} \tag{4.14}$$

with

$$a_{dry} = (0.001185) \cdot (1 + 0.6071^{-4} \cdot (P_0 - 1000) - 0.1471^{-3} \cdot (e_0) + 0.3072^{-2} \cdot (T_0 - 20) + 0.1965^{-1} \cdot (\beta + 6.5) - 0.5645^{-2} \cdot (h_T - 11.231))$$

$$b_{dry} = (0.001144) \cdot (1 + 0.1164^{-4} \cdot (P_0 - 1000) + 0.2795^{-3} \cdot (e_0) + 0.3109^{-2} \cdot (T_0 - 20) + 0.3038^{-1} \cdot (\beta + 6.5) - 0.1217^{-2} \cdot (h_T - 11.231))$$

$$c_{dry} = -0.0090 .$$

For the wet component:

$$m_{wet}CfA(E) = \frac{1}{\sin(E) + \dfrac{a_{wet}}{\tan(E) + b_{wet}}} \tag{4.15}$$

with

$$a_{wet} = 0.001185 + 0.6071 \cdot 10^{-4}(P_0 - 1000) - 0.1471 \cdot 10^{-3} \cdot e_0 + 0.3072 \cdot 10^{-2}(T_0 - 20) + 0.1965 \cdot 10^{-1}(\beta + 6.5) - 0.5645 \cdot 10^{-2}(h_T - 11.231)$$

$$b_{wet} = 0.00114 \cdot [1 + 0.1164 \cdot 10^{-4}(P_0 - 1000) + 0.2795 \cdot 10^{-3} \cdot e_0 + 0.3109 \cdot 10^{-2}(T_0 - 20) + 0.3038 \cdot 10^{-1}(\beta + 6.5) - 0.1217 \cdot 10^{-1}(h_T - 11.231)]$$

In the expressions for a_{wet} and b_{wet}, β is the tropospheric temperature lapse rate ($^\circ C / km$), h_T is the ellipsoidal height of the troposphere (km), T_0 is the surface temperature ($^\circ C$), P_0 is the barometric pressure (mb) and (e_0) is the partial pressure of water vapor in mb.

4.4.3 Marini mapping function with the Marini model

Marini (1972) proposed a mapping function in form of Equations (4.16) and (4.17). The Marini model shows that the troposphere path delay at different elevation angles could be expressed as a continued fraction in terms of the sine of this elevation angle (E), leading to the so-called Marini mapping function.

For the dry component:

$$m_{dry}Mar(E) = \frac{1}{\sin(E) + \dfrac{a_{dry}}{\sin(E) + \dfrac{b_{dry}}{\sin(E) + \dfrac{c_{dry}}{\sin(E) + \ldots}}}} \tag{4.16}$$

with

$$c_{dry} = -0.0090 .$$

For the wet component:

$$m_{wet}Mar(E) = \frac{1}{\sin(E) + \frac{a_{wet}}{\sin(E) + \frac{b_{wet}}{\sin(E) + \frac{c_{wet}}{\sin(E) + \ldots}}}} \tag{4.17}$$

where a_{dry}, b_{dry}, a_{wet} and b_{wet} are constant coefficients (the same as for the CfA-2.2 mapping function described above).

Several researchers have improved these constants with only small changes on the basic Equation (4.17) (e.g., Chao, 1973; Davis *et al.* 1985; Ifadis, 1986, 1987). But, so far, all mapping functions are based on meteorological parameters. According to Troller (2004), the accuracy of all mapping functions is ±1cm or better where the main difference is the elevation angle range for which this accuracy is valid.

4.5 Precipitable water vapor (PWV) estimation

The integrated amount of water vapor in the zenith direction is called *Precipitable Water Vapor* (PWV). PWV is approximately proportional to the tropospheric path delay, which can be estimated from GPS measurements (Bevis *et al.* 1992). Water vapor and its spatial distribution play an essential role in weather forecast models. GPS radio signals are delayed by the atmospheric layers (ionosphere and troposphere) on their way from the satellite to the receiver antenna on the ground. The delay caused by the neutral atmosphere can be used to retrieve the PWV from the ground-based GPS observations collected at sites with known locations. The integrated PWV and its temporal variation are the prime focus of this chapter. In the approach to estimate PWV, the time-varying part of the Z_{wet}, which is coupled with the PWV above the GPS receiver, was estimated using three different mapping functions, namely $m_{wet}Niell(E)$, $m_{wet}CfA(E)$ and $m_{wet}Mar(E)$ (described in Sections 4.4.1 to 4.4.3). On the other hand, the constant part was evaluated using the corresponding tropospheric models (i.e. Saastamoinen and Marini), and it was subsequently transformed to PWV following the standard approach as proposed by Bevis *et al.* (1992):

$$PWV_{GPS} = \left(Z_{wet}\right) \frac{10^6}{w_{den} \cdot \frac{sgc}{mol_2 kg} \left(\frac{k_3}{T_m} + k_2 p \right)} \tag{4.18}$$

where:

w_{den} is the density of water (kg/m^3),

sgc is the specific gas constant for water vapor [$(m^3 \cdot mbar)/(kg \cdot K)$] = universal gas constant / ($18 kg/kmole$) and $mol_2 kg$ for water $18 kg/kmole$,

k_3 ($\deg rees \cdot K^2 / mbar$) and $k_2 p$ ($\deg rees \cdot K / mbar$) are the refractivity constants,

T_m is the mean temperature.

The significance of Equation (4.18), according to Bevis *et al.* (1996), lies in the fact that it allows for a transformation of the PWV estimate, derived from an operational numerical weather model, into an estimate of Z_{wet}. In order to perform these transformations one must be able to form a prior estimate of the time varying parameter on the right hand side of Equation (4.18), which is a function of various local physical constants and the mean temperature (T_m) of the atmosphere. These values can be obtained from the vertical profiles as shown by Wang *et al.* (2005):

$$T_m \approx \frac{\sum_{i=1}^{N} (\frac{e_i}{T_i} \Delta p_i)}{\sum_{i=1}^{N} (\frac{e_i}{T_i^2} \Delta p_i)} \tag{4.19}$$

where:

e is the water vapor pressure,

T is the temperature.

Equation (4.19) can also be expressed in terms of the observations of the height (z) instead of the pressure (p). In this experiment, we used pressure, since the observations of p are readily available, and both are related to each other assuming a hydrostatic equilibrium (which is valid for Antarctica).

However, in order to obtain the T_m value in Equation (4.18), Bevis *et al.* (1994) developed the following linear relationship between T_m and the surface temperature (T_s), which was derived from radiosonde data at 13 U.S. sites over a 2-year period with an RMS error of ~4.74 K:

$$T_m = a + bT_s \tag{4.20}$$

where a and b generally depend on the region.

In Equation (4.20), the coefficients *a* and *b* were generated by Bevis *et al.* (1994) specifically for the United States (*a* = 70.2 and *b* = 0.72). The PAGES software uses these coefficients in the procedure to estimate water vapor from the wet zenith delay. However, these values might not be the appropriate ones for the Antarctic TAMDEF stations since the tropospheric conditions there are different from those experienced at GPS stations across the US. For example: Liou and Teng (2001) and Liu *et al.* (2005) obtained values of *a* = -31.5 and *b* = 1.07 for Taipei, and *a* = 44.05 and *b* = 0.81 for the Tibetan Plateau, respectively. Wang *et al.* (2005) provides a complete analysis of the relative error on GPS PWV due to errors in T_m using Equation (4.19), coming up with Equation (4.21) considering the fact that the relation between k_2 / k_3 is small ($\sim 5.9 \times 10^{-5} K^{-1}$).

$$\frac{\Delta PWV_{GPS}}{PWV_{GPS}} = \frac{1}{1 + \frac{k_2}{k_3} T_m} * \frac{\Delta T_m}{T_m} \approx \frac{\Delta T_m}{T_m} \tag{4.21}$$

On the basis of the above equation, Wang *et al.* (2005) shows that for T_m ranging from 240 K to 300 K, the 1% and 2% accuracies in GPS PWV require errors in T_m less than 2.74 K and 5.48 K on average, respectively. Hence the relative error of GPS PWV approximately equals to that of T_m, which is also shown by Bevis et al. (1994). Finally, Bevis *et al.* (1994) indicate that, in order to obtain T_m rigorously, the vertical profile of temperature and water vapor pressure is needed; plus accurate and simultaneous surface pressure and temperature measurements at the site locations for accurate estimates of GPS PWV.

4.5.1 Surface temperature and pressure for TAMDEF sites

Surface temperature and pressure for some of the TAMDEF sites were generated by using the European Center for Medium-Range Weather Forecasts (ECMWF) and the National Centers for Environmental Prediction–National Center for Atmospheric Research (NCEP–NCAR); for details, we refer to Bromwich and Fogt (2004). Due to the limitations of the reanalysis centers in terms of their coverage of the Antarctic continent, it was possible to estimate surface temperature and pressure only for two of the TAMDEF sites (McMurdo, MCM4, and Cape Roberts, ROB1).

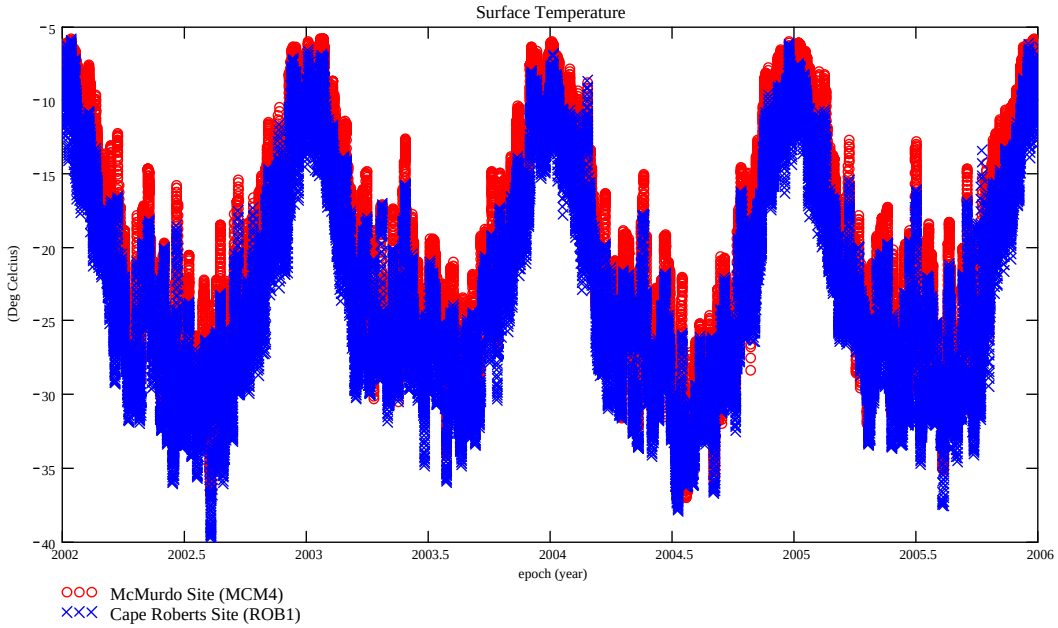

Figure 4.2: Surface temperature for the MCM4 and ROB1 sites.

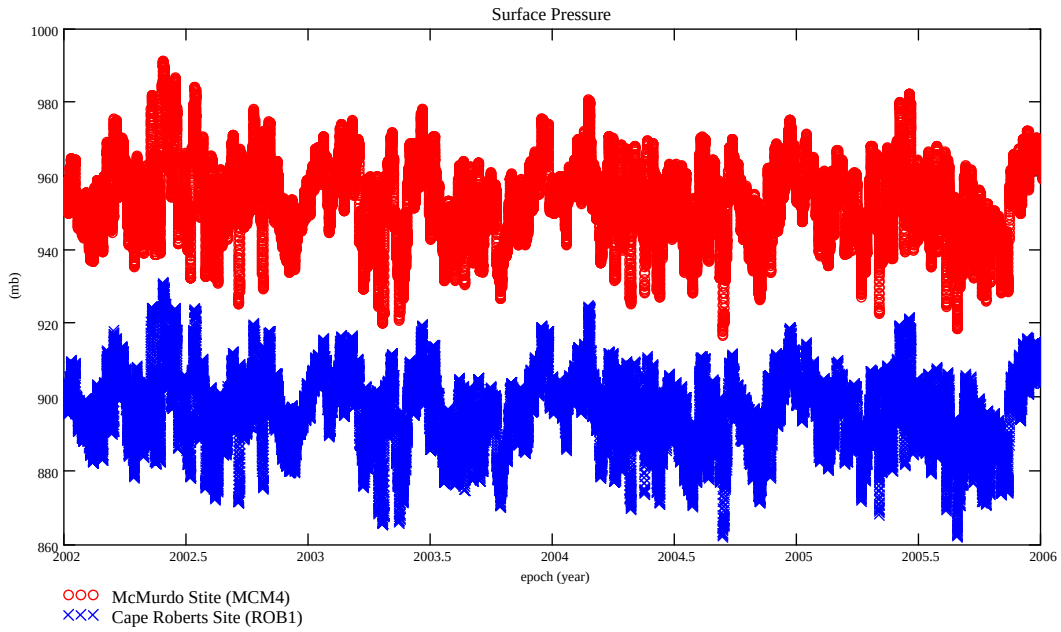

Figure 4.3: Surface pressure for the MCM4 and ROB1 sites.

4.6 Radiosonde measurements

To determine the quality of GPS derived PWV, the estimates for MCM4 are compared to the McMurdo radiosonde measurements of PWV. Radiosondes are weather-balloon-launched instrument packages that measure upper air profiles of temperature, pressure and humidity of the atmosphere. Also wind speed and direction can be measured by monitoring the balloon's progress from ground level to altitudes in excess of 30 km. Radioactivity and ozone measurements can also be obtained using this technique. The observed data are transmitted to the equipment located on the ground in order to be processed into weather messages. The Space Science and Engineering Center (SSEC), University of Wisconsin-Madison (UW-Madison), generated the water vapor radiosonde daily solutions with a 12-hr. interval, for only one of the TAMDEF/IGS sites analyzed in this experiment (http://amrc.ssec.wisc.edu/). Strictly speaking, MCM4 was the only site where both the water vapor radiosonde and the PWV from GPS were compared, due to the fact that radiosonde data for the rest of the TAMDEF stations are not available. The algorithm used to estimate the water vapor from radiosonde data is described in the following.

Regularly, by using radiosonde profiles, it is possible to calculate the total amount of water vapor by integrating the measurements by means of Equation (4.22):

$$PWV_{Radson} = \int \rho_{wv}(z)dz \tag{4.22}$$

where

ρ_{wv} is the water vapor mass density at the altitude z.

The value ρ_{wv} can be obtained from the relative humidity (RH) and the measured temperature (T) as:

$$\rho_{wv} = RH \cdot e_s \cdot \frac{1}{R_{wv} \cdot T} \tag{4.23}$$

where:

e_s is the saturation water vapor pressure (depends on temperature) , and

R_{wv} is the specific gas constant for water vapor ($18 kg / kmole$).

Traditionally, if the water vapor is directly measured by radiosondes, the wet zenith delay can be derived from it, by means of Equation (4.22). The radiosondes are very capable instruments to measure the wet zenith delay with high-quality vertical resolution but poor horizontal resolution, and varying temporal resolution. For the reason that most of the residual tropospheric delays result from the tropospheric wet component, radiosondes provide a good way to measure the residual tropospheric delay. However, these devices are relatively expensive and only limited measurements are available (usually, two launches per day during the summer field season, and one launch a day during the polar winter for MCM4). Figure 4.4 illustrates how the radiosondes are used as sources of vertical profiles of water vapor measurements.

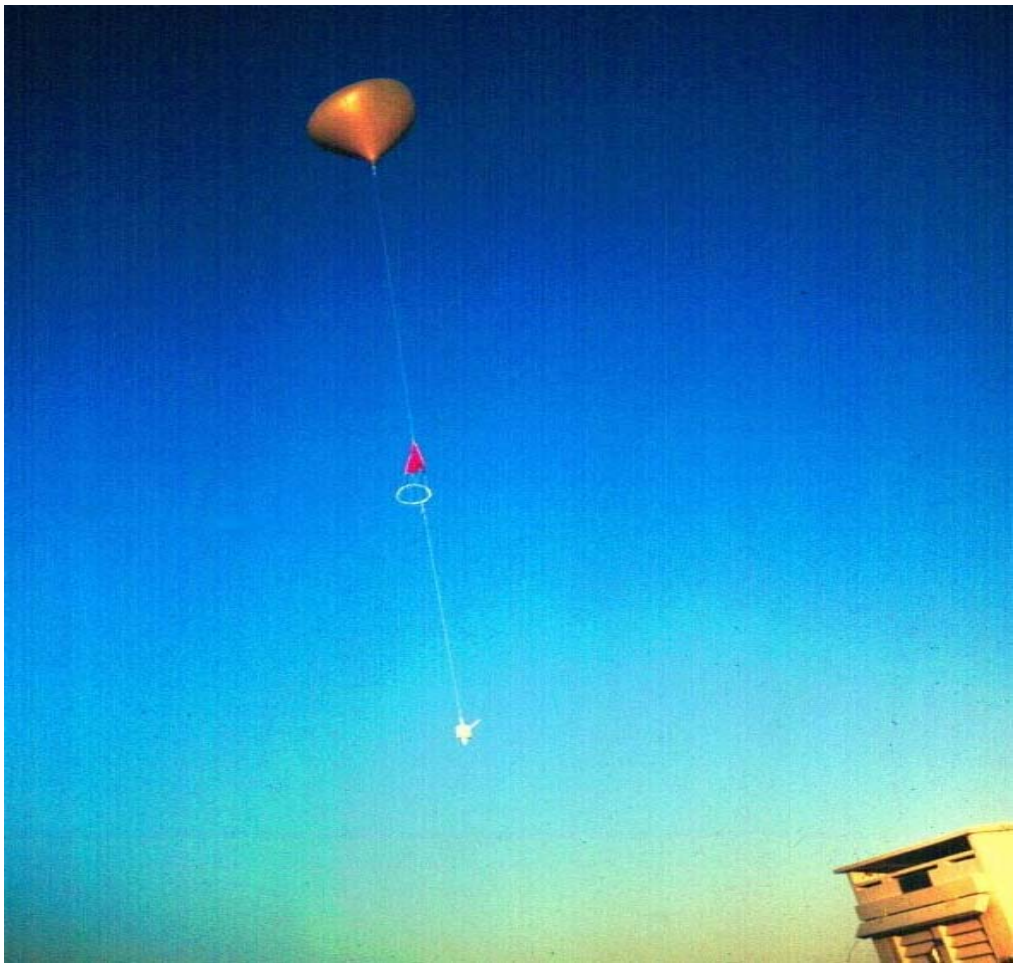

Figure 4.4: Radiosonde for water vapor measurement (courtesy of NOAA).

4.7 Numerical weather prediction

Since the GPS PWV estimates are able to reproduce the variability seen in the radiosonde measurements, the GPS values can thus be compared with extracted PWV values from the Antarctic Mesoscale Prediction System (AMPS). AMPS is a mesoscale numerical weather prediction model that has been tuned to work in the Antarctic environment, and currently provides guidance for operations-based forecasts for the United States Antarctic Program (http://www.mmm.ucar.edu/rt/wrf/amps/). Previous studies have demonstrated that the moisture prediction capability of AMPS is the lowest of the model fields; thus comparing the AMPS forecasts with the GPS PWV estimates will allow for a better understanding of the model's prediction of moist processes. In the future, it is expected that assimilated TAMDEF GPS PWV estimates will aid in improving the moisture prediction in AMPS, thereby leading to increased forecast accuracy, which is essential for any extended research operations conducted across the Antarctic continent. However, observations of the moisture in the atmosphere in and around the McMurdo region are very limited; thus, it is very difficult to quantify the model's performance in this important area. One set of available moisture observations, namely in form of PWV derived from stationary GPS recorders, offers a unique data set that covers a geographically and meteorologically diverse area of the McMurdo region. The use of GPS derived PWV is becoming more common in validating numerical weather forecasts (e.g., Vey *et al.* 2004; Vey and Dietrich, 2008; Liu *et al.* 2005). As such, there is significant potential to substantially extend the understanding of the McMurdo region in this collaborative effort between the United States Antarctic Program's (USAP) atmospheric and geological science initiatives.

PWV is evaluated with AMPS by using the following equation:

$$PWV_{AMPS} = \frac{1}{g}\int_{P\_sfc}^{P\_top} q\,dp \tag{4.24}$$

where:

g is the gravitational constant (~9.81 ms^{-2}),

P_sfc is the atmospheric pressure at the surface of the atmosphere,

P_top is the atmospheric pressure at the top of the atmosphere, and

q is the specific humidity.

The specific humidity is the mass of the dry air (the atmosphere minus water vapor), divided by the total mass of atmosphere (dry + moist air). It is usually expressed in g/kg. AMPS simply calculates the specific humidity, which is related to relative humidity, dew point temperatures, and other moisture indices, and then integrates this throughout the atmospheric column to calculate the PWV. Details in the PWV estimations from AMPS can be found at (http://www.mmm.ucar.edu/rt/wrf/amps/).

CHAPTER 5

NUMERICAL RESULTS AND ANALYSIS

5.1 Introduction

This chapter focuses on the interpretation and analysis of the numerical results of several experiments that investigate particular aspects of GPS geodesy for the continent of Antarctica, specifically for the TAMDEF network. The analysis of the numerical results is based on the appropriate methodology for optimum quality assessment and using data processing schemes as discussed throughout this document. Therefore, the experimental results are expected to provide the key information concerning the position accuracies within the TAMDEF network and to interpret broad, continental-size crustal motion patterns, detected by sparse, regionally distributed, continuous by operating GPS trackers over the Antarctic continent.

5.2 Antenna testing

A complete description of the antenna testing for some selected TAMDEF sites was explained in Section 2.6, and the results from this experiment are described in the following sections.

5.2.1 Hourly results

The hourly solutions for each antenna tested are presented in the Figures 5.1 to 5.3, where the differences in north (n), east (e) and up (u) coordinate components between the *reference antenna* AHT1/1-4 with ASH700936D_M Rev E and the *test antennas* (1) AHT2/1 with ASH701945D_M Rev D, (2) AHT2/2 with TRM29659.00, (3) AHT2/3 with TRM41249.00, and (4) AHT2/4 with NOV702_3.00 Rev 3, respectively, are illustrated. Four 72-hour sessions (0–72 hr, 72–144 hr, 144–216 hr, 216–288 hr) are plotted, each referring to one antenna type tested; note that the primary value of the coordinate component was removed and only the millimeter fraction is considered and plotted here.

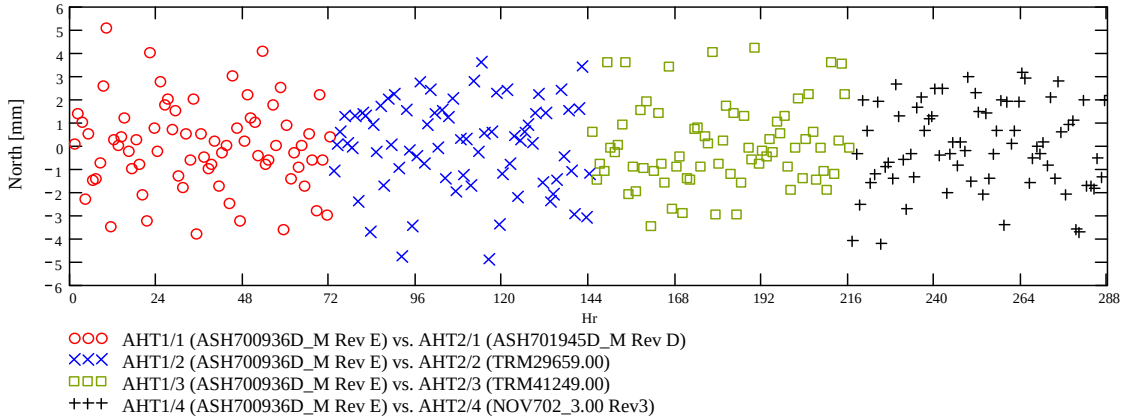

Figure 5.1: North coordinate component: Hourly differences AHT1/1-4 vs. AHT2/1-4.

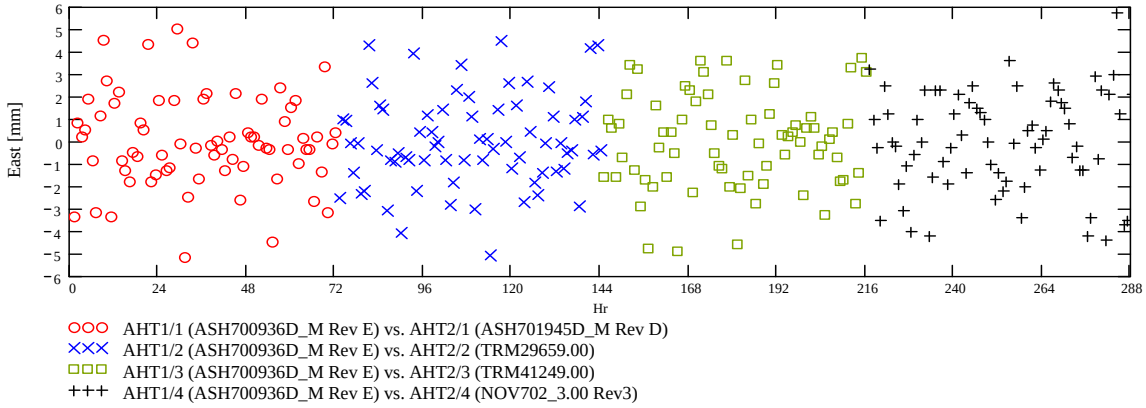

Figure 5.2: East coordinate component: Hourly differences AHT1/1-4 vs. AHT2/1-4.

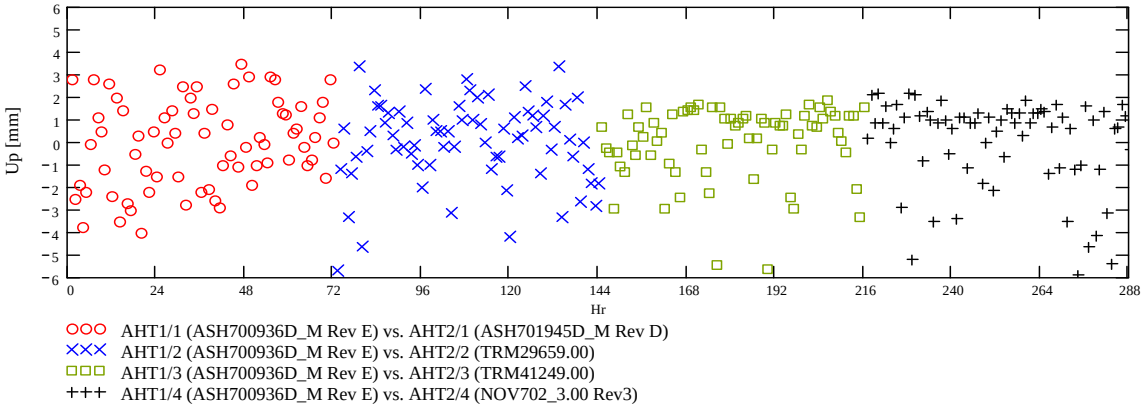

Figure 5.3: Up coordinate component: Hourly differences AHT1/1-4 vs. AHT2/1-4.

It can be observed in Figures 5.1 to 5.3 that the scatter of the n and e coordinate components ranges within –5.2 to +5.7 mm, while the scatter for the u coordinate component ranges within–5.9 to +3.5 mm for all antennas at the AHT2/1-4 site with respect to the antenna at the AHT1/1-4. A reduction of scatter in the u coordinate component by ~1.2 mm and 1.6 mm is observed when comparing ASH700936D_M Rev E against TRM41249.00 and NOV702_3.00 Rev 3, respectively, as compared to the first two antennas (ASH701945D_M Rev D and TRM29659.00). The largest scatter was found in the east coordinate component for all antennas tested, as reflected by the standard deviations shown in the Table 5.1. No significant bias was found in any of the three coordinate components, as reflected by their mean values (0.4 mm or less) listed in the Table 5.1. North, east and up differences at AHT2 between the first antenna, the AHT2/1, against AHT2/2, AHT2/3, and AHT2/4 antennas, respectively, are illustrated in the Figures 5.4, 5.5 and 5.6.

From AHT1/1-4 (ASH700936D_M Rev E)	Coordinate Component	Min (mm)	Max (mm)	Mean (mm)	St. Dev ±(mm)
AHT2/1 (ASH701945D_M Rev D)	**n**	-3.8	5.1	-0.2	1.84
	e	-5.2	5.0	0.4	2.01
	u	-4.0	3.5	-0.3	1.93
AHT2/2 (TRM29659.00)	**n**	-4. 9	3.6	-0.1	1.90
	e	-5.1	4.5	0.1	2.02
	u	-5.7	3.4	0.3	1.83
AHT2/3 (TRM41249.00)	**n**	-3.5	4.2	0.3	1.76
	e	-4.9	3.7	0.4	2.08
	u	-5.7	1.8	-0.1	1.61
AHT2/4 (NOV702_3.00 Rev 3)	**n**	-4.2	3.2	0.3	1.86
	e	-4.4	5.7	-0.3	2.19
	u	-5.9	2.2	0.1	1.97

Table 5.1: North, east and up coordinate components: Hourly statistics AHT1/1-4 vs. AHT2/1-4.

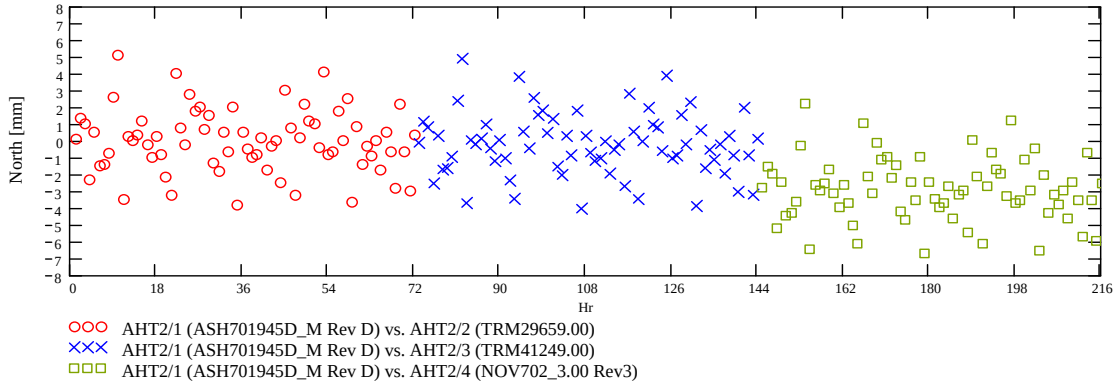

Figure 5.4: North coordinate component: Hourly differences AHT2/1 vs. AHT2/2-4.

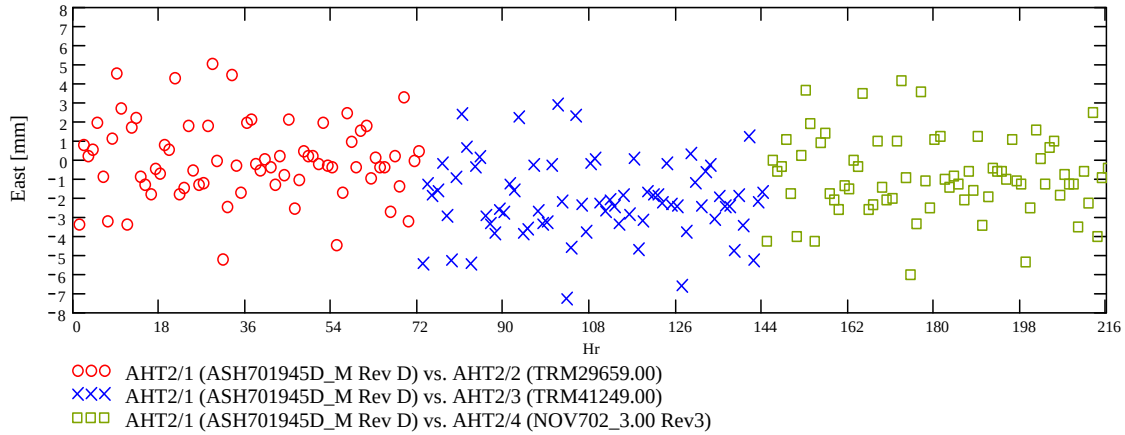

Figure 5.5: East coordinate component: Hourly differences AHT2/1 vs. AHT2/2-4.

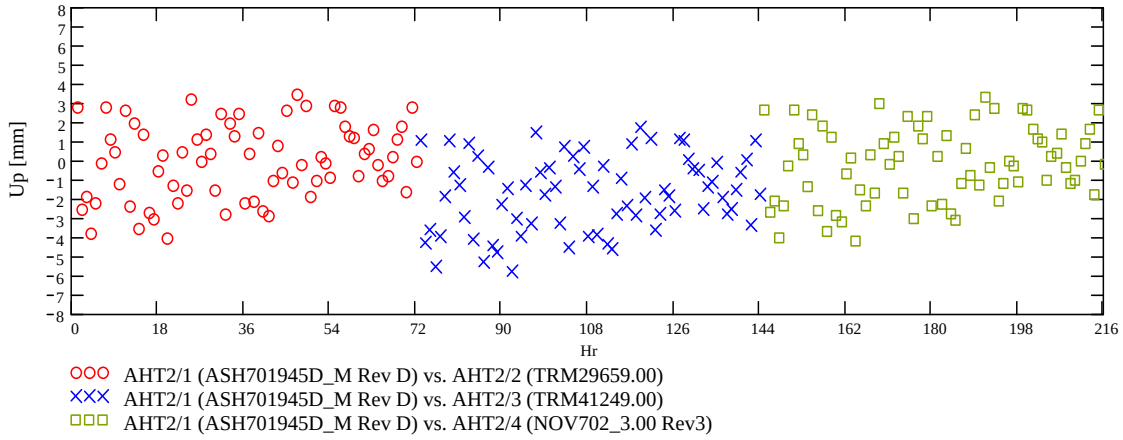

Figure 5.6: Up coordinate component: Hourly differences AHT2/1 vs. AHT2/2-4.

The scatter for the n and e coordinate components ranges within–7.3 to +5.1 mm as can be observed in Figures 5.4 to 5.6, while the scatter for the u coordinate component ranges within–5.8 to +3.5 mm for all the hourly differences (AHT2/1 vs. AHT2/2-4). A jump of ~ –2.5 mm in the n coordinate component, when comparing ASH701945D_M Rev D against NOV702_3.00 Rev 3, can be observed in Figure 5.4; this can also be observed by comparing the mean values shown in Table 5.2. The biggest variation in the u coordinate component (–1.7 mm) was found when comparing ASH701945D_M Rev D against TRM41249.00 (see Figure 5.6), also reflected by its mean value shown in Table 5.2. The smallest variation in the vertical coordinate component was found when comparing ASH701945D_M Rev D against the TRM29659.00, and NOV702_3.00 Rev 3 antennas, 0.1 mm in both cases (see Table 5.2).

From AHT2/1 (Ashtech Choke ring D&M)	Coordinate Component	Min (mm)	Max (mm)	Mean (mm)	St. Dev ±(mm)
AHT2/2 (Trimble Choke ring)	**n**	-3.8	5.1	0.1	1.8
	e	-5.2	5.0	0.5	2.0
	u	-4.0	3.5	-0.1	1.9
AHT2/3 (Trimble Zephyr)	**n**	-4.1	4.9	-0.2	1.3
	e	-7.3	2.9	-2.2	2.5
	u	-5.8	1.7	-1.7	2.2
AHT2/4 (NovAtelGPS-702 Rev 3)	**n**	-6.7	2.2	-2.5	2.3
	e	-6.1	4.1	-0.5	1.3
	u	-4.2	3.3	0.1	1.1

Table 5.2: North, east and up coordinate components: Hourly differences AHT2/1 vs. AHT2/2, AHT2/3 and AHT2/4.

5.2.2 Daily and sub-daily results

The Figures 5.7, 5.8 and 5.9 show the daily and sub-daily differences between AHT1/1-4 and AHT2/1-4. The results seem very stable and indicate a scatter of only –0.3 to +0.3 mm in the n coordinate component for the first three antennas, and –0.7 to +0.5 mm for NOV702_3.00 Rev 3. The smallest scatter was found in the e coordinate component; it ranges within –0.2 to +0.2 mm for all the antennas (see Figure 5.8). The scatter in the u coordinate component looks also very stable, and ranges within –0.5 to +0.6 mm as can be seen in Table 5.3.

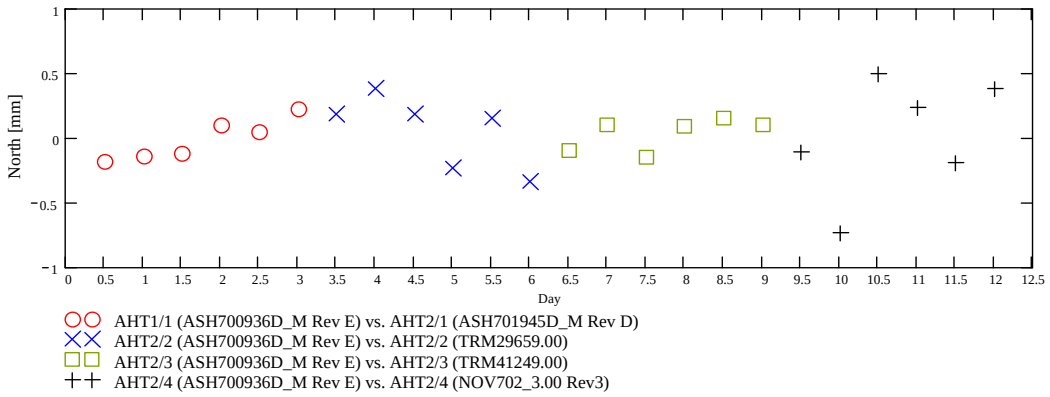

Figure 5.7: North coordinate component: Sub-daily and daily differences AHT1/1-4 vs. AHT2/1-4.

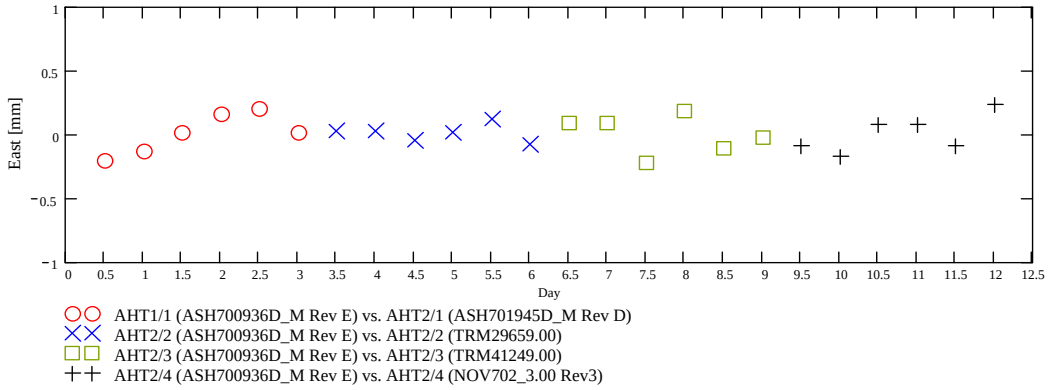

Figure 5.8: East coordinate component: Sub-daily and daily differences AHT1/1-4 vs. AHT2/1-4.

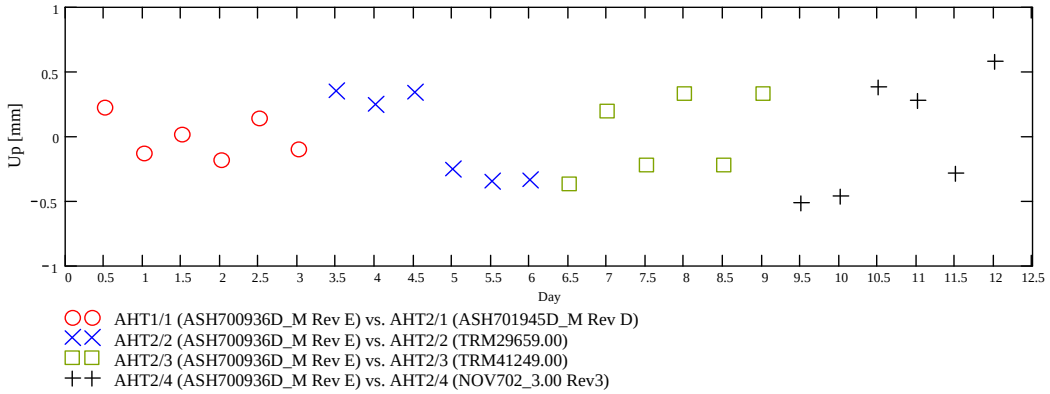

Figure 5.9: Up coordinate component: Sub-daily and daily differences AHT1/1-4 vs. AHT2/1-4.

From AHT1/1-4 (ASH700936D_M Rev E)	Coordinate Component	Min (mm)	Max (mm)	Mean (mm)	St. Dev. ±(mm)
AHT2/1 (ASH701945D_M Rev D)	**n**	-0.2	0.2	-0.022	0.1
	e	-0.2	0.2	0.012	0.1
	u	-0.2	0.2	-0.005	0.2
AHT2/2 (TRM29659.00)	**n**	-0.3	0.3	0.025	0.2
	e	-0.1	0.1	0.008	0.1
	u	-0.4	0.4	-0.001	0.3
AHT2/3 (TRM41249.00)	**n**	-0.2	0.2	0.002	0.1
	e	-0.2	0.2	0.000	0.1
	u	-0.4	0.3	0.003	0.2
AHT2/4 (NOV702_3.00 Rev 3)	**n**	-0.7	0.5	0.002	0.3
	e	-0.2	0.2	0.003	0.1
	u	-0.5	0.6	-0.002	0.3

Table 5.3: North, east and up coordinate components: Daily and sub-daily differences AHT1/1-4 vs. AHT2/1-4.

Table 5.3 gives the statistics for the n, e and u coordinate components of the daily differences (AHT1/1-4 vs. AHT2/1-4). As can be observed in Table 5.3, the standard deviation is very small (±0.1 to ±0.3 mm), and the mean indicates no significant bias in any of the three coordinate components (0.02 mm or less). In general, the results from the antennae testing indicate no significant variations in the vertical site coordinate due to the antenna change, when standard antenna calibration models from NGS (refer to Section 2.6) were used. In most cases, bigger variations in north (n), east (e) and up (u) coordinate components, as a result of the antenna change, appear in the hourly results, as compared to the sub-daily and daily solutions. The magnitude of daily and sub-daily variations is negligible for all antennas tested.

Since daily coordinate variations are routinely used for TAMDEF sites, it can be concluded that as long as proper antenna calibration parameters are used, no significant effects of the antenna replacement can be found. Therefore, any of the antennae type used in the experiment should guarantee the positioning results that are comparable to these currently obtained for TAMDEF GPS network under similar conditions with the choke ring D&M antenna. In practice, the behavior of the daily results indicates what could be expected in the TAMDEF network, since daily solutions are usually generated for the regular tracking sites. Thus, all four antennas tested here perform consistently, and no significant effect of the antenna replacement on the daily coordinate solutions for the test site is observed if proper antenna calibration parameters are used.

5.2.3 Multipath assessment at the *reference* and *test* sites

The UNAVCO TEQC software (see Section 2.7) was used to generate the hourly and daily pseudorange RMS (root mean squared) multipath (MP) variations at the *reference* (AHT1) and *test* (AHT2) sites, respectively. The TEQC software forms linear combinations of pseudorange and carrier phase observations to compute the L1/L2 pseudorange multipath for C/A- or P-code observations. Strictly speaking, for this experiment the hourly and daily MP1-RMS on L1 frequency were computed and analyzed.

Table 5.4 shows the statistics of cycle slips (CSs) due to ionospheric delay (IOD) and the level of pseudorange multipath on L1. In TEQC it is assumed that the maximum ionospheric rate that does not cause CS is 400 cm/min; if the IOD is greater than 400 cm/min, a cycle slip is assumed. Usually, the expected RMS is ±50 cm for MP1. If the MP1-RMS is less than expected, four times the sigma value is used as a threshold, in order to obtain the amount, by which the multipath must change to be considered as a cycle slip. It can be observed in Table 5.4 that the sites/sessions most affected by the presence of IOD or MP slips are AHT1/1 (ASH700936D_M Rev E) and AHT2/1 (ASH701945D_M Rev D) for Nov. 19-20; AHT1/2 (ASH700936D_M Rev E) and AHT2/2 (TRM29659.00) for Nov. 21-22; AHT1/4 (ASH700936D_M Rev E) and AHT2/4 (NOV702_3.00 Rev 3) for Nov. 30 – Dec. 1.

Site/ Session	Antenna Type	IOD or MP Slips	Start-End Date And Local UTC	IOD or MP Slips	Antenna Type	Site/ Session
AHT1/1	ASH700936D_M Rev E	24	19:43:10 (Nov. 17) 19:46:55 19:43:05 (Nov. 18) 19:46:50	17	ASH701945D_M Rev D	AHT2/1
		27	19:43:10 (Nov. 18) 19:46:55 19:43:05 (Nov. 19) 19:46:50	17		
		127	19:43:10 (Nov. 19) 19:46:55 19:43:05 (Nov. 20) 19:39:00	84		
AHT1/2	ASH700936D_M Rev E	51	19:45:35 (Nov. 20) 19:43:45 19:45:30 (Nov. 21) 19:43:40	23	TRM29659.00	AHT2/2
		157	19:45:35 (Nov. 21) 19:43:45 19:45:30 (Nov. 22) 19:43:40	113		
		44	19:45:35 (Nov. 22) 19:43:45 19:45:30 (Nov. 23) 19:43:40	21		
AHT1/3	ASH700936D_M Rev E	36	19:43:10 (Nov. 24) 19:43:45 19:43:05 (Nov. 25) 19:43:40	25	TRM41249.00	AHT2/3
		41	19:43:10 (Nov. 25) 19:43:45 19:43:05 (Nov. 26) 19:43:40	24		
		43	19:43:10 (Nov. 27) 19:43:45 19:43:05 (Nov. 28) 19:43:40	25		
AHT1/4	ASH700936D_M Rev E	30	19:43:45 (Nov. 28) 19:49:35 19:43:40 (Nov. 29) 19:49:30	18	NOV702_3.00 Rev 3	AHT2/4
		15	19:43:45 (Nov. 29) 19:49:35 19:43:40 (Nov. 30) 19:49:30	13		
		85	19:43:45 (Nov. 30) 19:49:35 19:43:40 (Dec. 01) 19:49:30	73		

Table 5.4: GPS signal tracking characteristics: Cycle slip analysis.

Figure 5.10 shows the hourly MP1-RMS at the *test site* AHT2. The smallest scatter of the MP1-RMS (~25 cm) is observed when using AHT2/2 and AHT2/3 antennas, while the scatter of the MP1-RMS values for AHT 2/1 and AHT 2/4 reaches more than 60 cm. The Figures 5.11 and 5.12 illustrate the daily MP1-RMS at both *reference site* (AHT2/1-4) and *test site* (AHT1/1-4), respectively. The MP1-RMS values for AHT1/1-4 look very comparable, with differences within 1-3 cm from day-to-day, and 1-2 cm for the same antenna type, except for day of week 333, where the NOV702_3.00 Rev 3 antenna was used (up to 6 cm difference within day-to-day comparison). The MP1-RMS values for AHT2/1-4 vary more significantly, as compared to the *reference site*; 1-13 cm variations from day-to-day, and 1 cm within the same antenna type, except for doy 333 where the NOV702_3.00 Rev 3 antenna was used (again, up to 6 cm difference within day-to-day comparison).

The Figures 5.13 and 5.14 illustrate the daily pseudo-range multipath variation MP1-RMS as a function of the average elevation (per satellite per day) at *reference site* (AHT1/1-4) at the *test site* (AHT2/1-4), respectively. The average elevation is computed by averaging the daily elevation values for each satellite. It can clearly be observed that the MP1-RMS for average elevation within 30-35 degrees reaches values up to 65 cm at the *reference* and *test sites*, respectively.

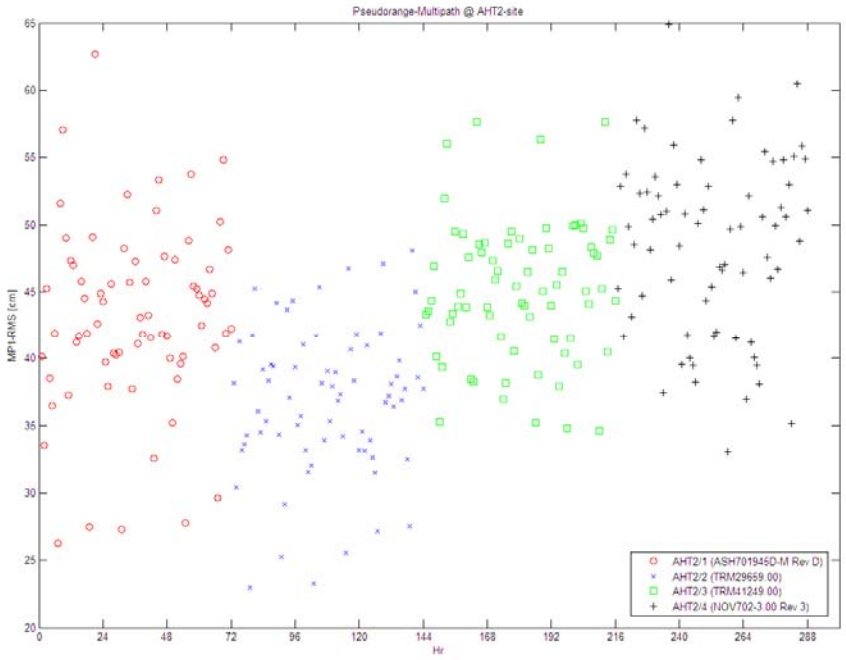

Figure 5.10: Hourly MP1-RMS at *test site* (AHT2/1-4).

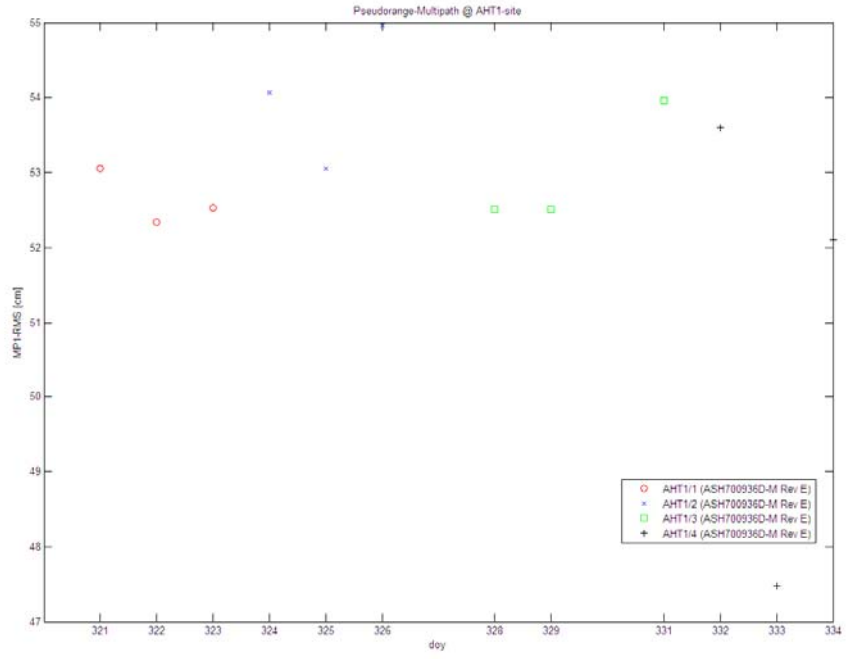

Figure 5.11: Daily MP1-RMS at *reference site* (AHT1/1-4).

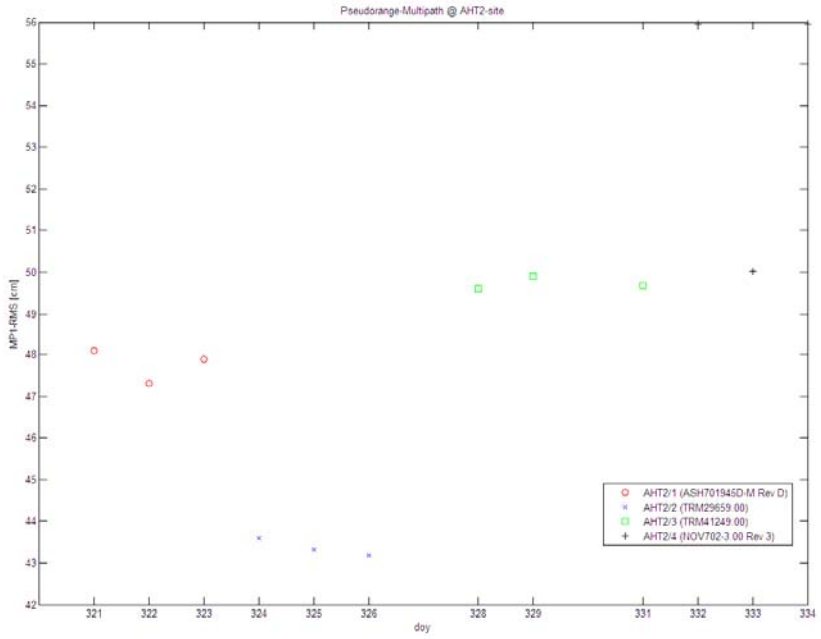

Figure 5.12: Daily MP1-RMS at *test site* (AHT2/1-4).

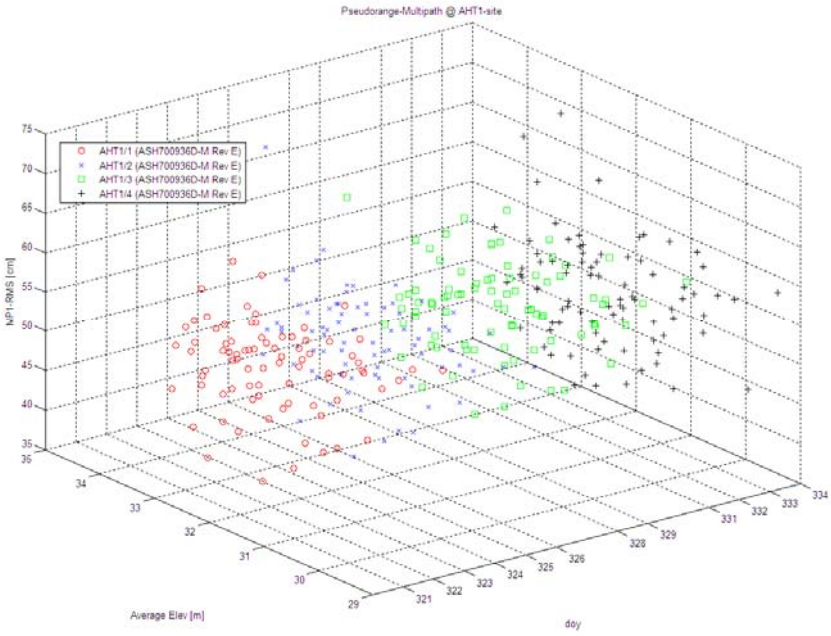

Figure 5.13: Pseudorange multipath (MP1-RMS) as a function of day of year (doy) and average elevation at *reference site* (AHT1/1-4).

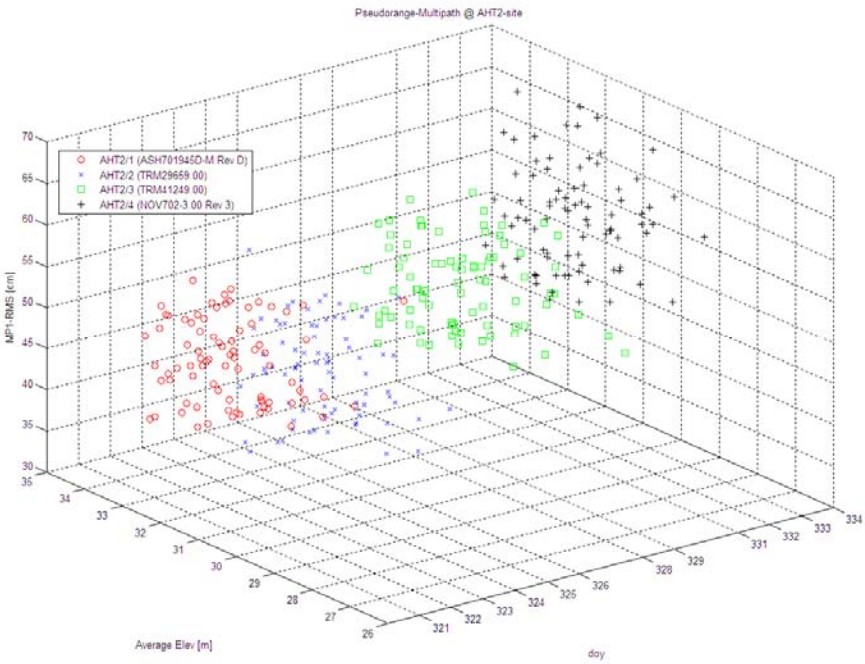

Figure 5.14: Pseudorange multipath (MP1-RMS) as a function of day of the year (doy) and average elevation at *test site* (AHT2/1-4).

5.3 Pseudorange multipath assessment at selected TAMDEF sites

It is always important to have a feasible estimation of multipath; this means that more than just a simple comparison between the measured pseudoranges or carrier phases and the true geometric range has to be done, since the measurement error is a combination of many effects in addition to multipath. Therefore, daily pseudo-range RMS (root mean squared) multipath (MP) on the L1 and L2 carriers was estimated for each of the TAMDEF sites. The objective of this experimentation was to investigate how the TAMDEF sites are affected by the influence of possible local multipath. In order to proceed with this experiment, this research followed the approach as shown by Estey and Meertens (1999); Hilla and Cline (2002), and the UNAVCO TEQC software (see Chapter 2) was used for this purpose.

5.3.1 MP1-RMS and MP2-RMS results

The Figures 5.15 and 5.16 show the pseudo-range multipath results (MP1-RMS and MP2-RMS) at the selected TAMDEF sites (FTP1, MCM4 and ROB1), which are the sites with the longest data span. As can be seen in these figures, MCM4 is the site with almost 10-years of continuous data (1996-2006). A jump on both the MP1-RMS and MP2-RMS results can be observed at the MCM4 site at the beginning of year 2002. This fact could be attributed to the hardware change when the AOA SNR-12 ACT replaced the

ROGUE SNR-8000 GPS receiver on January 3, 2002. It is very important to point out that there was no antenna replacement since the installation of the MCM4 site. The MP1-RMS and MP2-RMS results for MCM4 (2002-2006) behave the same way (i.e., annual variations) getting the highest values (1.76 m on MP1 and 3.38 m on MP2) in the middle of every year. Prior to 2002, the results look much more comparable among them at MCM4.

The MP1-RMS and MP2-RMS results for the FTP1 and ROB1 sites seem to experience less variations (0.85 m on MP1 and 1.16 m on MP2 for FTP1, 0.97 m on MP1 and 1.24 m on MP2 for ROB1), as compared to MCM4. However, the ROB1 site experienced a shift between the years 2005 and 2006, as shown in both Figures 5.15 and 5.16. Overall, FTP1, MCM4 and ROB1 were the sites with higher levels of pseudorange multipath (MP1-RMS), ranking first, second and fourth in Table 5.5. The Tables 5.5 and 5.6 summarize the MP1-RMS and MP2-RMS results for all TAMDEF sites. Here, the order (rank) of the most and least affected sites is shown, including the number of available days for each tested site. Statistics, such as the maximum, minimum, standard deviation, and mean, as well as characteristics of the hardware used (i.e., receiver and antenna type) are also shown on these tables.

It may be concluded from the multipath analysis, in accordance with the proposed objective, that the obtained MP1-RMS and MP2-RMS results should be considered in further research to improve the positional results. In addition, MCM4 was found to be the site with highest multipath (between 1 to 4 m in MP1 and MP2, respectively), and this is not good at all, since MCM4 is the primary ITRF access point for this part of Antarctica. The reason for high multipath (with seasonal effect) at MCM4 might be due to the receiver itself, the location environment and the existence of antenna radome. Note that same seasonal moisture condensation can be observed inside the radome (see Figure 2.8). Figures 5.15 and 5.16 show the level of MP1-RMS and MP2-RMS at each station individually, based on the daily variation.

Figures showing the MP1-RMS and MP2-RMS results for all TAMDEF sites are presented in APPENDIX C.

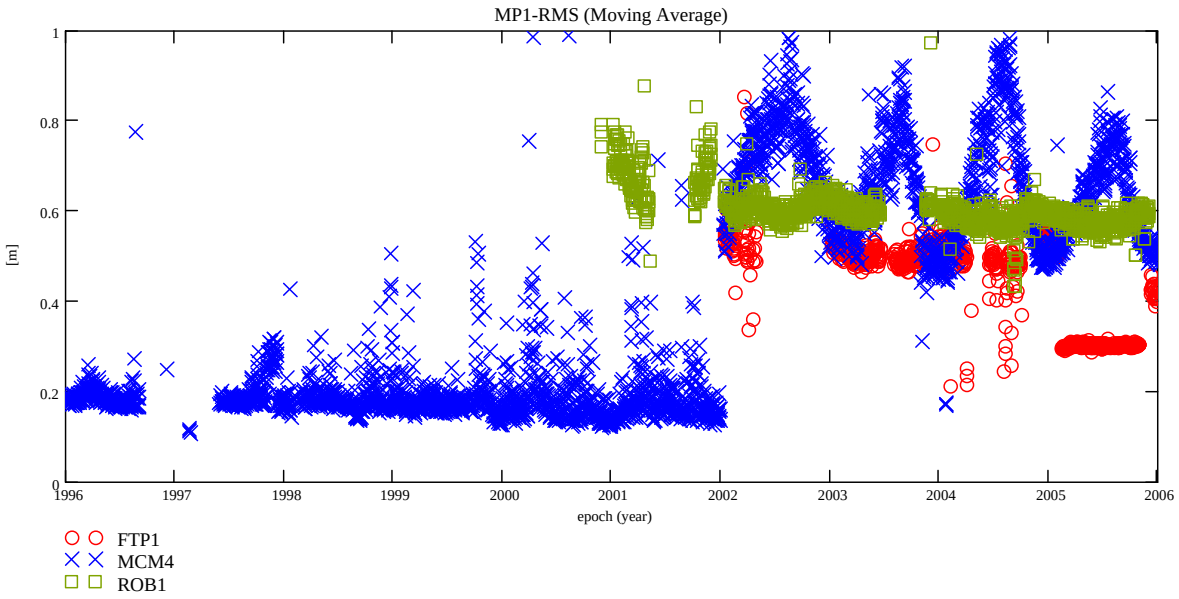

Figure 5.15: MP1-RMS for the FTP1, MCM4 and ROB1 sites.

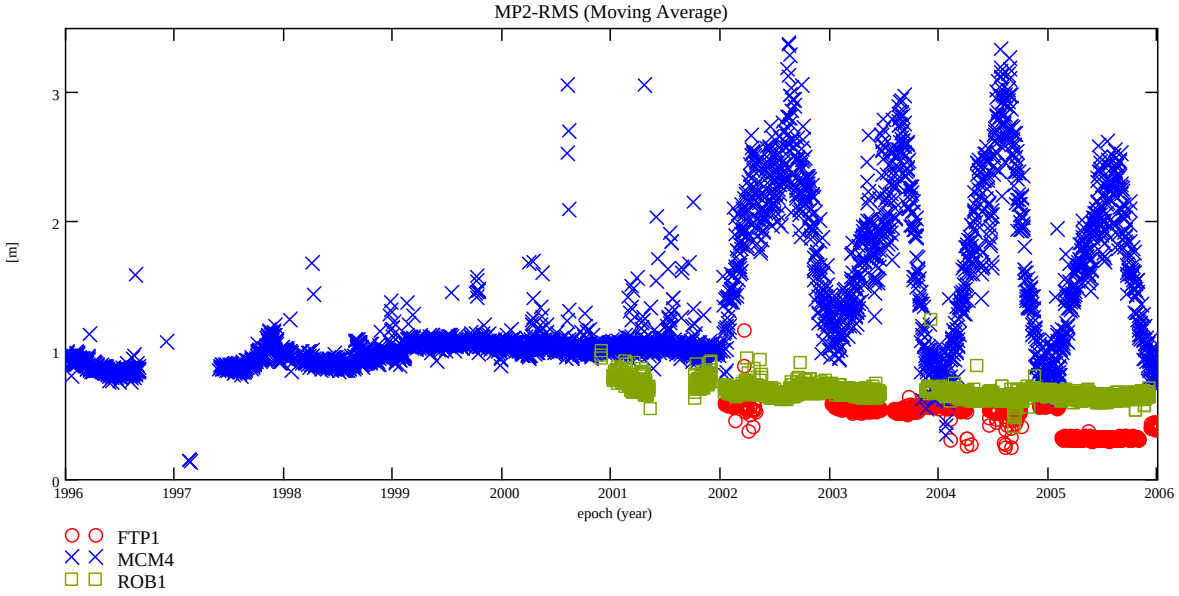

Figure 5.16: MP2-RMS for the FTP1, MCM4 and ROB1 sites.

Rank	Site	No. of Days	Max (m)	Min (m)	St. Dev. ±(m)	Mean (m)	Receiver Type	Antenna Type
1	**MCM4**	3293	1.76	0.11	0.25	0.40	AOA SNR-12 ACT	AOAD/M_T
2	**ROB1**	1416	0.97	0.43	0.04	0.60	TPS HE_GD	ASH700936E
3	**WTE0**	69	0.89	0.01	0.21	0.54	ASHTECH Z-XII3	TRM29659.00
4	**FTP1**	882	0.85	0.21	0.10	0.45	TPS HE_GD	ASH700936D_ M SCIS
5	**FIE0**	266	0.83	0.24	0.05	0.43	TPS HE_GGD	ASH701945B_ M SCIS
6	**KER0**	81	0.75	0.22	0.09	0.36	DL4-NovAtel	ASH700936E
7	**BRM0**	30	0.73	0.23	0.09	0.45	TRIMBLE_5700	ASH701945E_M
8	**LWN0**	317	0.64	0.24	0.04	0.51	TPS HE_GGD	ASH701945B_ M SCIS
9	**ROY0**	69	0.59	0.08	0.12	0.22	TRIMBLE 4000SSI	TRM29659.00
10	**BRO0**	80	0.57	0.24	0.05	0.33	DL4-NovAtel	ASH700936E
11	**WAL0**	74	0.55	0.02	0.14	0.20	TRIMBLE 4000SSE	TRM 29659.00
12	**BRA0**	42	0.52	0.33	0.06	0.47	TRIMBLE 4000SSI	ASH700936E
13	**ROS0**	33	0.51	0.26	0.05	0.34	DL4-NovAtel	ASH701945D_ M
14	**MAS0**	30	0.51	0.37	0.04	0.42	TRIMBLE 4000SSE	TRM29659.00
15	**BIR0**	31	0.51	0.08	0.16	0.29	TRIMBLE 4000SSI	ASH700936E
16	**CRZ0**	19	0.50	0.19	0.09	0.43	TRIMBLE 5700	ASH701945C_ M
17	**CON0**	49	0.49	0.22	0.05	0.28	DL4-NovAtel	ASH700936E
18	**WHN0**	447	0.48	0.21	0.03	0.39	TPS HE_GGD	ASH701945B_ M SCIS
19	**ALN0**	58	0.47	0.19	0.07	0.31	ASHTECH Z-12	ASH700936E
20	**FLM2**	166	0.47	0.20	0.06	0.39	TPS HE_GD	ASH700936E
21	**BUR0**	60	0.46	0.24	0.04	0.31	DL4-NovAtel	ASH700936E
22	**BFT0**	38	0.45	0.23	0.09	0.36	TPS LEGACY	ASH701945E_M
23	**WRN0**	124	0.43	0.17	0.05	0.27	DL4-NovAtel	ASH700936E
24	**ANT0**	46	0.40	0.20	0.05	0.29	TRIMBLE 4000SSE	ASH700936E
25	**MBF0**	74	0.38	0.18	0.06	0.27	TRIMBLE 5700	ASH701945E_M
26	**BTL0**	29	0.38	0.17	0.05	0.30	ASHTECH Z-12	TRM41249.00
27	**ESH0**	40	0.37	0.17	0.04	0.24	DL4-NovAtel	NOV702_2.02
28	**RYN0**	44	0.36	0.27	0.02	0.32	TRIMBLE 5700	ASH701945E_M
29	**DWT0**	21	0.36	0.21	0.04	0.29	ASHTECH Z-12	ASH700936E
30	**VAN0**	10	0.35	0.32	0.01	0.33	TRIMBLE 4000SSI	TRM22020.00+ GP
31	**FRK0**	29	0.35	0.20	0.06	0.39	ASHTECH Z-12	ASH700936E
32	**FLM0**	18	0.31	0.27	0.01	0.29	TPS HE_GD	ASH700936E
33	**CRN0**	16	0.30	0.27	0.01	0.29	TRIMBLE 4000SSE	ASH700936E

Table 5.5: Statistics of the MP1-RMS for TAMDEF sites.

Rank	Site	No. of Days	Max (m)	Min (m)	St. Dev. ±(m)	Mean (m)	Receiver Type	Antenna Type
1	**MCM4**	3293	3.38	0.13	0.56	1.33	AOA SNR-12 ACT	AOAD/M_T
2	**ROS0**	33	1.59	0.37	0.41	1.10	DL4-NovAtel	ASH701945D_M
3	**BTL0**	29	1.54	0.26	0.45	0.78	ASHTECH Z-12	TRM41249.00
4	**WAL0**	74	1.53	0.04	0.36	0.36	TRIMBLE 4000SSE	TRM 29659.00
5	**RYN0**	44	1.53	0.88	0.15	1.31	TRIMBLE 5700	ASH701945E_M
6	**BIR0**	31	1.52	0.12	0.51	0.66	TRIMBLE 4000SSI	ASH700936E
7	**ESH0**	40	1.50	0.24	0.46	0.75	DL4-NovAtel	NOV702_2.02
8	**WTE0**	69	1.46	0.01	0.30	0.86	ASHTECH Z-XII3	TRM29659.00
9	**CRZ0**	19	1.46	0.38	0.29	1.12	TRIMBLE 5700	ASH701945C_M
10	**MBF0**	74	1.45	0.27	0.43	0.70	TRIMBLE 5700	ASH701945E_M
11	**BRA0**	42	1.45	0.43	0.32	0.76	TRIMBLE 4000SSI	ASH700936E
12	**ANT0**	46	1.45	0.40	0.28	0.97	TRIMBLE 4000SSE	ASH700936E
13	**DWT0**	21	1.44	0.44	0.34	1.05	ASHTECH Z-12	ASH700936E
14	**MAS0**	30	1.43	0.84	0.24	1.17	TRIMBLE 4000SSE	TRM29659.00
15	**FRK0**	29	1.41	0.33	0.39	0.82	ASHTECH Z-12	ASH700936E
16	**CRN0**	16	1.40	1.15	0.07	1.30	TRIMBLE 4000SSE	ASH700936E
17	**ALN0**	58	1.39	0.30	0.40	0.69	ASHTECH Z-12	ASH700936E
18	**WRN0**	124	1.39	0.35	0.33	0.70	DL4-NovAtel	ASH700936E
19	**BRM0**	30	1.38	0.51	0.24	1.16	TRIMBLE_5700	ASH701945E_M
20	**FLM0**	18	1.36	0.38	0.24	1.07	TPS HE_GD	ASH700936E
21	**FIE0**	266	1.32	0.25	0.08	0.52	TPS HE_GGD	ASH701945B_M SCIS
22	**FLM2**	166	1.25	0.27	0.16	0.47	TPS HE_GD	ASH700936E
23	**ROB1**	1416	1.24	0.41	0.06	0.68	TPS HE_GD	ASH700936E
24	**BFT0**	38	1.21	0.49	0.25	0.71	TPS LEGACY	ASH701945E_M
25	**FTP1**	882	1.16	0.25	0.12	0.48	TPS HE_GD	ASH700936D_M SCIS
26	**ROY0**	69	1.14	0.15	0.24	0.35	TRIMBLE 4000SSI	TRM29659.00
27	**KER0**	81	0.98	0.54	0.10	0.71	DL4-NovAtel	ASH700936E
28	**LWN0**	317	0.71	0.28	0.05	0.60	TPS HE_GGD	ASH701945B_M SCIS
29	**BUR0**	60	0.69	0.55	0.03	0.61	DL4-NovAtel	ASH700936E
30	**BRO0**	80	0.69	0.33	0.06	0.45	DL4-NovAtel	ASH700936E
31	**WHN0**	447	0.60	0.28	0.03	0.45	TPS HE_GGD	ASH701945B_M SCIS
32	**VAN0**	10	0.58	0.44	0.04	0.53	TRIMBLE 4000SSI	TRM22020.00+GP
33	**CON0**	49	0.56	0.30	0.05	0.38	DL4-NovAtel	ASH700936E

Table 5.6: Statistics of the MP2-RMS for TAMDEF sites.

5.4 Effect of ocean tide loading on the vertical coordinate component

The results from the ocean tide modeling and its possible effect on the vertical (up) coordinate component of TAMDEF positioning results are shown in this section. The analysis is presented for TPXO6.2 and CATS02.01, which are the recently validated models for the Antarctica (refer to Section 2.8) and have been used in this experiment. These two models have been minimally tested using independent data at the selected TAMDEF sites (FTP1, MCM4 and ROB1) so far. It is expected that the results obtained in this experiment could help validating the OTM for Antarctic GPS, which would ensure that GPS measurements in and across the region to succeed in measuring crustal motion.

5.4.1 OTM-TPXO6.2 vs. OTM-CATS02.01 results

The Figures 5.17, 5.18 and 5.19 illustrate the adjusted vertical coordinate component obtained with PAGES software after applying the tested models (CATS02.01 and TPXO6.2) for the years 2002-2005 specifically for three of the TAMDEF sites (FTP1, MCM4 and ROB1). The results indicate a difference among the models differ at the decimeter level, with smaller mean values when using the CATS02.01 model for the three sites. In terms of standard the deviation, the results compare very well with millimeter differences among the two models: 0.3 mm for FTP1 and 0.9 mm MCM4, in contrast to 4.6 mm difference for ROB1 (see Table 5.7).

It can be concluded from the OTM analysis that the vertical coordinate component for the three TAMDEF sites is more stable when using the CATS02.01 model in comparison with the TPXO6.2; this might be attributed to the fact that CATS02.01 model best assimilates the topography of the Antarctic region.

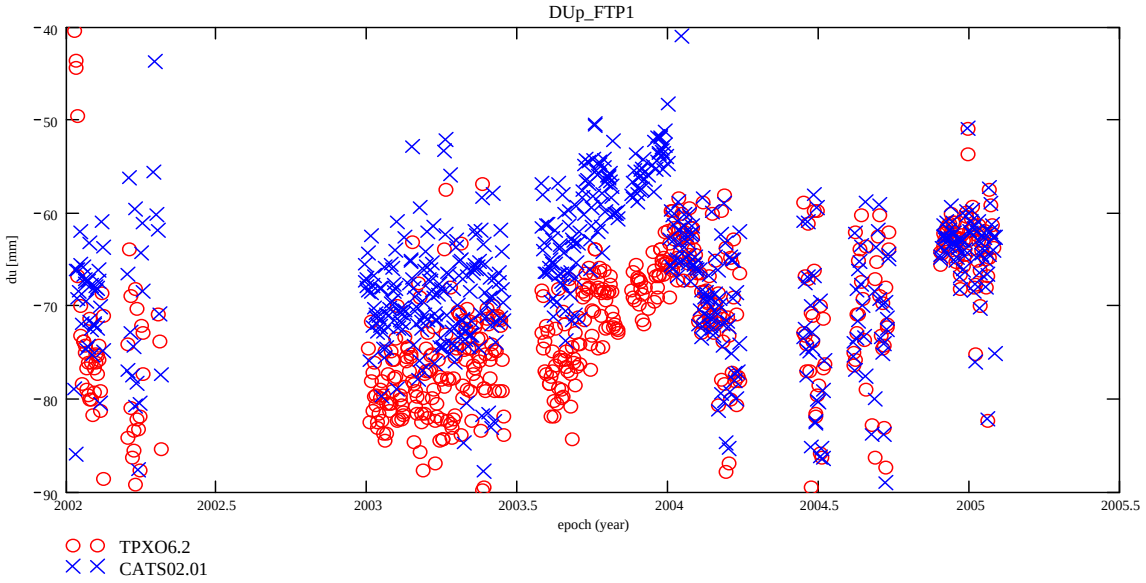

Figure 5.17: Effect on the up coordinate component for the FTP1 site using TPXO6.2 vs. CATS02.01.

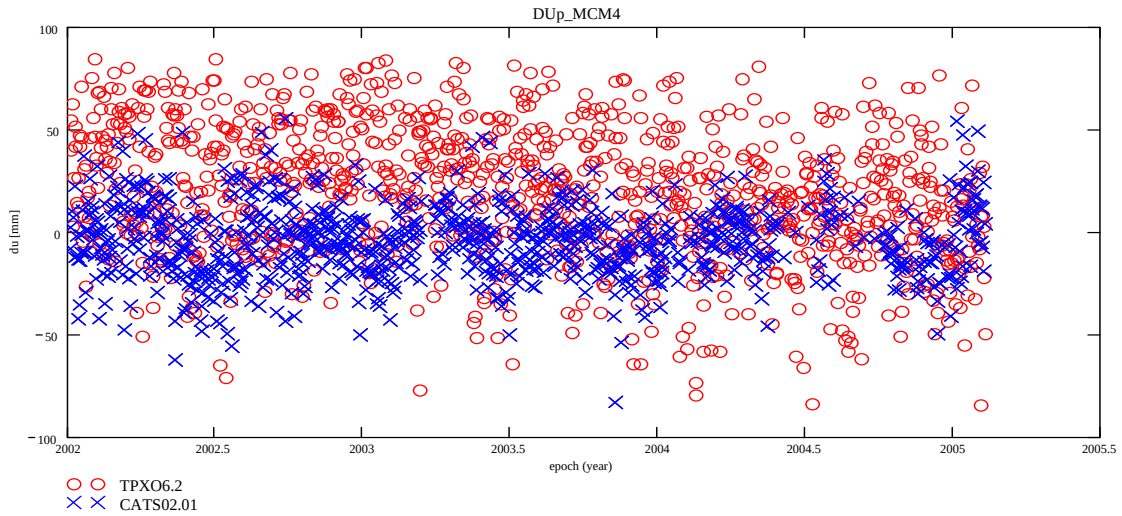

Figure 5.18: Effect on the up coordinate component for the MCM4 site using TPXO6.2 vs. CATS02.01.

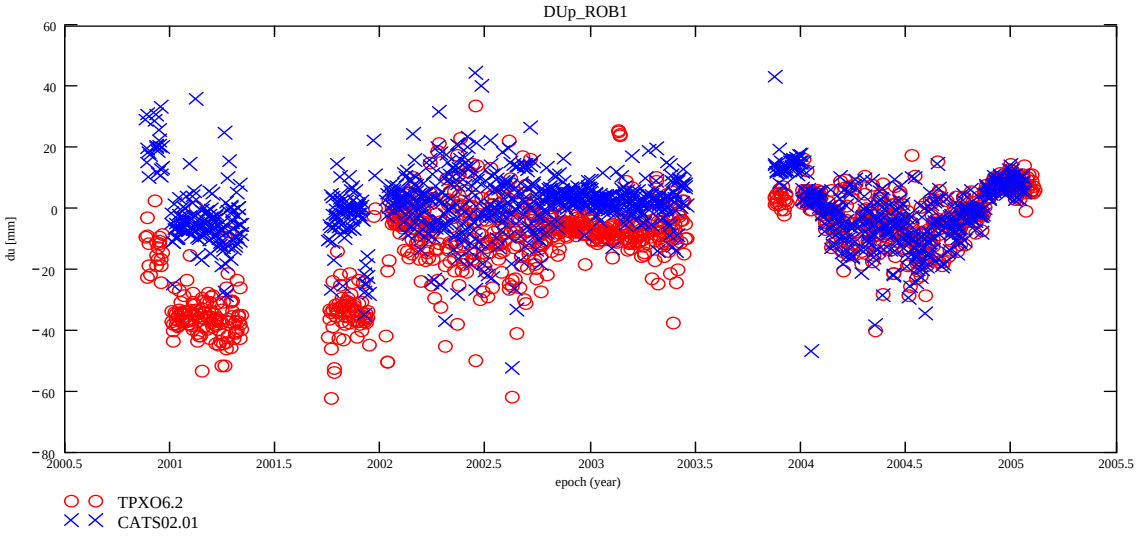

Figure 5.19: Effect on the up coordinate component for the ROB1 site using TPXO6.2 vs. CATS02.01.

Site	OTM	Max (mm)	Min (mm)	Mean (mm)	St. Dev. ± (mm)
FTP1	TPXO6.2	-40.4	-89.9	-72.2	7.7
	CATS02.01	-41.0	-89.0	-66.6	7.4
MCM4	TPXO6.2	84.4	-84.4	-19.2	17.8
	CATS02.01	55.4	-83.1	-4.3	16.9
ROB1	TPXO6.2	33.6	-62.2	-10.0	14.9
	CATS02.01	44.4	-52.3	0.1	10.3

Table 5.7: Effect on the up coordinate component for the FTP1, MCM4 and ROB1 sites, using TPXO6.2 vs. CATS02.01.

5.5 Network adjustment results

Obtaining the network adjustment results for the TAMDEF network turned out to be a challenging task, indeed, since it involved a very long and rigorous process. This process was followed in accordance with the suggested strategies (Case I-IV) described in Chapter 3. The obtained results are illustrated and discussed in the following sections.

5.5.1 SCLESS results

As mentioned in Chapter 3, the TAMDEF network was processed with respect to IGS sites located in Antarctica, South America, Africa and Australia by using the SCLESS least-squares approach described in Section 3.3.2. Figures 5.20 to 5.28 show the time-series for the adjusted north (dn), east (de) and up (du) coordinate components for the three TAMDEF sites with longest data spans (FTP1, MCM4 and ROB1) for the year 2000-2005. The statistics of the time-series coordinate components for dn, de and du (Case I-IV) are illustrated in Table 5.8 for the sites tested.

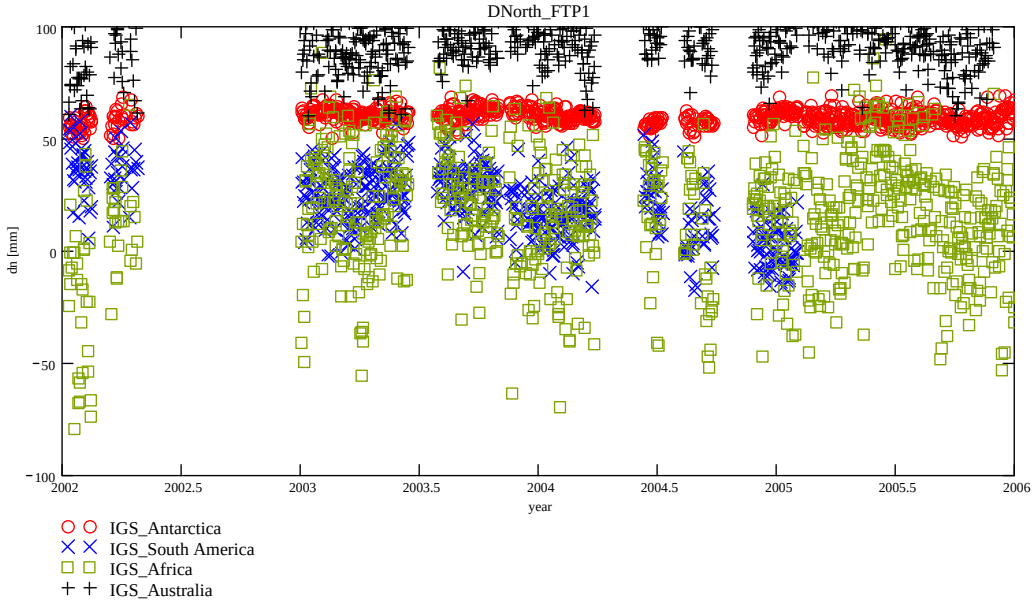

Figure 5.20: Adjusted north coordinate component (dn): All solutions for the FTP1 site.

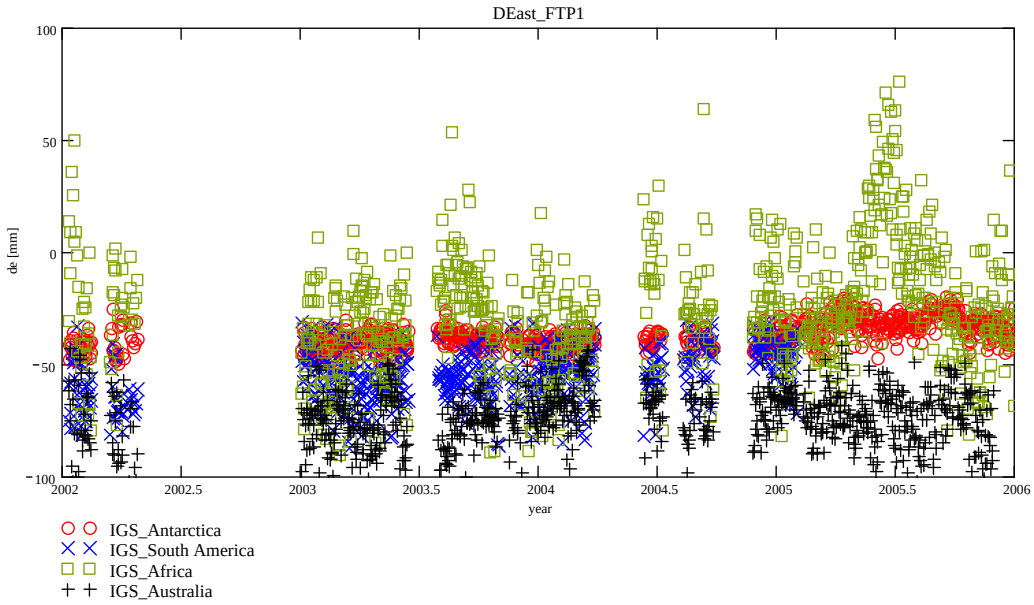

Figure 5.21: Adjusted east coordinate component (de): All solutions for the FTP1 site.

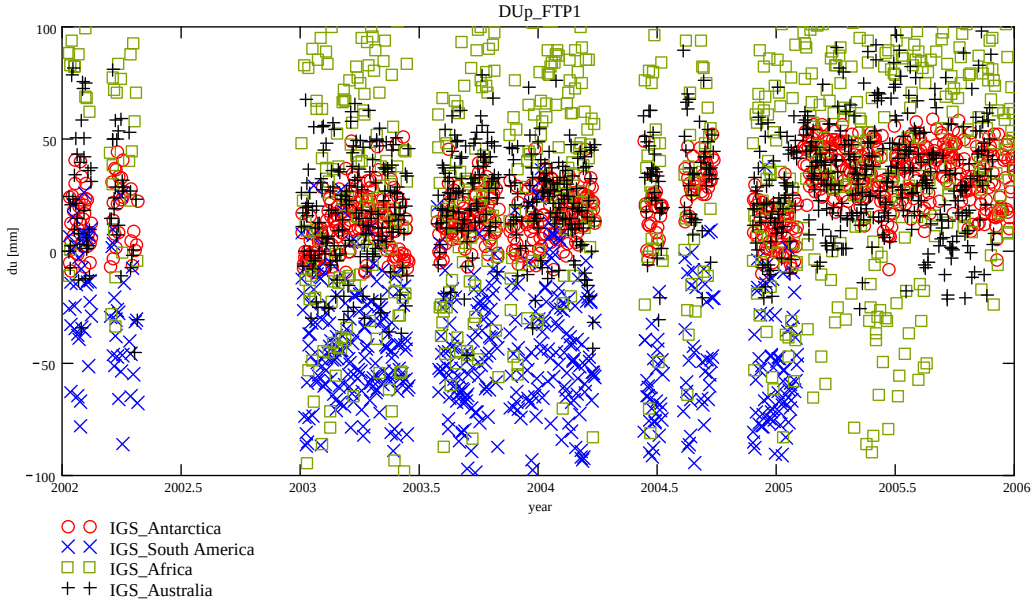

Figure 5.22: Adjusted up coordinate component (du): All solutions for the FTP1 site.

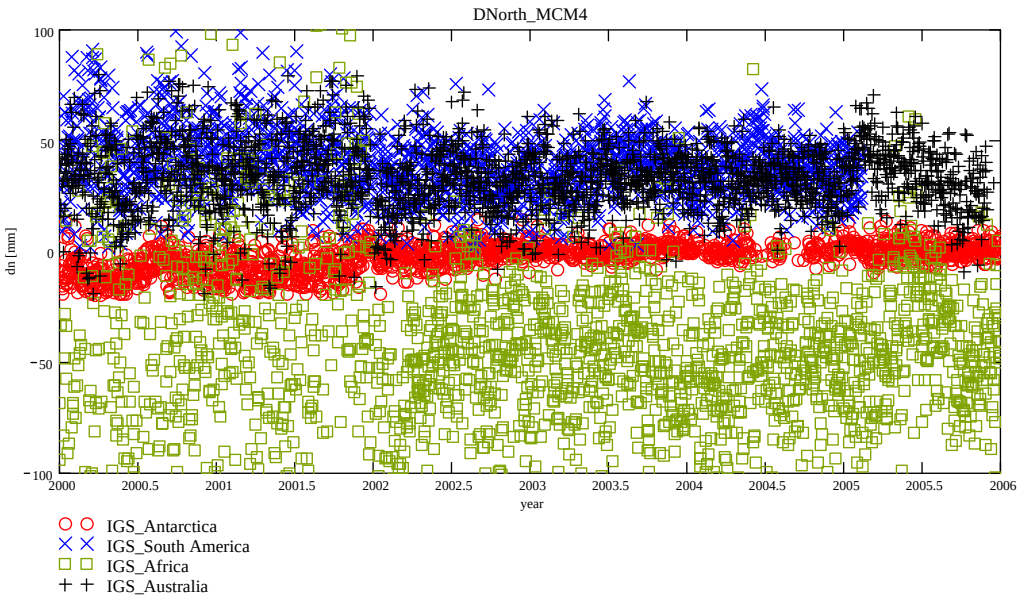

Figure 5.23: Adjusted north coordinate component (dn): All solutions for the MCM4 site.

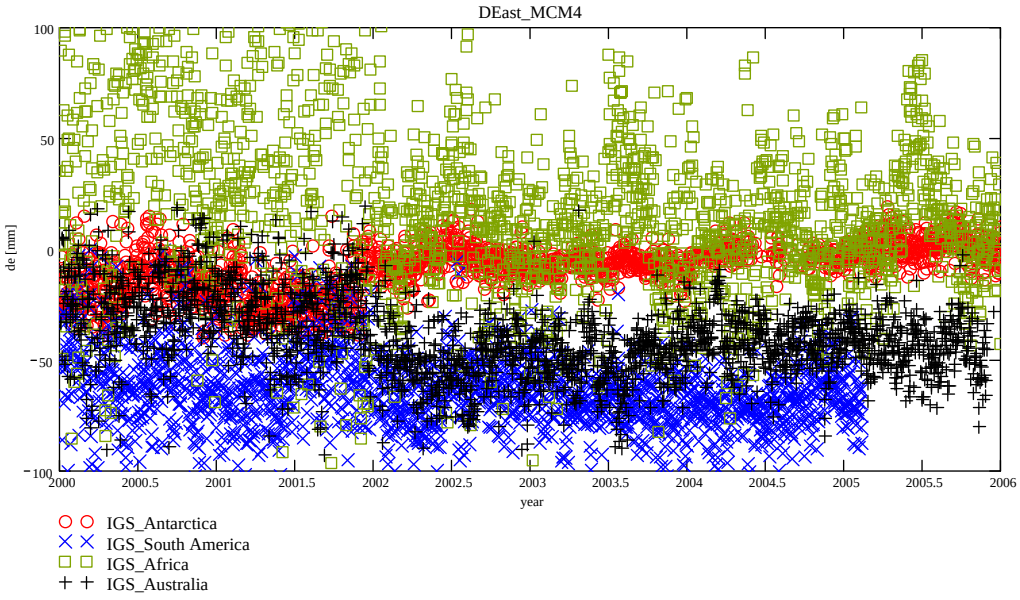

Figure 5.24: Adjusted east coordinate component (de): All solutions for the MCM4 site.

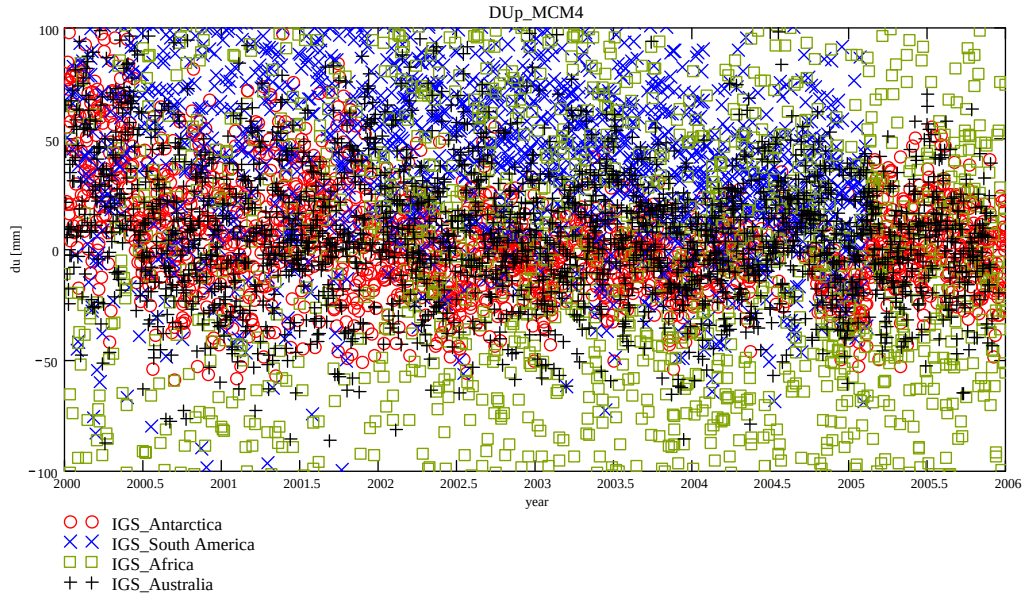

Figure 5.25: Adjusted up coordinate component (du): All solutions for the MCM4 site.

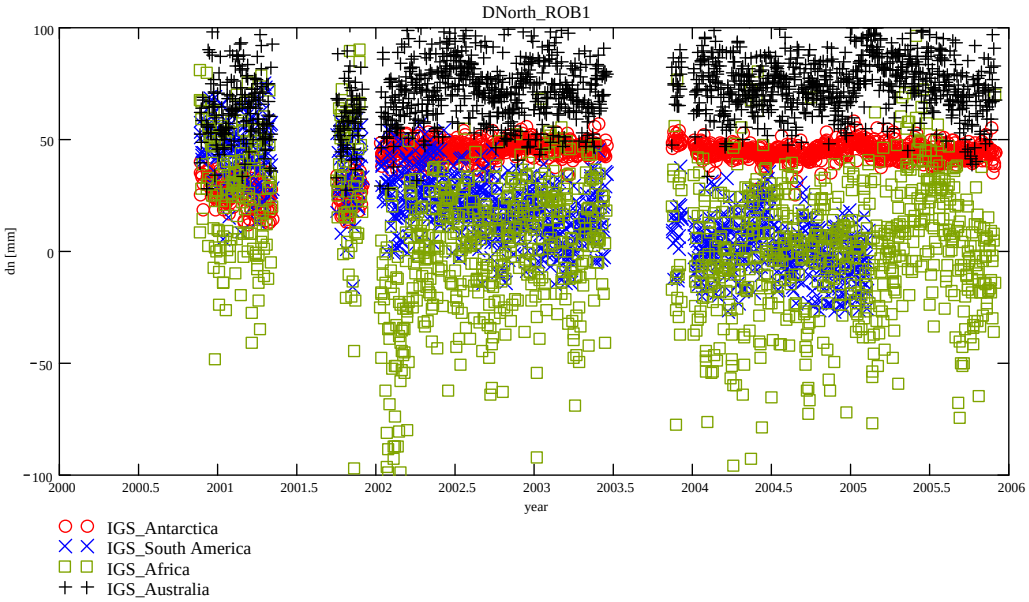

Figure 5.26: Adjusted north coordinate component (dn): All solutions for the ROB1 site.

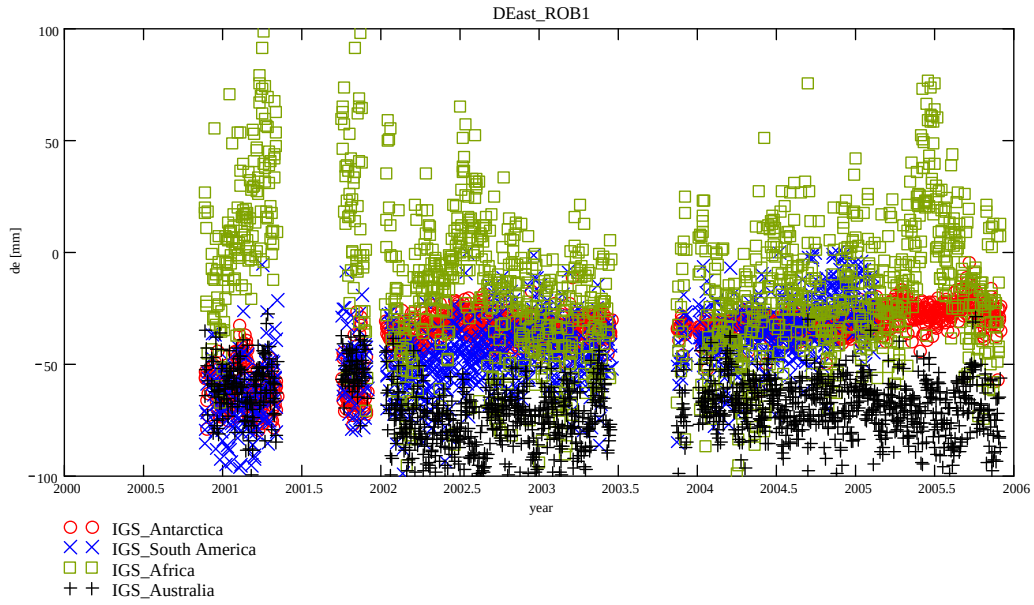

Figure 5.27: Adjusted east coordinate component (de): All solutions for the ROB1 site.

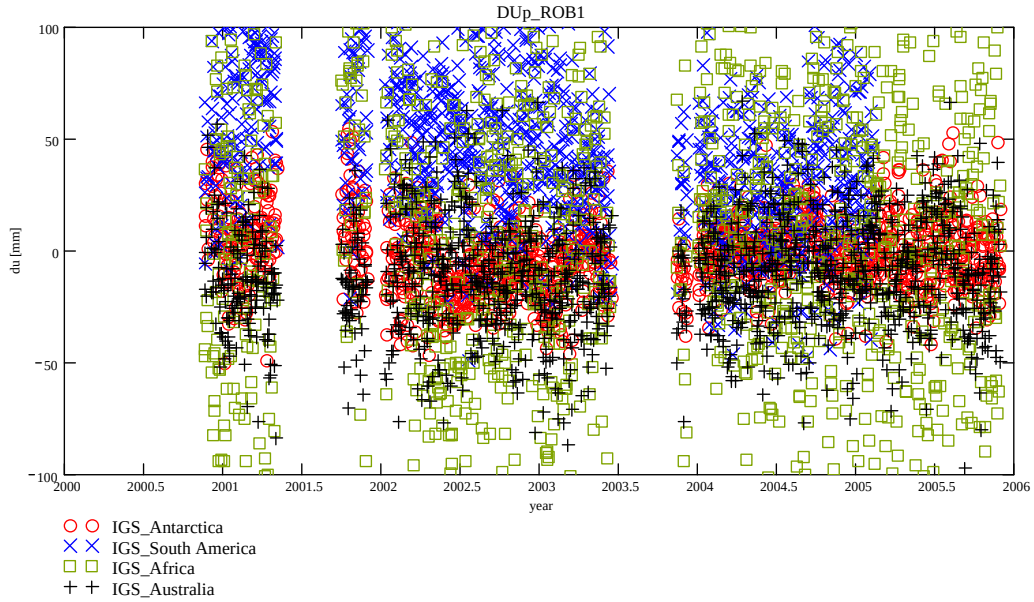

Figure 5.28: Adjusted up coordinate component (du): All solutions for the ROB1 site.

With respect to IGS Antarctica (Case I)					
Site	**Component**	**Mean (mm)**	**Min (mm)**	**Max (mm)**	**St. Dev. ± (mm)**
FTP1	dn	58.9	51.2	68.7	3.3
	de	-37.1	-48.7	-20.3	6.2
	du	20.0	-10.3	59.2	16.5
MCM4	dn	-2.6	-18.9	13.8	6.1
	de	-8.8	-38.6	18.1	10.9
	du	4.6	-59.3	98.5	24.9
ROB1	dn	41.9	12.1	57.6	7.7
	de	-35.8	-78.4	-4.6	12.6
	du	-1.2	51.0	53.4	15.8
With respect to IGS South America (Case II)					
FTP1	dn	21.7	-18.4	58.7	15.6
	de	-54.3	-86.7	-31.0	11.7
	du	-42.8	-98.8	36.6	27.9
MCM4	dn	38.7	1.3	98.5	14.6
	de	-64.6	-119.0	-0.5	18.0
	du	54.8	-98.7	198.6	50.5
ROB1	dn	15.7	-26.8	75.1	21.1
	de	-43.5	-97.5	0.2	16.5
	du	44.8	-48.4	141.9	32.9
With respect to IGS Africa (Case III)					
FTP1	dn	14.8	-78.5	95.1	26.9
	de	-27.1	-91.1	76.2	25.8
	du	53.2	-97.2	197.6	62.0
MCM4	dn	-47.9	-196.7	198.3	51.3
	de	23.0	-97.6	198.2	45.2
	du	-2.8	-198.8	199.1	98.4
ROB1	dn	3.7	-98.9	97.0	31.5
	de	-13.9	-98.6	99.4	32.1
	du	9.0	-184.7	193.8	70.5
With respect to IGS Australia (Case IV)					
FTP1	dn	93.6	61.1	118.5	12.4
	de	-74.8	-108.9	-40.8	12.6
	du	25.7	-47.3	97.4	23.9
MCM4	dn	34.1	-19.1	78.1	14.7
	de	-38.6	-93.5	19.7	16.8
	du	7.5	-8.2	99.3	30.3
ROB1	dn	72.4	26.8	117.7	14.4
	de	-68.8	-119.0	-26.8	12.8
	du	-11.3	-98.1	65.4	24.9

Table 5.8: Statistics for the dn, de and du coordinate components (cases I-IV).

It can be observed in the Figures 5.20 to 5.22 and in Table 5.8 that the scatter is smaller for the dn, de and du coordinate components for the adjusted FTP1 site for Case I (ranges within ~-50 to ~70 mm), and bigger scatter was obtained in Case III (ranges within ~-100 to ~200 mm). A positive ~+60 mm bias, a negative ~-40 mm bias and a

positive ~+20 mm could be inferred in dn, de and du coordinate components, respectively, in Case I. Case II solution reported mean values close to zero for the dn and de coordinate components in comparison with the other three cases. The smallest values in terms of the standard deviation for the three coordinate components were also found for the most consistent solution (Case I).

Figures 5.23 to 5.25 and Table 5.8 present the solution for dn, de and du coordinate components for the adjusted MCM4 site, which seem more stable when processed with respect to Case I (ranges within ~-60 to ~100 mm). Similarly to the FTP1 site, the less homogeneous solution for the MCM4 site occurs when processed with respect to Case III (ranges within ~-200 to ~200 mm) in all three coordinate components. However, even though the du coordinate component with respect to Case III looks very dispersed, its mean value was the smallest (2.8 mm), as compared to the other three cases. Again, the smallest values in terms of the standard deviation for the estimated dn, de and du coordinate components were also found for Case I.

Finally, Figures 5.26 to 5.28 and Table 5.8 present the solutions of the dn, de and du components for the adjusted ROB1 site which, in comparison to the previous two sites (FTP1 and MCM4), looks more stable when processed with respect to Case I (ranges within ~-80 to ~60 mm). This site is also the least stable when processed with respect to Case III (ranges within ~-100 to ~120 mm). A positive ~+35 mm bias could be inferred in both dn and de coordinate components, respectively, in Case I. No bias is present in the du component. Similarly to the other two sites, the best values in terms of the standard deviation for the three coordinate components were also found for the most consistent solution (Case I).

Overall, it can be concluded from the results coming from the network adjustment when using different tectonic plates for reference that the time-series reflects the quality of the solution obtained when processed TAMDEF network with respect to the Antarctic tectonic plate. In other words, the MCM4 is the site that behaves more stable in the three components with respect to Antarctic tectonic plate (Case I). To the contrary, the worst scenario (the biggest scatter of the time-series) occurs when processing TAMDEF network with respect to IGS Africa (Case III). This was expected, as in this case, longest baselines were processed. Still, the analyses presented here are useful, as they quantify to qualify of ITRF connection of the TAMDEF network in various scenarios.

5.5.1.1 Overall RMS results

The PAGES allows computing what is called the overall root mean squared (overall RMS deviations) for the processed GPS data. In other words, it provides an estimate of the RMS deviations for the entire GPS time-series as a quality indicator. According to Schenewerk *et al.* (2001) a good rule-of-thumb is that the overall RMS deviations should be less than or equal to ±0.015 meters for long baselines, as in the present case, when processed the TAMDEF GPS data with respect to other sites inside and outside Antarctica. Figure 5.29 shows the mean values for the overall RMS deviations (Case I-IV) plotted for the option with fixed ambiguity, where the mean RMS ranges from 7.7–11.4 mm, a convincing result in view of the (mostly) very long baselines. In addition, the statistics of the computed overall RMS deviations are shown

in Table 5.9, where the mean and the standard deviation values confirm that the results from the network adjustment (Case I) are more stable, in comparison to the other three solutions (cases II–IV).

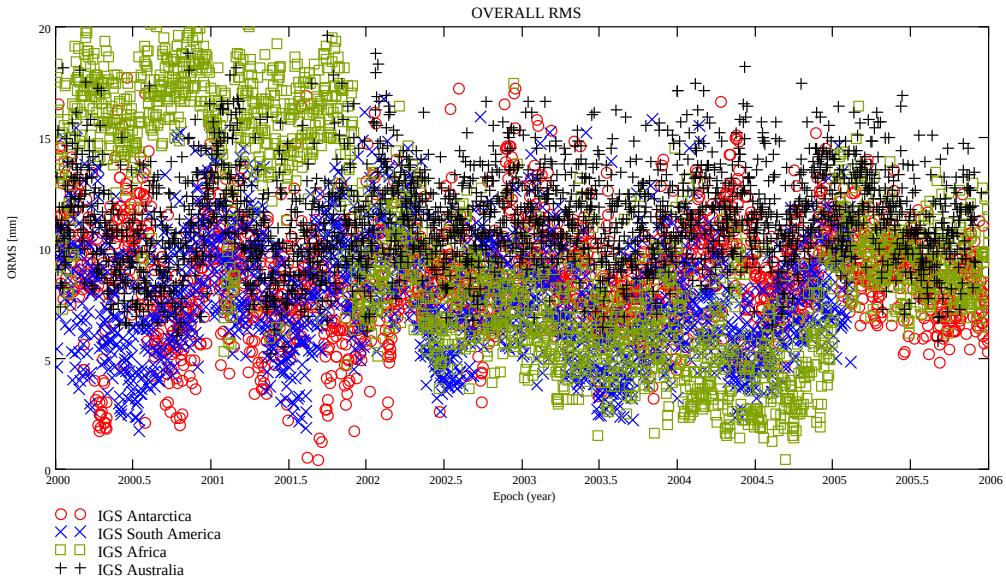

Figure 5.29: Overall RMS for deviations in the TAMDEF GPS data.

IGS Sites	Mean (mm)	Min (mm)	Max (mm)	St. Dev. ± (mm)
Antarctica	8.7	0.4	23.3	2.4
South America	7.7	1.7	16.7	2.7
Africa	10.0	0.4	23.0	4.8
Australia	11.4	5.2	24.1	2.2

Table 5.9: Overall statistics for RMS deviations in the TAMDEF GPS data.

5.5.2 GPSCOM results

The results from the GPSCOM for the four cases (Case I-IV), as described in Chapter 3 are illustrated in Table 5.10. It should be pointed out here that the results presented in Table 5.10 come from a homogeneous global network with coordinates and velocities referred and transformed to the ITRF 2000 at epoch 2005.5. It can be observed from Table 5.10 that the horizontal and vertical GPS rates of motion with respect to the IGS Antarctica (Case I) are less than $10mm/yr$. The MCM4 site has less rates of motion: $V_x = -4mm/yr\ (\pm 1.1)$; $V_y = +6mm/yr\ (\pm 1.2)$; and $V_z = +1.3mm/yr\ (\pm 0.4)$, as compared to FTP1: $V_x = -8mm/yr\ (\pm 2.6)$; $V_y = +7mm/yr\ (\pm 2.5)$; and $V_z = +6.1mm/yr\ (\pm 0.8)$ and ROB1: $V_x = -9mm/yr\ (\pm 2.1)$; $V_y = +8mm/yr\ (\pm 1.9)$; and $V_z = +1.1mm/yr\ (\pm 0.5)$. MCM4 is the site that is also more stable in the vertical with

respect to the four tectonic plates (Case I-IV): $V_z = +1.3 mm/yr\ (\pm 0.4)$ to $V_z = +1.6 mm/yr\ (\pm 0.4)$. The biggest rates of motion for the TAMDEF sites were found with respect to IGS Africa (Case III) with horizontal and vertical GPS rates up to $14 mm/yr$ or less.

IGS Antarctica (case I)						
Site	**Coordinate/Velocity**			**St. Dev. Coord. / St. Dev. Vel.**		
	$X\ [m]$	$Y\ [m]$	$Z\ [m]$	$\sigma_X \pm [m]$	$\sigma_Y \pm [m]$	$\sigma_Z \pm [m]$
	$V_X\ [m/yr]$	$V_Y\ [m/yr]$	$V_Z\ [m/yr]$	$\sigma_{V_X} \pm [m/yr]$	$\sigma_{V_Y} \pm [m/yr]$	$\sigma_{V_Z} \pm [m/yr]$
FTP1	-1172458.615	368222.124	-6237889.250	0.0190	0.0185	0.0283
	-0.0080	+0.0070	+0.0061	0.0026	0.0025	0.0008
MCM4	-1311703.188	310815.021	-6213254.908	0.0114	0.0124	0.0168
	-0.0040	+0.0060	+0.0013	0.0011	0.0012	0.0004
ROB1	-1374248.864	415169.538	-6193597.055	0.0147	0.0144	0.0273
	-0.0090	+0.0080	+0.0011	0.0021	0.0019	0.0005
IGS South America (case II)						
Site	**Coordinate/Velocity**			**St. Dev. Coord. / St. Dev. Vel.**		
	$X\ [m]$	$Y\ [m]$	$Z\ [m]$	$\sigma_X \pm [m]$	$\sigma_Y \pm [m]$	$\sigma_Z \pm [m]$
	$V_X\ [m/yr]$	$V_Y\ [m/yr]$	$V_Z\ [m/yr]$	$\sigma_{V_X} \pm [m/yr]$	$\sigma_{V_Y} \pm [m/yr]$	$\sigma_{V_Z} \pm [m/yr]$
FTP1	-1172458.601	368222.112	-6237889.223	0.0153	0.0116	0.0272
	-0.0090	+0.008	+0.0068	0.0033	0.0021	0.0014
MCM4	-1311703.174	310815.013	-6213254.853	0.0151	0.0173	0.0514
	-0.0050	+0.008	+0.0014	0.0021	0.0029	0.0003
ROB1	-1374248.841	415169.519	-6193597.020	0.0201	0.0177	0.0339
	-0.0110	+0.009	+0.0017	0.0032	0.0027	0.0002
IGS Africa (case III)						
Site	**Coordinate/Velocity**			**St. Dev. Coord. / St. Dev. Vel.**		
	$X\ [m]$	$Y\ [m]$	$Z\ [m]$	$\sigma_X \pm [m]$	$\sigma_Y \pm [m]$	$\sigma_Z \pm [m]$
	$V_X\ [m/yr]$	$V_Y\ [m/yr]$	$V_Z\ [m/yr]$	$\sigma_{V_X} \pm [m/yr]$	$\sigma_{V_Y} \pm [m/yr]$	$\sigma_{V_Z} \pm [m/yr]$
FTP1	-1172458.591	368222.098	-6237889.193	0.0268	0.0269	0.0616
	-0.0110	+0.0090	+0.0072	0.0031	0.0030	0.0025
MCM4	-1311703.138	310814.987	-6213254.002	0.0508	0.0443	0.0971
	-0.0070	+0.0090	+0.0016	0.0025	0.0027	0.0004
ROB1	-1374248.833	415169.503	-6193596.984	0.0301	0.0314	0.0716
	-0.0140	+0.0120	+0.0014	0.0052	0.0039	0.0003
IGS Australia (case IV)						
Site	**Coordinate/Velocity**			**St. Dev. Coord. / St. Dev. Vel.**		
	$X\ [m]$	$Y\ [m]$	$Z\ [m]$	$\sigma_X \pm [m]$	$\sigma_Y \pm [m]$	$\sigma_Z \pm [m]$
	$V_X\ [m/yr]$	$V_Y\ [m/yr]$	$V_Z\ [m/yr]$	$\sigma_{V_X} \pm [m/yr]$	$\sigma_{V_Y} \pm [m/yr]$	$\sigma_{V_Z} \pm [m/yr]$
FTP1	-1172458.616	368222.1235	-6237889.249	0.0189	0.0185	0.0283
	-0.0120	+0.0080	+0.0071	0.0029	0.0020	0.0014
MCM4	-1311703.189	310815.0208	-6213254.907	0.0114	0.0124	0.0168
	-0.0060	+0.0070	+0.0015	0.0016	0.0021	0.0002
ROB1	-1374248.863	415169.5379	-6193597.054	0.0147	0.0144	0.0273
	-0.0130	+0.0100	+0.0012	0.0034	0.0026	0.0003

Table 5.10: ITRF00 coordinates/velocities for TAMDEF sites at epoch 2005.5 (cases I-IV).

In general, it can be stated that TAMDEF sites are more stable with respect to IGS Antarctic sites (Case I), which seems intuitive since the TAMDEF is located on the Antarctic tectonic plate. Overall up to $14 mm/yr$ rates of motions were recorded for the tested TAMDEF sites. Furthermore, it can be found in (Willis, 2008) that the horizontal GPS rates of motions for the Antarctic plate are up to $15 mm/yr$ to the southeast. On the other hand, Rülke *et al.* (2008) found vertical deformation values within ($-4 mm/yr$ to $+18 mm/yr$) for the Antarctic continent.

Based of the obtained rates of motion that generally verify the earlier reports by ibid., it can be concluded that GPS should be able to detect meaningful horizontal motions within Antarctica, but it is crucial to properly implement the data reduction strategies to distinguish the various motion components in the GPS-sensed total displacement (e.g., multipath, ocean tide loading, antenna effects, troposphere, etc.)

5.5.3 Alternative network adjustment results

An analysis and coordinate comparison is presented for the PAGES results versus the alternative network adjustment (described in Sections 3.4.2, 3.4.3 and 3.4.4) using the previously developed algorithms and software (i.e., Snow and Schaffrin, 2004). Figure 5.30 shows the proposed geometry for the alternative geodetic network in case of a singular least-squares adjustment.

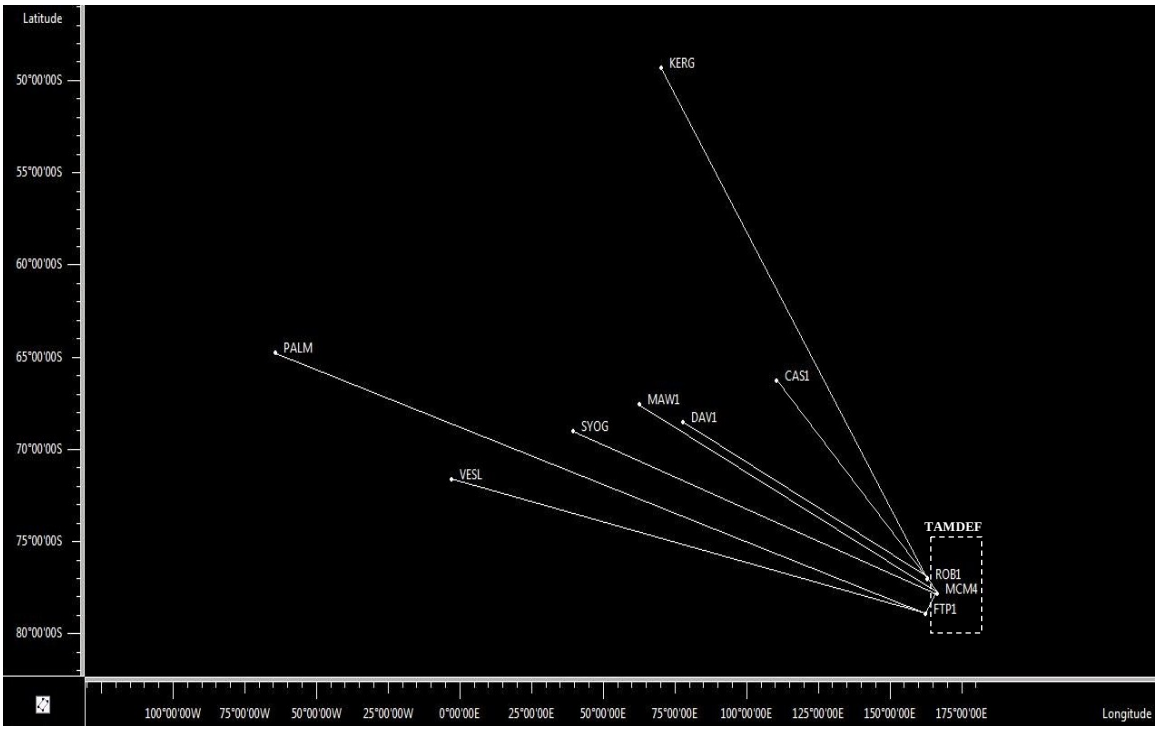

Figure 5.30: Alternative geodetic network design.

To be consistent with the proposed scenario for Case I (see Section 3.2), a GPS network with 6 IGS stations and one none-IGS was analyzed. For the 10 GPS stations involving 30 parameters (coordinates) were estimated. As mentioned before, the *a priori* coordinates for the 10 GPS stations involved in the adjustment come from a previous adjustment using the PAGES software; here it was assumed that the GPS baseline components should only vary at the random noise level. Table 5.11 shows the resulting coordinates and their corresponding standard deviations with respect to the *a priori* values.

SCLESS (PAGES)						
Site	$X\ [m]$	$Y\ [m]$	$Z\ [m]$	$\sigma_X \pm [m]$	$\sigma_Y \pm [m]$	$\sigma_Z \pm [m]$
FTP1	-1172458.615	368222.124	-6237889.250	0.0190	0.0185	0.0283
MCM4	-1311703.188	310815.021	-6213254.908	0.0114	0.0124	0.0168
ROB1	-1374248.864	415169.538	-6193597.055	0.0147	0.0144	0.0273
MINOLESS						
FTP1	-1172458.618	368222.121	-6237889.253	0.0193	0.0182	0.0286
MCM4	-1311703.185	310815.024	-6213254.911	0.0111	0.0127	0.0165
ROB1	-1374248.867	415169.529	-6193597.053	0.0150	0.0141	0.0271
Partial-MINOLESS						
FTP1	-1172458.619	368222.123	-6237889.252	0.0194	0.0184	0.0281
MCM4	-1311703.183	310814.026	-6213254.909	0.0112	0.0129	0.0163
ROB1	-1374248.869	415169.531	-6193596.051	0.0152	0.0143	0.0269
BLIMPBE						
FTP1	-1172458.617	368222.122	-6237889.252	0.0192	0.0183	0.0285
MCM4	-1311703.184	310815.025	-6213254.910	0.0110	0.0128	0.0164
ROB1	-1374248.868	415169.530	-6193597.054	0.0151	0.0142	0.0272

Table 5.11: Coordinate comparison between PAGES and the alternative network adjustment approaches.

The results from the stochastically constrained least-squares adjustment (SCLESS), performed with PAGES, are very comparable (at the mm level) with respect to those obtained from the alternative network adjustment approaches (MINOLESS, Partial-MINOLESS and BLIMPBE). It can be pointed out that the results from MINOLESS should guarantee that the vector of coordinate changes would be the smallest with respect to the other two solutions; however, results from both partial-MINOLESS and BLIMPBE are very similar to those from MINOLESS (showing 1-2 mm differences), and it seems that there is no reason to suspect any bias among the resulting coordinates. Thus, GPS data used for the TAMDEF network are consistent to the point that various adjustment methods gave equivalent results. Hence, it can be concluded that the alternative approaches experimented in this research for TAMDEF network can also be used as an alternative when performing least-squares adjustment for other GPS networks. Furthermore, the objective of performing such comparison fulfills the requirements of validating the previous approach developed for this application (i.e., Snow and Schaffrin, 2004).

5.6 PWV results

This section illustrates the estimated GPS PWV results, in comparison with the radiosonde PWV and numerical weather prediction models (AMPS). First, three different mapping functions, namely $m_{wet}Niell(E)$, $m_{wet}CfA(E)$ and $m_{wet}Mar(E)$ with their corresponding tropospheric models of type, Saastamoinen and Marini (described in Chapter 4), were investigated in estimating the wet delay from GPS measurements. The estimated wet delay was then converted to PWV using the approach discussed in Chapter 4. Next, in order to determine the quality of GPS derived PWV, the estimates for MCM4 were compared to the McMurdo radiosonde measurements of PWV. As a final point, since the GPS PWV estimates are able to reproduce the variability seen in the radiosonde measurements, the GPS values were then compared with the extracted PWV values from the AMPS. To make this possible, it was required to use external meteorological information (i.e., surface temperature and pressure). The PAGES software allows three options for troposphere estimation (refer to Section 4.3.1). Three of the TAMDEF sites with longer data spans (FTP1, MCM4 and ROB1) were investigated to decide which mapping function and tropospheric model ought to be used for the GPS PWV estimation (see Table 5.12). The statistics presented in Table 5.12 were generated for GPS PWV time-series between the years 2000 and 2005; here, the Marini mapping function with the Marini model performs with the highest reliability on the TAMDEF data, as indicated by the values for the mean and the standard deviations, which are 30-40% smaller than for other mapping functions. Hence, hereinafter the GPS PWV results were generated using the Marini mapping function with the Marini model.

Site	Mapping Function and Model	Max (mm)	Mean (mm)	St. Dev. ± (mm)
FTP1	Niell with Saastamoinen	12.5	4.2	3.2
	CfA-2.2 with Saastamoinen	13.7	5.0	3.5
	Marini with Marini	10.3	3.7	2.4
MCM4	Niell with Saastamoinen	14.2	6.4	4.5
	CfA-2.2 with Saastamoinen	15.7	7.3	4.6
	Marini with Marini	10.8	4.2	2.6
ROB1	Niell with Saastamoinen	12.3	6.2	4.5
	CfA-2.2 with Saastamoinen	14.7	7.0	4.7
	Marini with Marini	9.9	3.4	2.3

Table 5.12: Statistics of GPS PWV for the FTP1, MCM4 and ROB1 sites by using different mapping functions and tropospheric models.

Figures 5.31 to 5.33 illustrate the GPS PWV time-series, computed for each of the tested TAMDEF sites. The GPS PWV ranges from 0 to 10 mm for the FTP1, MCM4 and ROB1 sites. A clear seasonal effect can be observed in the graph for MCM4, with more noise in PWV for 2002, before the replacement of the station's hardware. The values for the PWV are higher in summer and lower in winter, due to the greater moisture storing capacity of the warmer summer atmosphere. The FTP1 and ROB1 PWV estimates look nosier in comparison with MCM4, and the seasonal effect barely seen. The reason for more noise in these data is not fully understood and requires more investigation. In

addition, some statistics of the GPS PWV results for each of the three analyzed TAMDEF sites are presented in Table 5.13.

Site	Mapping Function & Tropospheric Model	Maximum (mm)	Mean (mm)	Standard Deviation ± (mm)
FTP1	**Marini**	10.3	3.7	2.4
MCM4	**Marini**	10.8	4.2	2.6
ROB1	**Marini**	9.9	3.4	2.3

Table 5.13: GPS PWV statistics for TAMDEF sites with a data span from 2000 to 2005.

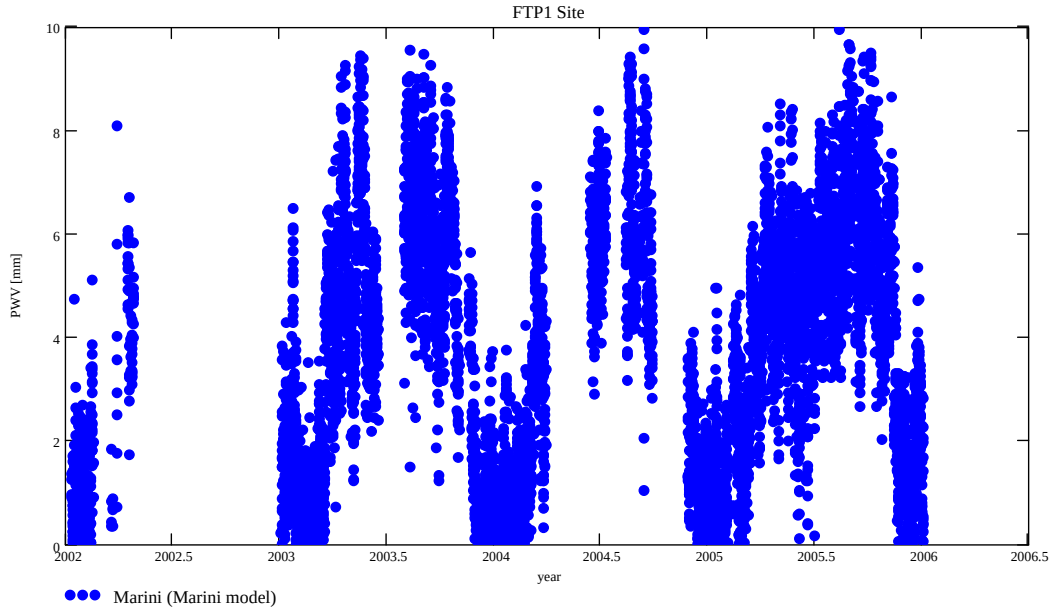

Figure 5.31: GPS PWV time-series at the FTP1 site.

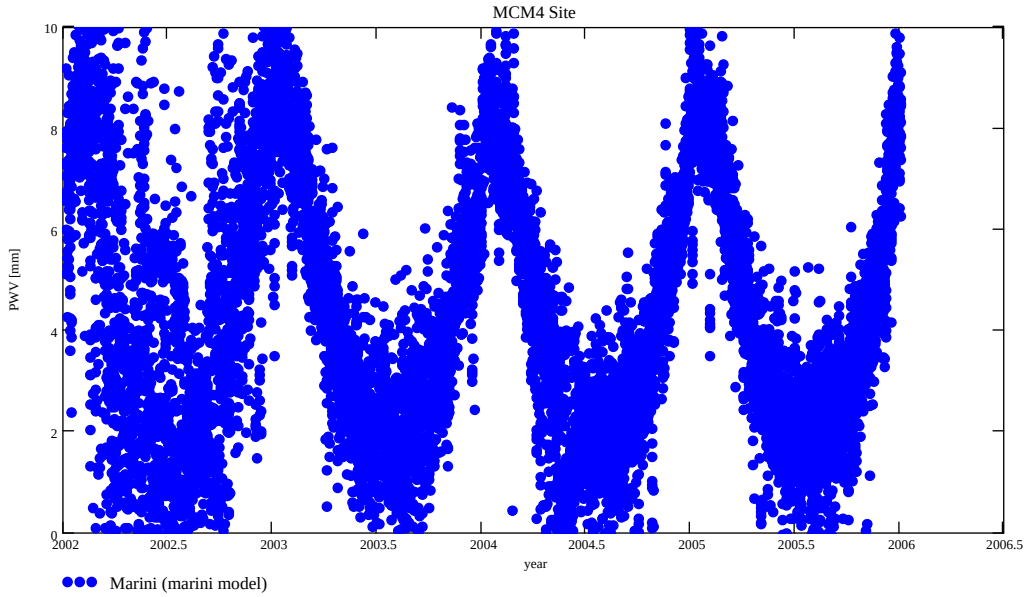

Figure 5.32: GPS PWV time-series at the MCM4 site.

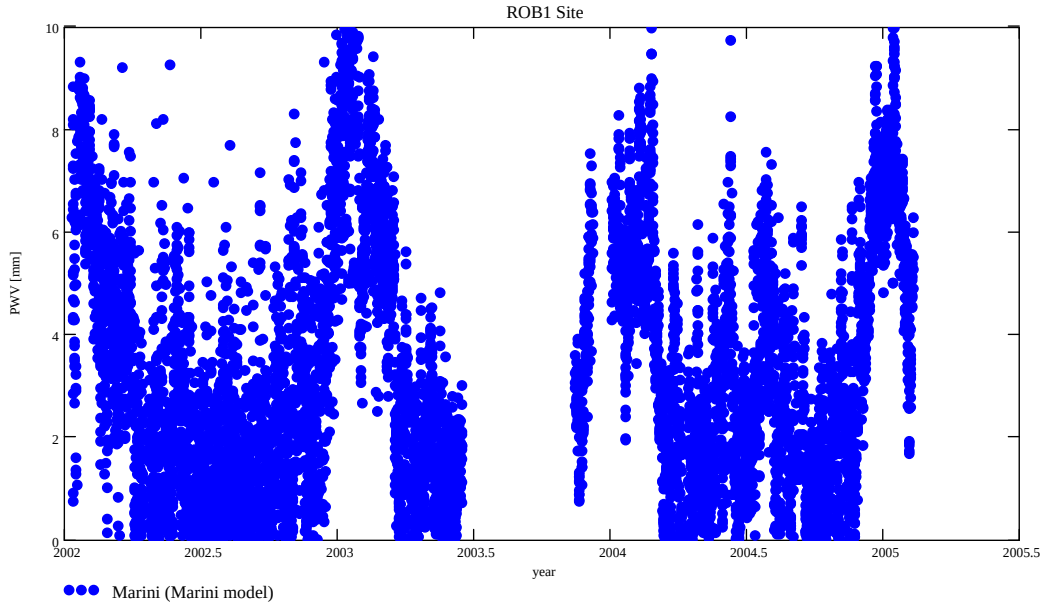

Figure 5.33: GPS PWV time-series at the ROB1 site.

Figure 5.34 illustrates the comparison between GPS PWV using external meteorological information (surface temperature and pressure) with radiosonde PWV data at the MCM4 site for the year 2004. It can be observed that GPS PWV (estimated every 3 hours) consistently exceeds the radiosonde PWV values (estimated every 12 hours). Therefore, Figure 5.35 shows the one-to-one comparison between the GPS PWV and radiosonde PWV at the same site (MCM4) that shows more coincidence than the previous comparison.

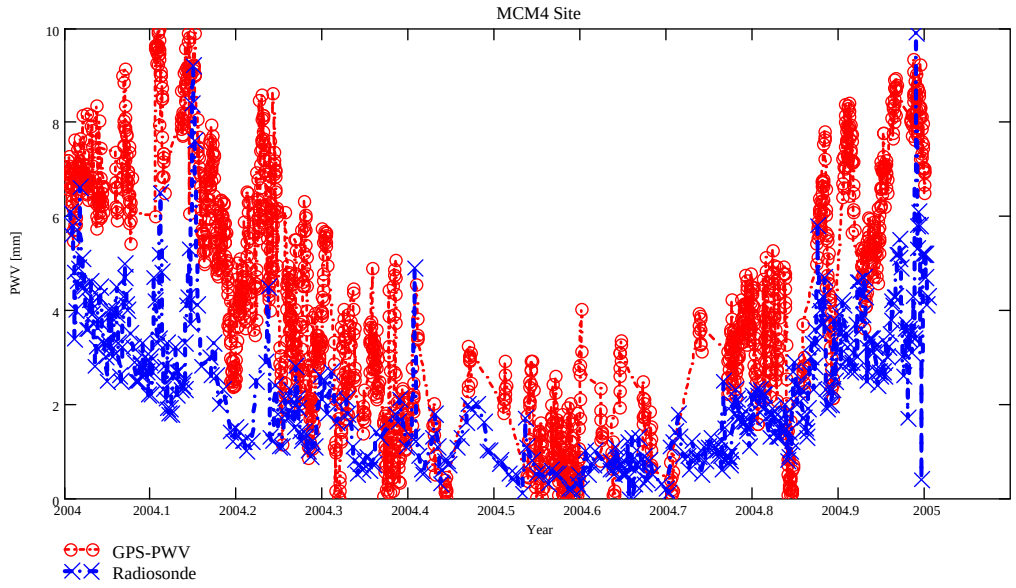

Figure 5.34: GPS PWV (estimated every 3 hours) vs. radiosonde PWV values (estimated every 12 hours) at the MCM4 site.

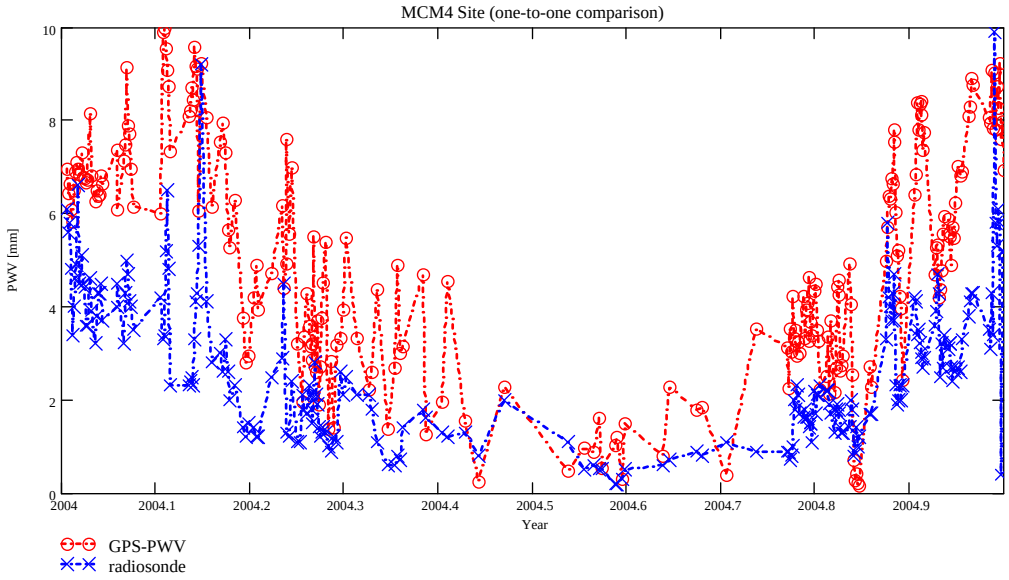

Figure 5.35: One-to-one comparison of GPS PWV (estimated every 12 hours) vs. radiosonde PWV values (estimated every 12 hours) at the MCM4 site.

Table 5.14 illustrates the statistics for the one-to-one comparison of GPS PWV (estimated every 12 hour) vs. Radiosonde PWV values (estimated every 12 hour) at MCM4.

Site	PWV	Maximum (mm)	Mean (mm)	Standard Deviation ± (mm)
MCM4	**From Radiosonde**	9.9	2.7	1.6
MCM4	**From GPS**	9.9	4.9	2.4
MCM4	**Radiosonde - GPS**	0.0	-2.2	0.8

Table 5.14: Statistics of the one-to-one comparison of GPS PWV vs. radiosonde PWV at the MCM4 site.

In order to more closely investigate these differences, monthly mean comparisons between the radiosonde, AMPS, and the GPS PWV values are shown in Figure 5.36.

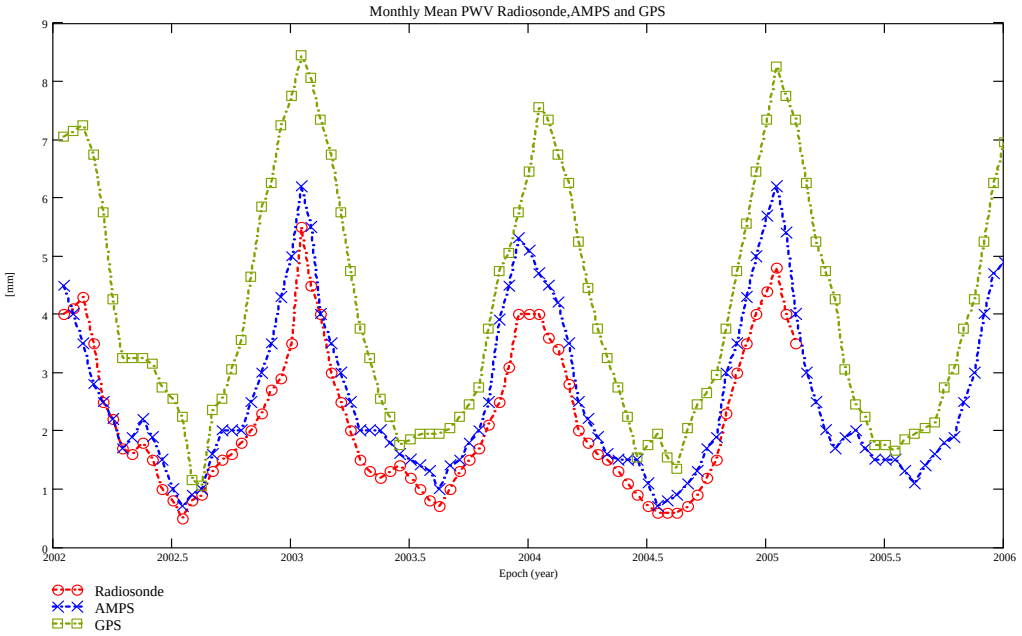

Figure 5.36: Monthly mean PWV comparisons at the MCM4 site.

Statistics of these PWV values at MCM4 are shown in Table 5.15.

MCM4 Site	Mean (mm)	Standard Deviation ±(mm)
GPS PWV	3.9	1.9
AMPS PWV	2.6	1.4
Radiosonde PWV	2.2	1.3

Table 5.15: GPS PWV statistics at the MCM4 site.

In addition, the biases were analyzed by season, following the proposed classification:
Annual = average for the whole year (i.e., mean value for AMPS minus mean value for GPS PWV for the entire year);
DJF = December - January - February average (i.e., austral summer);
MAM = March - April - May average (i.e., austral fall);

JJA = June - July - August average (i.e., austral winter); and
SON = September - October - November average (i.e., austral spring).

The results from the above classification are shown in Table 5.16, with the smallest values of the bias during the winter and the highest values during the summer. Overall, 2002 was the year with the biggest bias (it ranges from -0.36 to -4.32). Note that * indicates that no PWV data were available for 2005 to compare them with GPS PWV.

Biases	DJF	MAM	JJA	SON	Annual
2002	-4.32	-1.91	-0.89	-0.98	-3.47
2003	-1.06	-0.59	-0.32	-0.35	-1.67
2004	-0.50	-0.34	-0.21	-0.25	-1.08
2005	-0.36	*	*	*	-0.20
Overall	-1.96	-0.95	-0.47	-0.53	-2.07

Table 5.16: Biases in PWV by season (AMPS-GPS) at the MCM4 site.

Figure 5.37 presents a plot of the monthly means from another continuously tracking station (ROB1) situated north-east of MCM4, in a more marine environment. A better alignment can be observed, as compared to MCM4, with the mean bias of -0.79 mm (larger in summer). Here, the PAGES software was used, but considering only annual means for external surface temperature and surface pressure. This result requires special attention and further investigation.

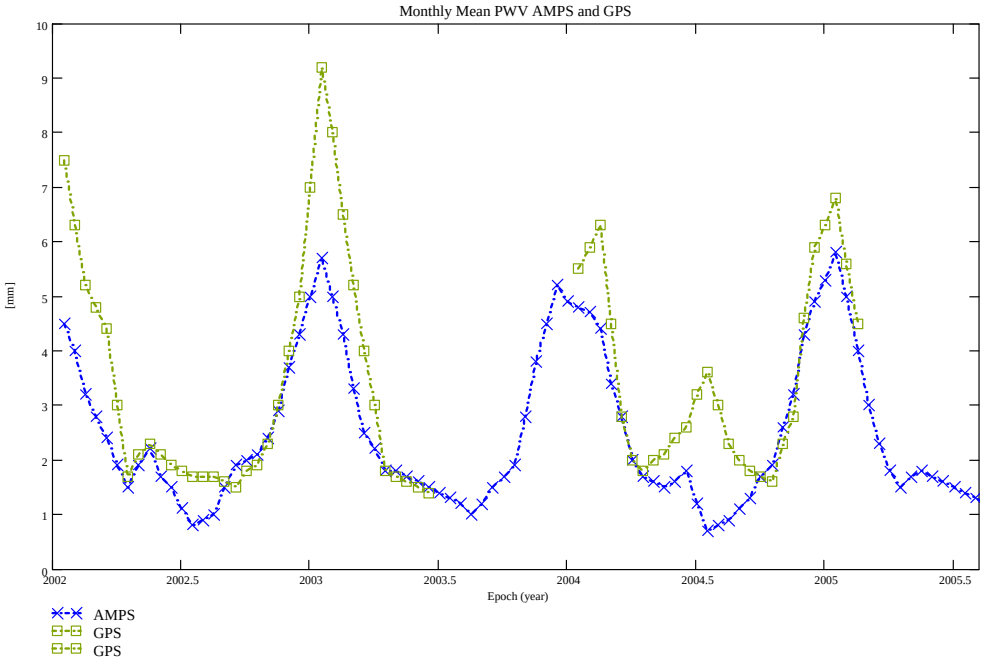

Figure 5.37: Monthly mean comparisons at the ROB1 site.

Figure 5.38 shows the auto-covariance for the GPS PWV values computed for each of the three tested TAMDEF sites (FTP1, MCM4 and ROB1). It can be observed that the signal does not decorrelate for any of the three stations analyzed in the experiment. Further investigation may be required if surface meteorological data become available in the future.

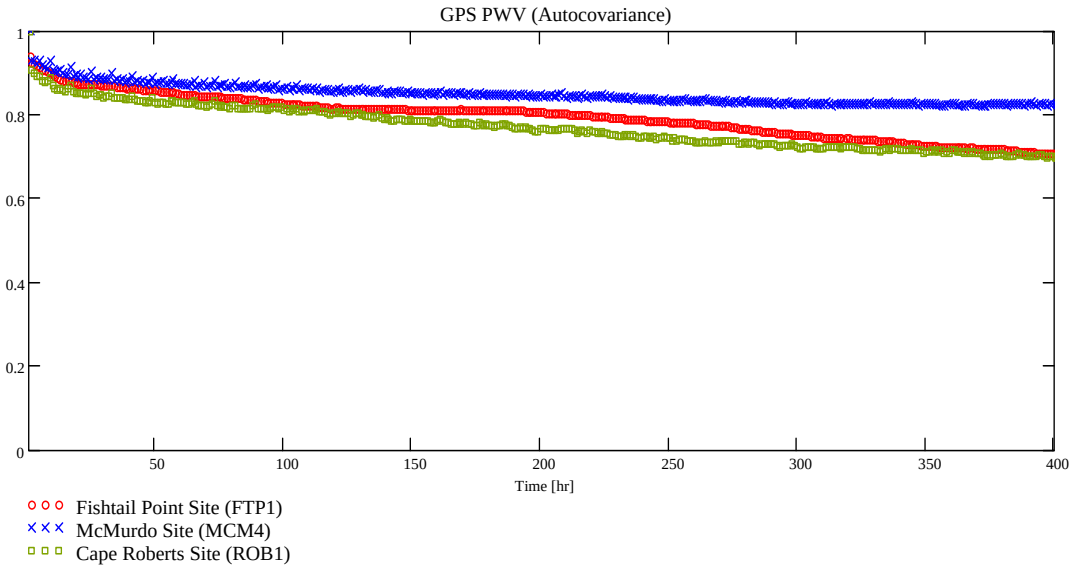

Figure 5.38: GPS PWV auto-covariance at the FTP1, MCM4 and ROB1 sites.

Summarizing, the GPS PWV estimates for the MCM4 site were compared to the radiosonde and the AMPS PWV, this comparison revealed a consistent positive bias of ~2.3 mm with respect to radiosonde and a 1.5 mm with respect to AMPS. A potential contributor to this bias could be the antenna phase center variation at the MCM4 site, which has not been calibrated (refer Section 5.3.1). Note that the antenna phase center miscalibration (or the lack of proper calibration parameters) will directly impact the PWV estimates, http://dbx.cr.chiba-u.jp/Gps_Met/gpsmet/gpsmet_jp/gpsmet_jp.html. Another potential contributor could be the PAGES software that uses specific values for the coefficients of the linear regression between surface temperature and T_m in the procedure to estimate water vapor from the wet zenith delay (refer Equations 4.18 and 4.20). These coefficients were derived exclusively under U.S. conditions. These values might not be appropriate for the Antarctic TAMDEF stations since the tropospheric conditions there are different from those experienced by GPS stations across the U.S.

Furthermore, in order to validate the total wet zenith delay (TWZD) estimates at the MCM4 site using PAGES software, these estimates were directly compared to the TWZD computed every 3-hours by the CDDIS analysis center (ftp://cddisa.gsfc.nasa.gov) as shown in Figure 5.39. Some statistics of the differences between both solutions are presented in Table 5.17. The results of the TWZD between the PAGES and the CDDIS analysis center are very comparable with 1.1 mm difference in the mean value and ±0.4 mm in this standard deviation value. Also, the range from both solutions looks similar, with only less than 1% difference with respect to the

minimum value; thus the reason of the small positive bias in the GPS PWV should come from another source.

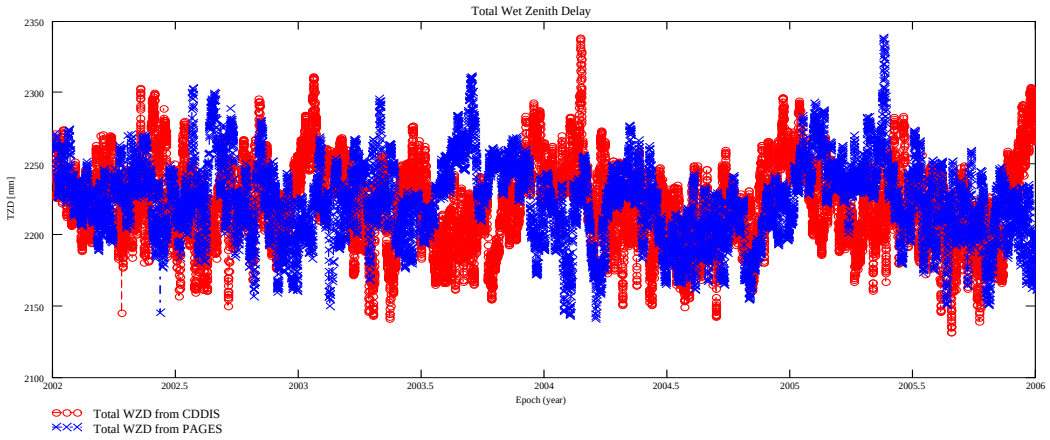

Figure 5.39: Total wet zenith delay at the MCM4 site estimated by PAGES & CDDIS.

Total WZD	Max (mm)	Min (mm)	Mean (mm)	St. Dev. ±(mm)
From CDDIS	2338.4	2131.4	2221.85	27.97
From PAGES	2338.7	2141.0	2222.92	27.57
CDDIS - PAGES	-0.3	-9.6	-1.07	0.40

Table 5.17: Statistics of the total wet zenith delay at the MCM4 site.

CHAPTER 6

CONCLUSIONS, CONTRIBUTIONS, AND OUTLOOK

6.1 Summary and conclusions

The primary objectives of this research were in identifying and investigating various aspects of GPS geodesy in Antarctica, together with the appropriate methodology for the quality assessment and suitable data processing schemes for the Antarctic environment. To accomplish these objectives, a variety of factors and requirements that may have impact on the deformation monitoring networks in Polar Regions were taken into account. Furthermore, the obtained results are expected to provide key information to improve position accuracies and interpretation of broad, continental-scale crustal motion patterns (bedrock motions) detected by sparse, regionally distributed continuous GPS trackers, such as the TAMDEF (Trans Antarctic Mountains Deformation) network at Victoria Land.

Based on the analysis of the various practical and theoretical aspects presented through this research for the TAMDEF network the following conclusions can be drawn:

For the topic related to the antennae testing, it can be concluded that the standard antenna calibration models from NGS that was used for each antenna involved in the experiment presented did not result in any significant variation in the daily results, but showed mm-level variations in the hourly results. Thus, based on this fact, the antenna types tested here could be employed in future TAMDEF or similar Antarctic campaigns, where 24-hour solutions are normally used for deformation monitoring.

From the multipath analysis it was revealed that MCM4 is the TAMDEF site, which is most affected by the influence of local pseudorange multipath (between 1 to 4m in MP1-RMS and MP2-RMS, respectively), and this is not good at all, since MCM4 is the primary ITRF access point for this part of Antarctica. An explanation of high levels of multipath at the MCM4 site could be due to the switch of the receiver in January 3, 2002, because the same antenna has been in use at the MCM4 since 1995 up to present. Another potential reason for the high multipath might be the condensation inside its radome and the antennae surrounding environment. At present, the pseudorange multipath can be used for further data cleaning to improve the positioning results.

The outcomes of the Ocean Tide Modeling (OTM) analysis revealed that the vertical component for the tested TAMDEF sites is more stable when using CATS02.01 model in comparison with the TPXO6.2. This fact might be attributed to CATS02.01 model being a regional hydrodynamic model that best assimilates the bathymetry of the Antarctic region. The results obtained in this section validate the importance of a suitable choice of OTM in Antarctic GPS, in order to ensure that GPS measurement in and across this region can successfully discover crustal motion.

Furthermore, the results derived from the computed rates of motion for the TAMDEF sites among different IGS sites from other tectonic plates reveal that the biggest rates of motion for the TAMDEF sites occur with respect to IGS Africa (Case III) with horizontal GPS rates within 7 to 14 mm. In general, the TAMDEF sites seem to be more stable with respect to the IGS Antarctic sites (Case I), which is a reasonable result, since TAMDEF is located well inside the Antarctic tectonic plate. In addition, the length of the baseline vectors is smaller, as compared with sites on the other tectonic plates (case II-IV) outside of Antarctica. Overall, up to ~14 mm/yr rates of motion were recorded for the tested TAMDEF sites. Similar results for the rates of motion for the TAMDEF network are also shown by Rülke *et al.* (2008) and Willis (2008), though only for Case I.

From the network adjustment process, when analyzing the TAMDEF network connection to ITRF via IGS stations (Case I) and outside (Case II-IV) of Antarctica, it was concluded that the time series results look more stable (in the horizontal and vertical coordinate components) when processing TAMDEF network with respect to the Antarctic tectonic plate. Additionally, the results from the stochastically constrained least-squares adjustment (SCLESS) obtained with PAGES are very comparable (at the mm level) to those results obtained from the proposed alternative adjustment approaches (MINOLESS, partial-MINOLESS and BLIMPBE). In particular, the results from MINOLESS should guarantee that the vector of coordinate changes would be the smallest with respect to the other two solutions; the results from the partial-MINOLESS and BLIMPBE are very similar to those from MINOLESS (within 1-2 mm differences), and it seems that there is no reason to suspect any bias among the resulting coordinates. In addition, the alternative methodology and experimental algorithms in this research regarding the TAMDEF network can also be considered as a good choice when performing a least-squares adjustment for other GPS networks. Hence, it can be demonstrated that the GPS data used are largely free of bias after proper care has been taken of ionosphere, troposphere, multipath and some other sources that affect GPS positioning, when processed for Case I-IV.

From the water vapor analysis it was deduced that GPS PWV estimates for the TAMDEF network is site and data dependent; for example, a clear seasonal effect can be observed for MCM4, with noisy PWV for the year 2002, before the replacement of the station hardware. On the other hand, the FTP1 and ROB1 PWV estimates look noisier in comparison with MCM4, and the seasonal effect is barely seen. This might be attributed to the fact that no external meteorological information was available for FTP1 and ROB1, as compared to MCM4. The GPS PWV estimates for the MCM4 site were compared to the radiosonde and the AMPS PWV; this comparison revealed a consistent positive bias of ~2.3 mm with respect to radiosonde and a 1.5 mm bias with respect to AMPS. A probable contributor to this bias could be the antenna radome at the MCM4 site that has not been calibrated yet, plus the a and b coefficients involved in the surface temperature to T_m conversion, used in PWV estimation procedure.

Overall, it can be concluded that no suspected bias was present in the obtained results; thus, GPS is capable of capturing the signal which can be used for further geophysical interpretation within Antarctica.

The following are the primary contributions of this research:

- Based on a pilot study, this research presented a comprehensive analysis of the various aspects of GPS geodesy in Antarctica, specifically for the TAMDEF network.
- Optimal GPS data processing, based on proper algorithms and scientific software, data analysis and data quality assessment was implemented in order to achieve most precise geodetic results.
- A hardware test of different antenna types in the TAMDEF network and a pseudorange multipath analysis of the TAMDEF sites.
- First analysis of GPS data from the TAMDEF network was used to validate two ocean tide models for Antarctica in order to support the detection of vertical rates of motion.
- Testing of different least-squares and other estimates to validate the least-squares algorithm coded in the PAGES software were performed.
- Interpretation and verification of the geodetic link between the TAMDEF network and the ITRF has been provided.
- A complete procedure to compute GPS PWV by means of the estimated total wet zenith delay using external meteorological information and validation of the GPS PWV with radiosonde PWV and AMPS PWV has been established. This procedure has a potential for real-time application.

The following discusses the outlooks for further research that is directly associated with the findings of this report:

- All the antenna tests, as presented in this research, could be used in future TAMDEF campaigns; this means that results on this issue can serve as good guidance to any future use of GPS equipment in Antarctica.
- Based on the pseudorange multipath results, it is suspected that the hardware used at the MCM4 site might be one of the reasons for the high multipath there; thus, more investigations are required on this issue.
- Introducing GPS derived PWV to weather/climate models could improve the model's predictive capability, and would allow a better understanding of the Antarctic weather conditions (and climate). Hence, it is very positive to substantially extend the understanding of the McMurdo region.
- Equation for $T_m = a + bT_s$ can be customized for Antarctica when sufficient amount of surface meteorological data became available.

BIBLIOGRAPHY

Anderson, O. B., Woodworth, P. L. and Flather, R. A. (1995). Intercomparison of recent ocean tide models. *Journal of Geophysical Research* 100(C12), 25261-25282.

Beutler, G., I.I. Mueller, and R.E. Neilan. (1996). The International GPS Service for Geodynamics (IGS): The story, in *Proceedings, International Association of Geodesy Symposia No. 115, GPS Trends in Precise Terrestrial, Airborne, and Spaceborne Applications*, Springer-Verlag, New York.

Bevis, M., Businger, S., Herring, T.A., Rocken, C., Anthes, R.A. and Ware, R.H. (1992). GPS meteorology: Remote sensing of atmospheric water vapor using the global positioning system. *Journal of Geophysical Research* 97, l5.787-15.801.

Bevis, M., Businger S., Chiswell, S.R., Herring, T.A., Anthes, R.A., Rocken, C. and Ware, R.H. (1994). GPS meteorology: Mapping zenith wet delay onto precipitable water. *Journal of Applied Meteorology*, 33 379-386.

Bevis, M., Chiswell, S. and Businger, S. (1996). Estimating wet delays using numerical weather analyses and predictions. *Radio Science*, 31, (3), 477-487.

Boucher, C., Altamimi, Z. and Sillard, P. (1998). Results and analysis of the ITRF96. *IERS Tech. Note* 24, Central Bureau of IERS, Observatoire de Paris, France.

Boucher, C., Altamimi, Z. and Sillard, P. (1999). The 1997 International Terrestrial Reference Frame (ITRF-97). *IERS Tech. Note* 27, Central Bureau of IERS, Observatoire de Paris, France.

Boucher, C. and Altamimi, A. (2001). Availability of the ITRF2000 Primary Solution. World Wide Web Address: http://www.iers.org/iers/publications/niessages/

Bromwich, D.H., and Fogt, R.L. (2004). Strong trends in the skill of the ERA-40 and NCEP/NCAR Reanalyses in the high and middle latitudes of the Southern

Hemisphere, 1958-2001. *Journal of Climate*, Vol. 17, 4603-4619.

Chao, C. (1973). A model for tropospheric calibration from daily surface and radiosonde balloon measurement, *Technical Memorandum 391-350*, Jet Propulsion Laboratory, Pasadena, California.

Davis, J.L., Herring, T.A., Shapiro, I., Rogers, A. E. and Elgered, G. (1985). Geodesy by radio interferometry: Effects of atmospheric modeling errors on estimates of baseline length. *Radio Science* 20 (6), 1593-1607.

Dietrich, R. (2001). Present Status of the SCAR GPS Epoch Campaigns. In *SCAR Report No. 20*, pages 15-18,Cambridge, UK.

Dietrich, R., Dach, R., Engelhardt, G., Ihde, J., Korth, W., Kutterer, H.-J., Lindner, K., Mayer, M., Menge, F., Miller, H., Müller, C., Niemeier, W., Perlt, J., Pohl, M., Salbach, H., Schenke, H.-W., Schöne, T., Seeber, G., Veit, A., and Völksen, C. (2001). ITRF coordinates and plate velocities from repeated GPS campaigns in Antarctica – an analysis based on different individual solutions. *Journal of Geodesy* 74 (11/12) 756-766.

Dietrich, R. and Rülke, A. (2002). The SCAR GPS Campaigns in the ITRF2000. In *SCAR Report No. 21*.

Dietrich, R., Rülke, A., Ihde, J., Lindner, K., Millerd, H., Niemeiere, W., Schenkef H.-W., and Seeber G. (2004). Plate kinematics and deformation status of the Antarctic Peninsula based on GPS. Global and Planetary Change 42: 313-321.

Dietrich, R., A. Rülke (2008): A Precise Reference Frame for Antarctica from SCAR GPS Campaign Data and Some Geophysical Implications. In: Capra, A., Dietrich, R. (eds.): *Geodetic and Geophysical Observations in Antarctica – An Overview in the IPY Perspective*, Springer-Verlag Berlin Heidelberg, pp. 1-10.

Dillinger, W. H. (1978). Helmert block higher level system. *Proceedings of the Second International Symposium on Problems Related to the Redefinition of North American Geodetic Networks*, 417-426.

Dodson A.H., Shardlow, P.J., Hubbard, L.C., Elegered, G. and Jarlemark P.O. (1996), Wet Tropospheric effects on precise relative GPS height determination. *Journal of Geodesy* 70 (4) 188-202.

Dodson, A. H., Meng, X., and Roberts G. W. (2001). Adaptive Method for Multipath Mitigation and Its Applications for Structural Deflection Monitoring. *Proceedings of International Symposium on Kinematic Systems in Geodesy, Geomatics and Navigation*, Banff Alberta, Canada 101-110.

Eckl, M.C., Snay, R.A., Soler, T.A., Cline, M.W. and Mader, G.L. (2001). Accuracy of GPS-derived relative positions as a function of interstation distance and observation-session duration. *Journal of Geodesy*, *75*, 633-640.

Egbert, G. D., Bennett, A. F. and Foreman, M. G. (1994). TOPEX/POSEIDON tides estimated using a global inverse model. *Journal of Geophysical Research*, 99(C12), 24,821–24,852.

Egbert, G. D. and Erofeeva, S.Y. (2002). Efficient inverse modeling of the barotropic ocean tides. *Journal of Atmospheric and Ocean Technology*, Vol.19, N2, 183-204.

Emardson, T. R. (1998). Studies of atmospheric water vapor using the Global Positioning System. *Technical Report* No. 339, Chalmers University of Technology.

Erofeva, L. (2003). Personal communication.

Estey, L.H., Meertens, C.M. (1999). TEQC: the multi-purpose toolkit for GPS/GLONASS data. GPS Solutions (3)1:42–49

Ge, L., Han, S., and Rizos C. (2000). Multipath Mitigation of Continuous GPS Measurements Using an Adaptive Filter. *GPS Solutions*, 4(2), 19-30.

Ge, L., Han, S., and Rizos C. (2002). GPS Multipath Change Detection in Permanent GPS Stations. *Survey Review*, 36(283), 306-322.

Han, S. and Rizos, C. (1997). Multipath Effects on GPS in mine environments. *X International Congress of the International Society for Mine Surveying, Fremantle, Australia*, 447-457.

Helmert, F. R. (1880). Die mathematischen und physikalischen Theorien der höheren Geodäsie. 1. Teil. Leipzig, 631 pp.

Hilla, S. and Cline, M. (2002). Evaluating Pseudorange Multipath Effects at Stations in the National CORS Network. *Proceedings of the Weiko A. Heiskanen Symposium in Geodesy*, Department of Geodetic Science and Surveying The Ohio State University, Columbus, Ohio, on CD.

Hofmann-Wellenhof, B., Lichtenegger, H., and Collions, J. (1997). *GPS Theory and Practice*, 4th ed., Springer-Verlag, Wien Austria.

Ifadis, I. (1986), The Atmospheric Delay of Radio Waves: Modelling The Elevation Dependence on a Global Scale. *Licentiate Thesis, Technical Report No 38L*, Department of Chalmers University of Technology, Gothenburg, Sweden.

Ifadis, I. (1987). Contribution to the Study of the Atmospheric Refraction, on Radiowaves Used in Modern Geodetic Techniques in Long Distance Measurements, *Thesis Report*, vol. IA'6, School of Engineering, Faculty of Civil Engineering, Thessaloniki, Greece.

James, T.S., and Ivins, E.R. (1998). Predictions of Antarctic crustal motions driven by present-day ice sheet evolution and by isostatic memory of the Last Glacial Maximum, *Journal of Geophysical Research, 103*, 4993-5017.

Kaplan, E. D. (1996) *Understanding GPS: Principles and Applications*, Artech House, Boston, London.

King, M., Penna, N., and Clarke, P. (2005). Validation of ocean tide models around Antarctica using onshore GPS and gravity data. *Journal of Geophysical Research, 110*, B08401. doi:10.1029/2004JB003390.

Koch, K.R. (1999). *Parameter Estimation and Hypothesis Testing in Linear Models*, 2nd edn., Springer, Berlin/Heidelberg/New York.

Kuang, S. (1996). *Geodetic Network Analysis and Optimal Design*, Ann Arbor Press, Chelsea, Michigan.

Lancaster, P., and Salkauskas, K. (1986). *Curve and Surface Fitting: An Introduction*. Academic Press, Harcourt Brace Jovanovich: New York.

Liou, Y.A., and Teng, Y.T. (2001). Comparison of precipitable water observations in the near tropics by GPS, microwave radiometer, and radiosondes. *Journal of Applied Meteorology*, 40, 5–15

Liu J., Sun Z., Liang H., Xu X., and Wu P. (2005). Precipitable water vapor on the Tibetan Plateau estimated by GPS, water vapor radiometer, radiosonde, and numerical weather prediction analysis and its impact on the radiation budget. *Journal of Geophysical Research*, Vol. 110, D17106.

Mader, G.L., Schenewerk, M.S., Ray, J.R., Kass, W.G., Spofford, P.R., Dulaney, R.L. and Pursell, D.G. (1995). GPS orbit and earth orientation parameter production at NOAA for the International GPS Service for Geodynamics for 1994 in Zumberge, J.F. *et al.*, (eds) *International GPS Service for Geodynamics, 1994 Annual Report*, 197-212, Jet Propulsion Lab., California Institute of Technology, Pasadena, CA.

Mader, G. (1999). GPS antenna calibration at the National Geodetic Survey. *GPS Solutions*, 3(1), 50-58.

Marini, J.W. (1972). Correction of satellite tracking data for an arbitrary tropospheric profile, *Radio Science*, Vol. 7 (2), 223-231.

Marshall, J., Schenewerk, M., and Snay, R. (2001). The Effect of the MAPS Weather Model on GPS-Determined Ellipsoidal Heights. *GPS Solutions* 5 (1), 1-14.

Meertens, C. (2000). The Antenna and Multipath Calibration System website: http://www.unavco.ucar.edu/projects/active_projects/amcs

Niell, A.E. (1996). Global mapping functions for the atmosphere delay at radio wavelengths, *Journal of Geophysical Research*, Vol. 101, (B2), 3227-3246.

Padman, L., Fricker, H. A., Coleman, R., Howard, S. and Erofeeva L. (2002). A new tide model for the Antarctic ice shelves and seas. *Ann. Glaciol.* 34, 247-254.

Rizos, C. (1999). Quality Issues in Real-time GPS Positioning. IUGG Congress, Birmingham, U.K.

Roberts, G.W., Meng, X., Dodson, A.H., and Cosser E. (2002). Multipath Mitigation for

Bridge Deformation Monitoring. *Journal of Global Positioning System* 1(1), 25-33.

Rülke, A., R. Dietrich, M. Fritsche, M. Rothacher, P. Steigenberger (2008): Realization of the Terrestrial Reference System by a reprocessed global GPS network. *Journal of Geophysical Research*, Vol. 113, B08403, doi:10.1029/2007JB005231.

Rülke, A. and R. Dietrich (2007). "The SCAR GPS Campaigns in the context of global reference system realization and geodynamic research." Antarctica: A Keystone in a Changing World – Online Proceedings of the10th ISAES A. K. Cooper, C. A. Raymond *et al* (eds), USGS Open-File Report 2007-1047, Extended Abstract 146.

Saastamoinen, I. I. (1973), Contribution to the theory of atmospheric refraction, *Bulletin Géodésique*, 107, 13– 34. doi:10.1007/BF02522083.

Satirapod, C., Khoonphool, R. and Rizos, C. (2003). Multipath Mitigation of Permanent GPS Stations Using Wavelets. *Proceedings of 2003 International Symposium on GPS/GNSS*, Tokyo, Japan, 133-139.

Schaffrin, B. and Iz, H.B. (2002). BLIMPBE and its geodetic applications. In: Ádám J. and Schwartz K.P. (eds), *Vistas for Geodesy in the New Millennium*. IAG Symposium Series, 125. Springer, Berlin/Heidelberg/New York, 377-381.

Schaffrin, B. and Snow, K. (2007). Adjustment Computations, Part II. Lecture Notes, School of Earth Science, The Ohio State University, Columbus OH.

Schaffrin, B., and Bock, Y. (1988). A unified scheme for processing GPS phase observations, *Bulletin Geodesique, 62*, 142–160.

Schenewerk, M.S., Marshall, J., and Dillinger, W. (2001). Vertical Ocean Loading Deformations Derived from a Global GPS Network. *Journal of the Geodetic Society of Japan.* 47(1), 237-242.

Schenewerk, M. (2004). Workshop in PAGES. Department of Geodetic Science and Surveying, The Ohio State University, Columbus OH.

Schwiderski, E. W. (1980). Ocean Tides, Part I: Global ocean tidal equations, *Marine Geodesy*, 3, 161-217.

Seeber, G. (1993). Satellite Geodesy: Foundations, Methods, and Applications, Walter de Gruyter, New York.

Shum, C. K., Woodworth, P. L., Andersen, O. B., Egbert, G., Francis, O., King, C., Klosko, S., Le Provost, C., Li, X., Molines, J., Parke, M., Ray, R., Schlax, M., Stammer, D., Tierney, C., Vincent, P. and Wunsch, C. (1997): Accuracy assessment of recent ocean tide models, *Journal of Geophysical Research*

102 (C11), (25) 173-194.

Snow, K. and Schaffrin, B. (2003). Three-dimensional outlier detection for GPS networks and their densification via the BLIMPBE approach. *GPS Solutions* 7, 130-139.

Snow, K. and Schaffrin, B. (2004). GPS-Network Analysis with BLIMPBE: A Less Biased Alternative To Least-Squares Adjustment. *Proceedings of ION-Meeting*, (Dayton OH), M. Miller/J. Arnold (eds.), pp.614-625.

Troller, M. (2004). GPS-based determination of the integrated and spatially distributed water vapor in the troposphere. *Geodätisch-geophysikalische Arbeiten in der Schweiz*, 67.

Vey, S., Dietrich, R., Johnsen, K.P., Miao, J., and Heygster, G. (2004). Comparison of tropospheric water vapour over Antarctica derived from AMSU-data, ground-based GPS data and the NCEP/NCAR reanalysis. *Journal of Meteorology* Soc. Japan¸ 82, 259-267.

Vey, S., Dietrich, R. (2008): Validation of the Atmospheric Water Vapour Content from NCEP Using GPS Observations Over Antarctica In: Capra, A., Dietrich, R. (eds.): *Geodetic and Geophysical Observations in Antarctica – An Overview in the IPY Perspective*, Springer-Verlag Berlin Heidelberg, pp. 125-136.

Wang, Yu. (2004). Ocean Tide Modeling in the Southern Ocean. OSU Reports pp, ix – 64.

Wang J., Zhang L., and Dai A. (2005): Global estimates of water-vapor-weighted mean temperature of the atmosphere for GPS applications *Journal of Geophysical Research*, VOL. 110, D21101.

Willis, M. J. (2008a). Technologies to Operate Year-Round Remote Global Navigation Satellite System (GNSS) Stations in Extreme Environments. in Geodetic and geophysical observations in polar regions - Overview in an IPY perspective A. Capra and R. Dietrich (eds), Springer.

Willis M. J. (2008b). Crustal motion in the Antarctic interior from a decade of global positioning system measurements PhD. Thesis. *School of Earth Sciences, The Ohio State University*, Columbus OH.

Wolf, H. (1978). The Helmert block method, its origin and development. *Proceedings of the Second International Symposium on Problems Related to the Redefinition of North American Geodetic Networks*, Arlington, VA., 319-326.

Zhang, J., Bock, Y., Johnson, H., Fang, P., Williams, S., Genrich, J., Wdowinski, S. and Behr, J. (1997). Southern California Permanent GPS Geodetic Array: Error analysis on daily position estimates and site velocities. *Journal of Geophysical*

Research 102 (B8). (l8) 035-055.

ftp://amrc.ssec.wisc.edu

ftp://cddisa.gsfc.nasa.gov

ftp://igscb.jpl.nasa.gov/igscb/data/format/rinex210.txt

http://dbx.cr.chiba-u.jp/Gps_Met/gpsmet/gpsmet_jp/gpsmet_jp.html

http://itrf.ensg.ign.fr/ITRF_solutions/2000/results/ITRF2000.php

http://lareg.ensg.ign.fr/ITRF.html

http://www.geology.ohio-state.edu/TAMDEF/

http://www.grdl.noaa.gov/ANTCAL/

http://www.mmm.ucar.edu/rt/wrf/amps/

http://www.ngs.noaa.gov/GRD/GPS/DOC/pages/pages.html

http://www.ngs.noaa.gov/GRD/GPS/DOC/gpscom/gpscom.html

http://www.oso.chalmers.se/~loading

http://www.polenet.org/

http://www.unavco.org/facility/software/teqc/teqc.html

http://www.unavco.org QC v3 User Guide, UNAVCO, Document Date: March 1994.

http://www.wunderground.com/global/Region/AN/Temperature.html

APPENDIX A

GPS DATA AVAILABILITY FOR TAMDEF SITES

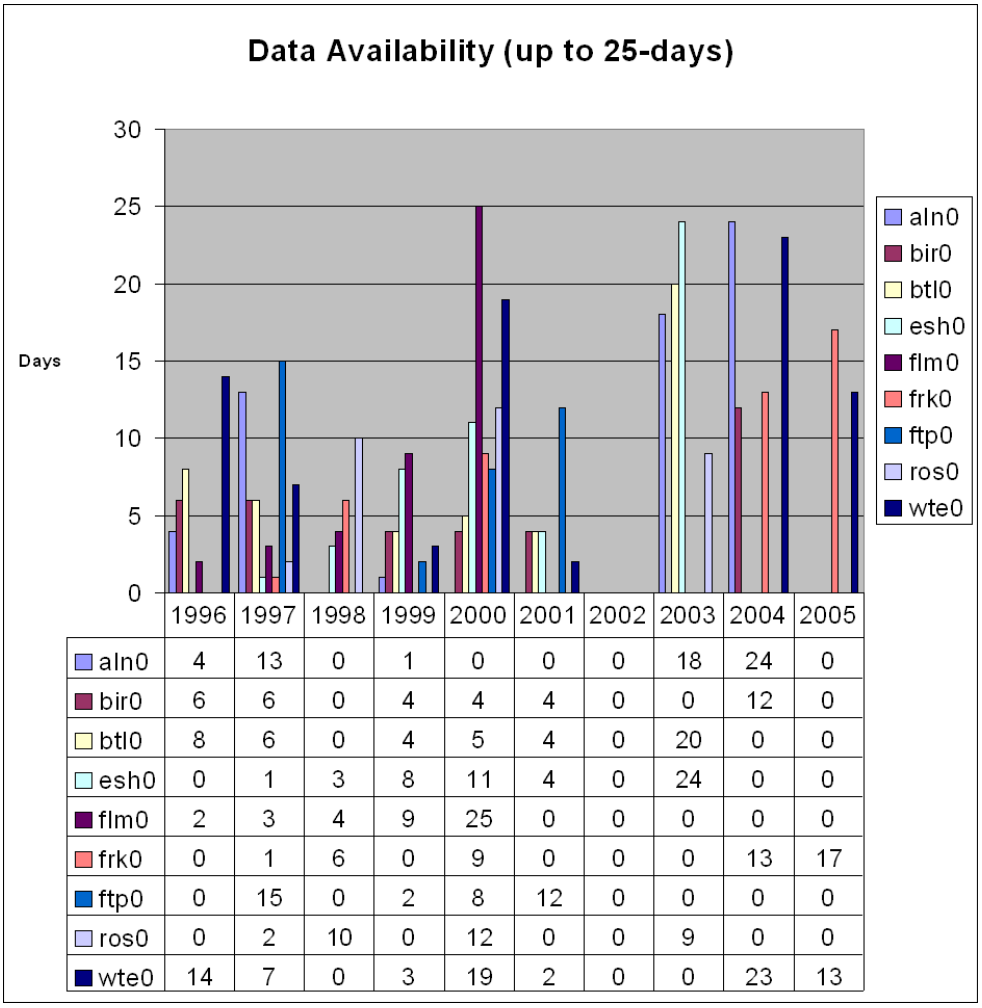

	1996	1997	1998	1999	2000	2001	2002	2003	2004	2005
aln0	4	13	0	1	0	0	0	18	24	0
bir0	6	6	0	4	4	4	0	0	12	0
btl0	8	6	0	4	5	4	0	20	0	0
esh0	0	1	3	8	11	4	0	24	0	0
flm0	2	3	4	9	25	0	0	0	0	0
frk0	0	1	6	0	9	0	0	0	13	17
ftp0	0	15	0	2	8	12	0	0	0	0
ros0	0	2	10	0	12	0	0	9	0	0
wte0	14	7	0	3	19	2	0	0	23	13

Figure A.1: TAMDEF station data availability up to 25-day duration.

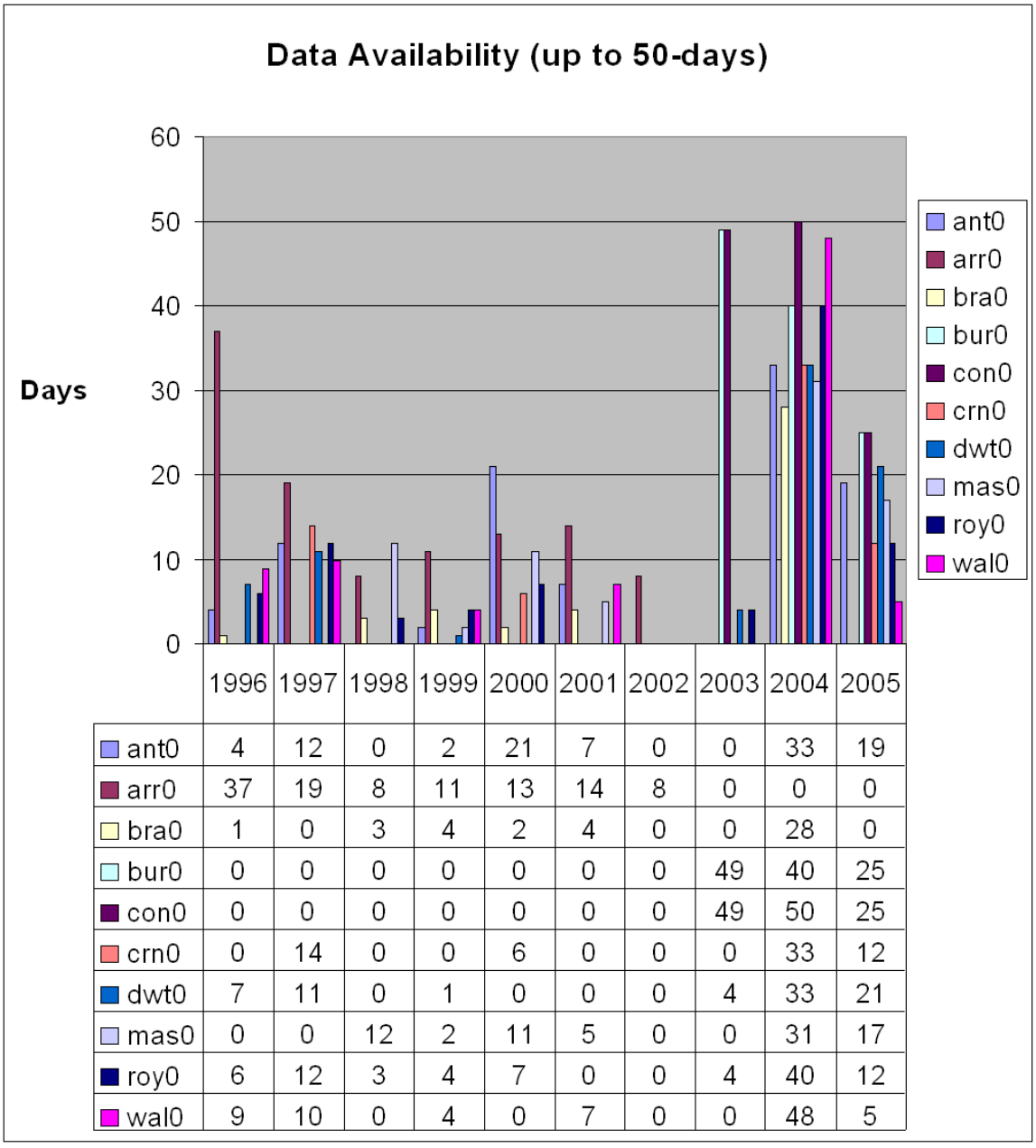

	1996	1997	1998	1999	2000	2001	2002	2003	2004	2005
ant0	4	12	0	2	21	7	0	0	33	19
arr0	37	19	8	11	13	14	8	0	0	0
bra0	1	0	3	4	2	4	0	0	28	0
bur0	0	0	0	0	0	0	0	49	40	25
con0	0	0	0	0	0	0	0	49	50	25
crn0	0	14	0	0	6	0	0	0	33	12
dwt0	7	11	0	1	0	0	0	4	33	21
mas0	0	0	12	2	11	5	0	0	31	17
roy0	6	12	3	4	7	0	0	4	40	12
wal0	9	10	0	4	0	7	0	0	48	5

Figure A.2: TAMDEF station data availability up to 50-day duration.

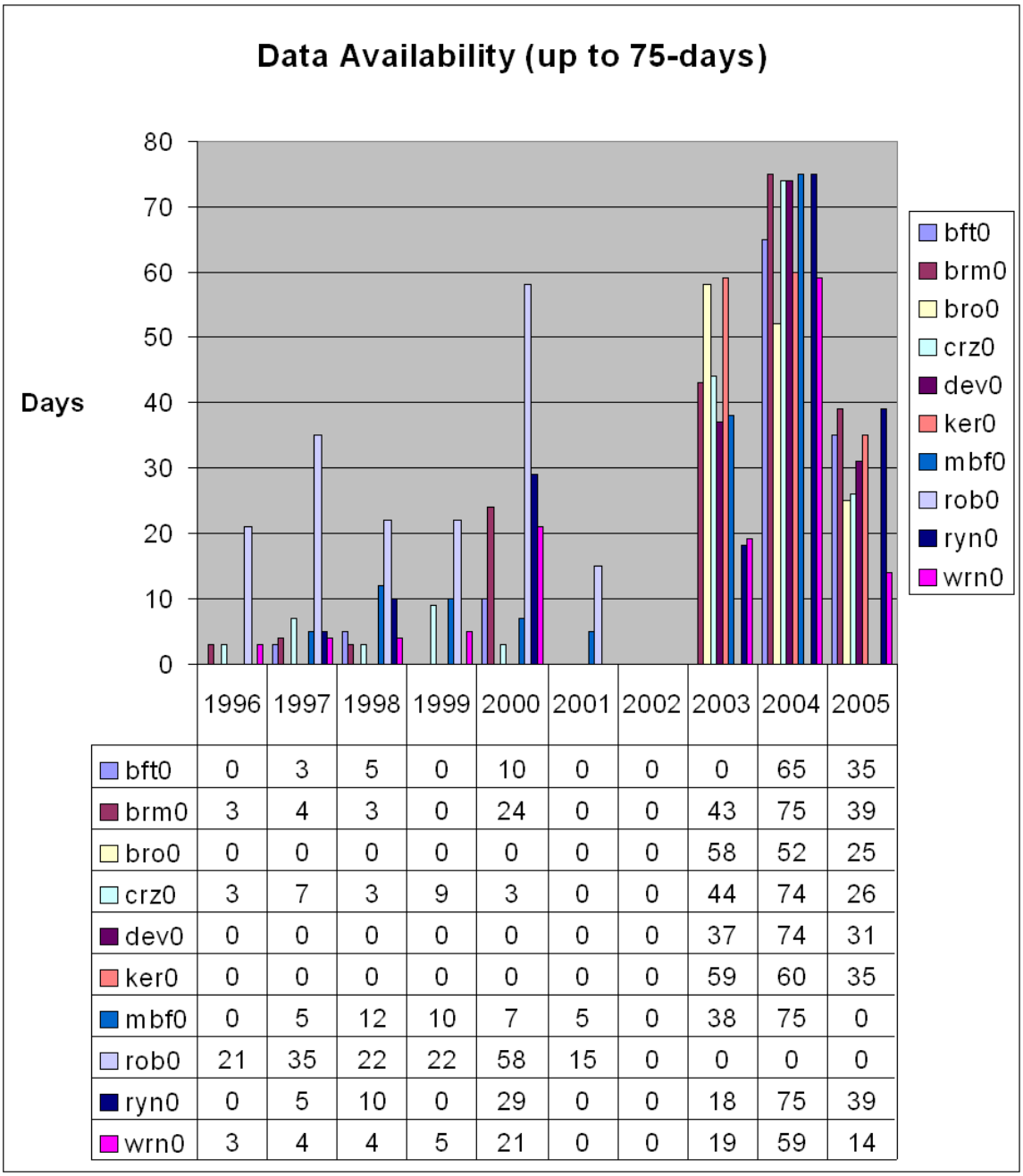

	1996	1997	1998	1999	2000	2001	2002	2003	2004	2005
bft0	0	3	5	0	10	0	0	0	65	35
brm0	3	4	3	0	24	0	0	43	75	39
bro0	0	0	0	0	0	0	0	58	52	25
crz0	3	7	3	9	3	0	0	44	74	26
dev0	0	0	0	0	0	0	0	37	74	31
ker0	0	0	0	0	0	0	0	59	60	35
mbf0	0	5	12	10	7	5	0	38	75	0
rob0	21	35	22	22	58	15	0	0	0	0
ryn0	0	5	10	0	29	0	0	18	75	39
wrn0	3	4	4	5	21	0	0	19	59	14

Figure A.3: TAMDEF station data availability up to 75-day duration.

APPENDIX B

GPS DATA AVAILABILITY FOR IGS SITES

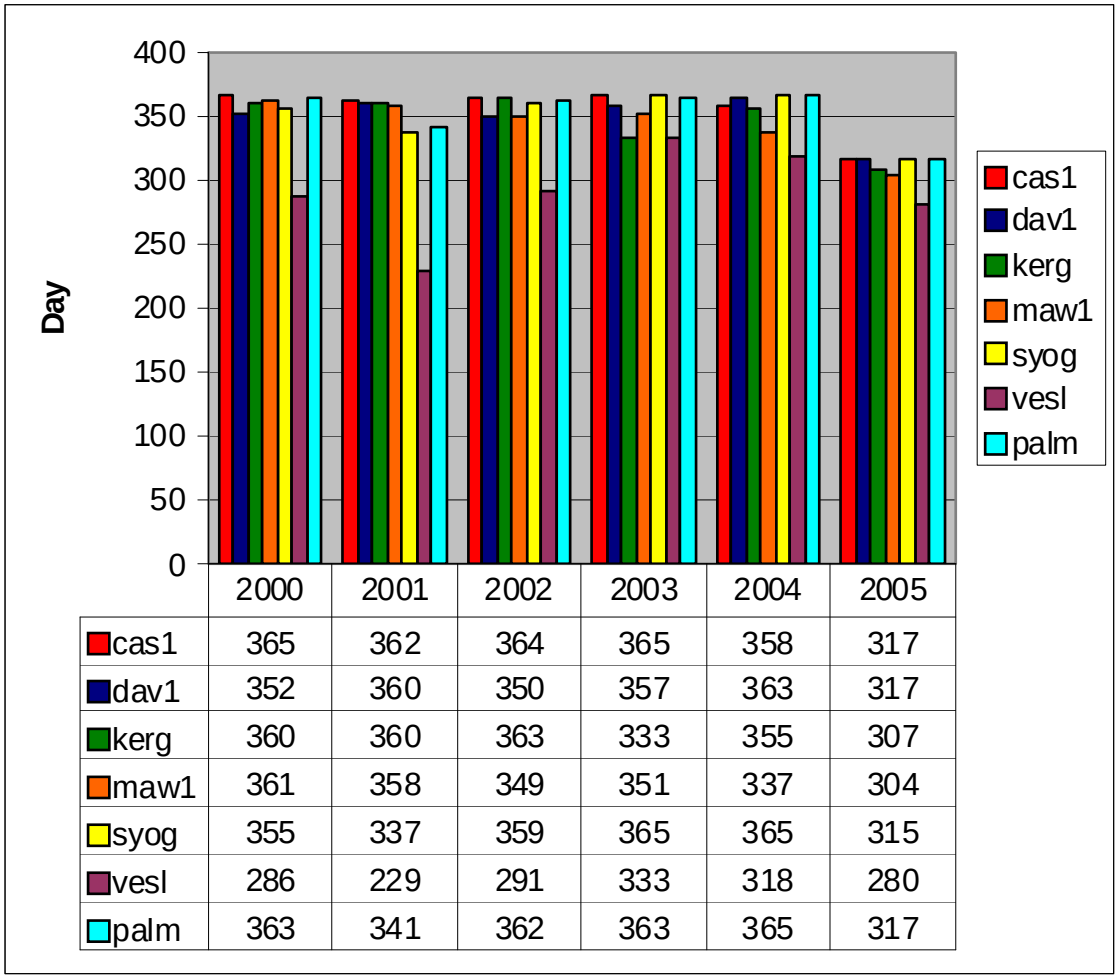

	2000	2001	2002	2003	2004	2005
cas1	365	362	364	365	358	317
dav1	352	360	350	357	363	317
kerg	360	360	363	333	355	307
maw1	361	358	349	351	337	304
syog	355	337	359	365	365	315
vesl	286	229	291	333	318	280
palm	363	341	362	363	365	317

Figure B.1: Data availability for IGS sites in Antarctica.

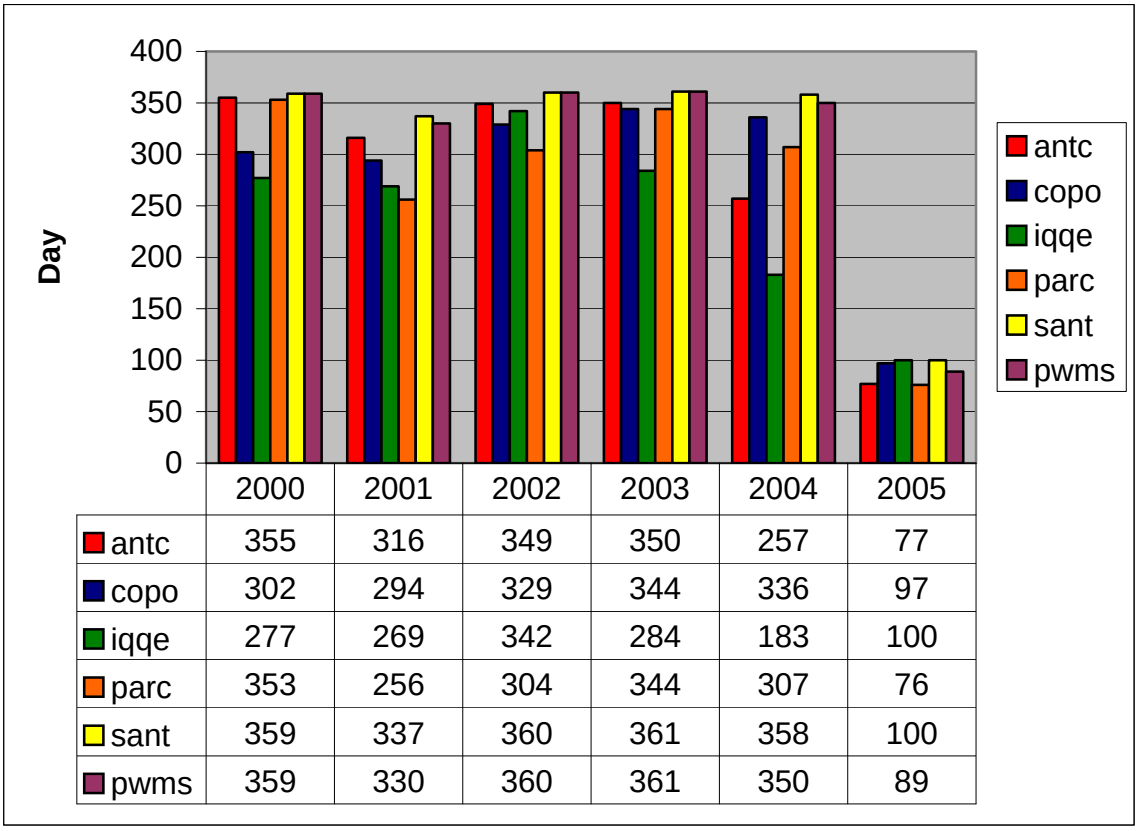

	2000	2001	2002	2003	2004	2005
antc	355	316	349	350	257	77
copo	302	294	329	344	336	97
iqqe	277	269	342	284	183	100
parc	353	256	304	344	307	76
sant	359	337	360	361	358	100
pwms	359	330	360	361	350	89

Figure B.2: Data availability for IGS sites in South America.

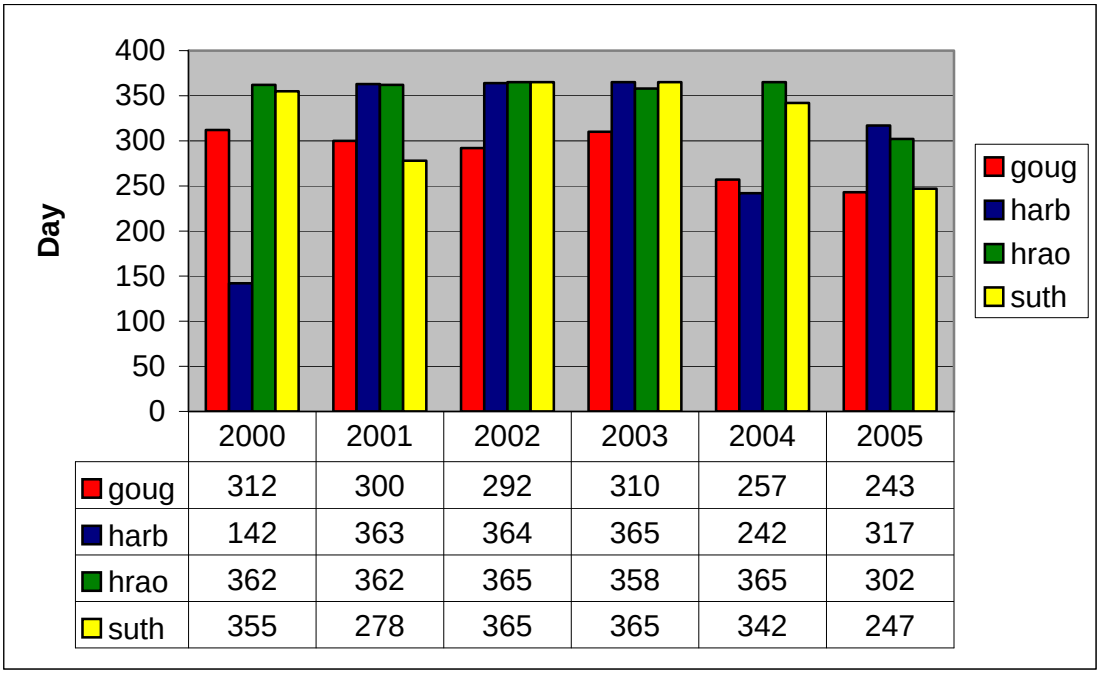

	2000	2001	2002	2003	2004	2005
goug	312	300	292	310	257	243
harb	142	363	364	365	242	317
hrao	362	362	365	358	365	302
suth	355	278	365	365	342	247

Figure B.3: Data availability for IGS sites in Africa.

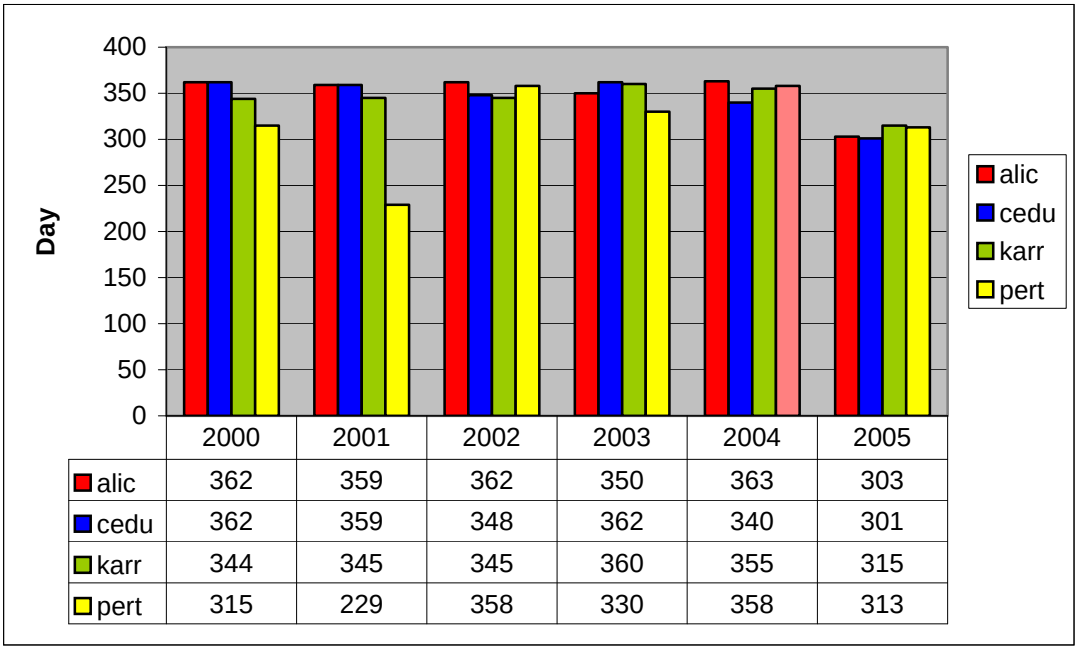

	2000	2001	2002	2003	2004	2005
alic	362	359	362	350	363	303
cedu	362	359	348	362	340	301
karr	344	345	345	360	355	315
pert	315	229	358	330	358	313

Figure B.4: Data availability for IGS sites in Australia.

APPENDIX C

MP1 RMS AND MP2 RMS FOR TAMDEF SITES

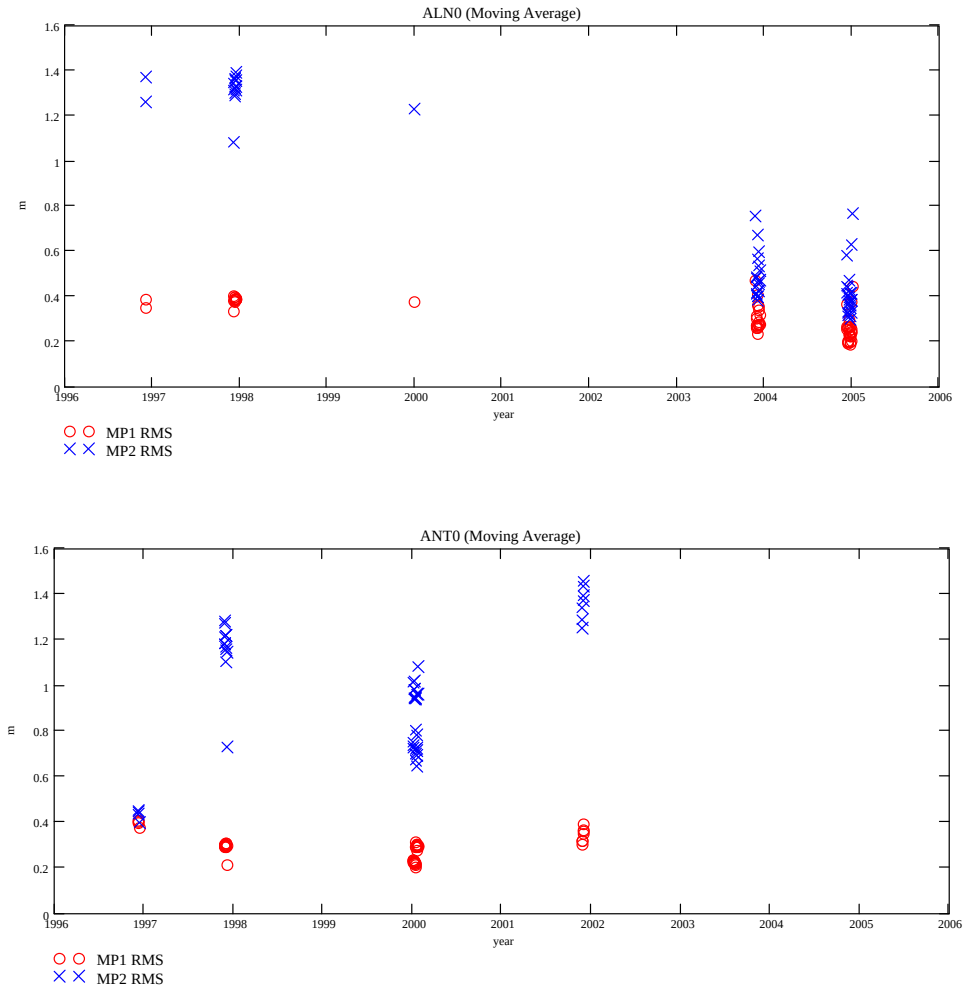

Figure C.1: MP1 RMS and MP2 RMS at the ALN0 and ANT0 sites.

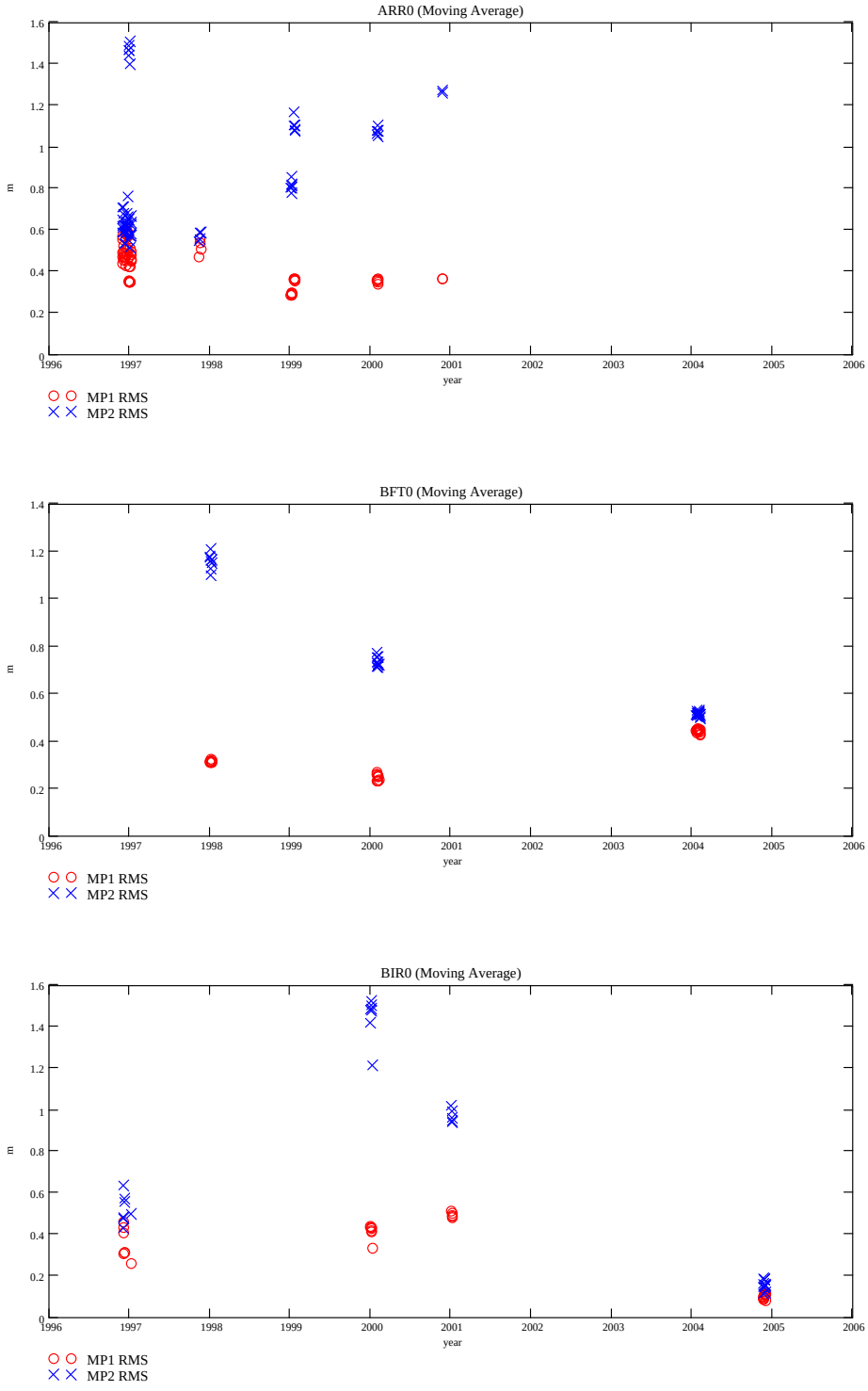

Figure C.2: MP1 RMS and MP2 RMS at the ARR0, BFT0 and BIR0 sites.

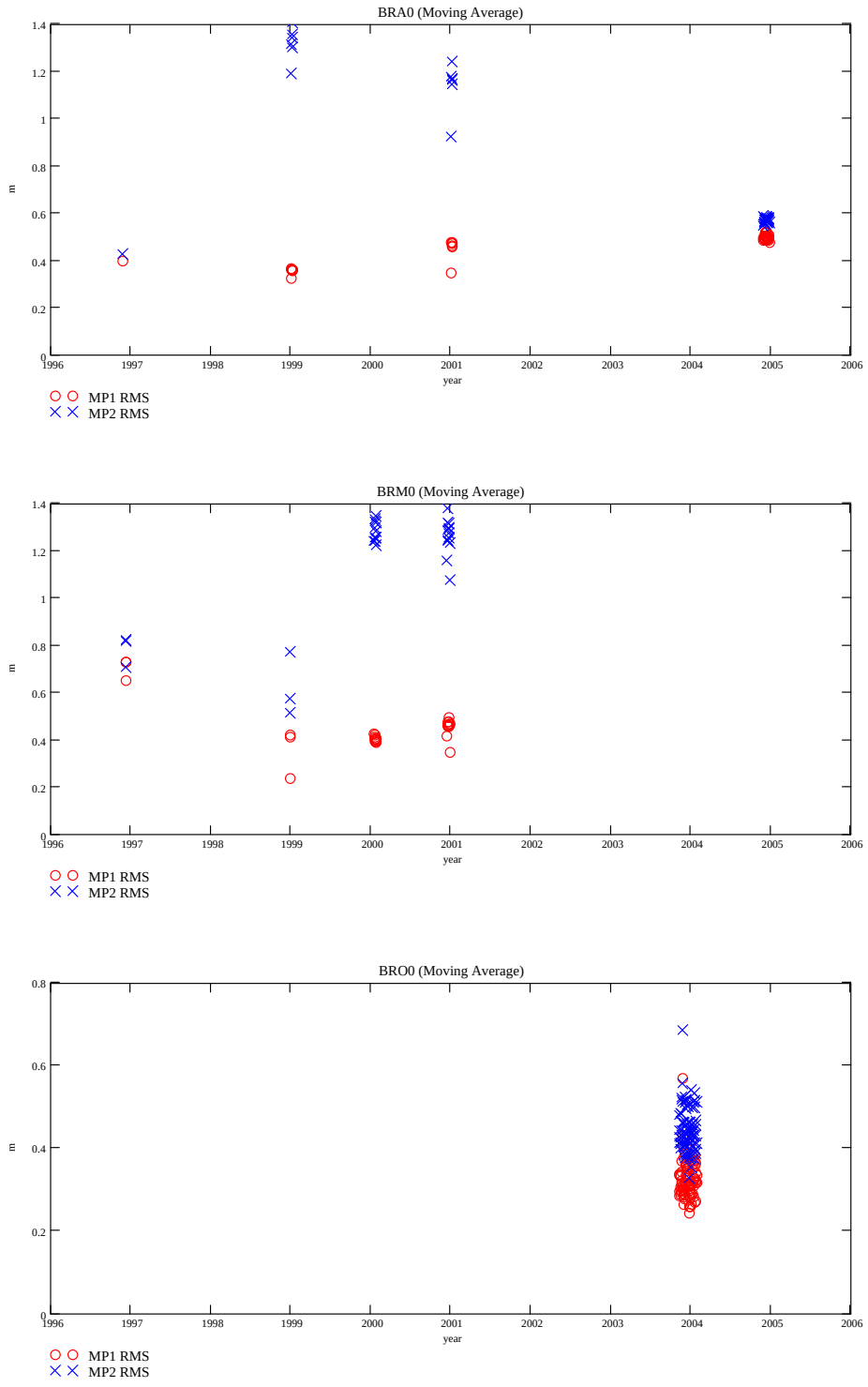

Figure C.3: MP1 RMS and MP2 RMS at the BRA0, BRM0 and BRO0 sites.

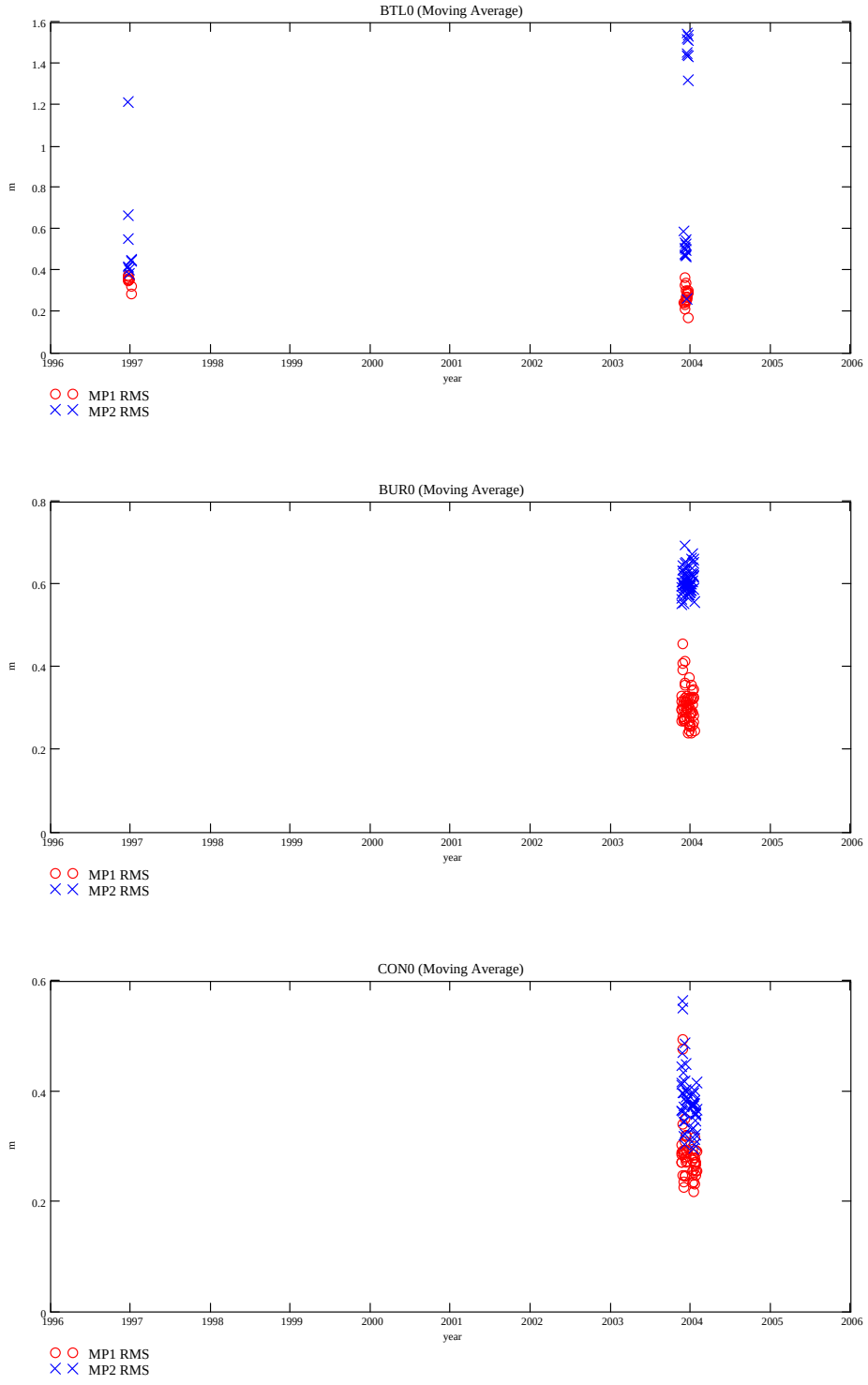

Figure C.4: MP1 RMS and MP2 RMS at the BTL0, BUR0 and CON0 sites.

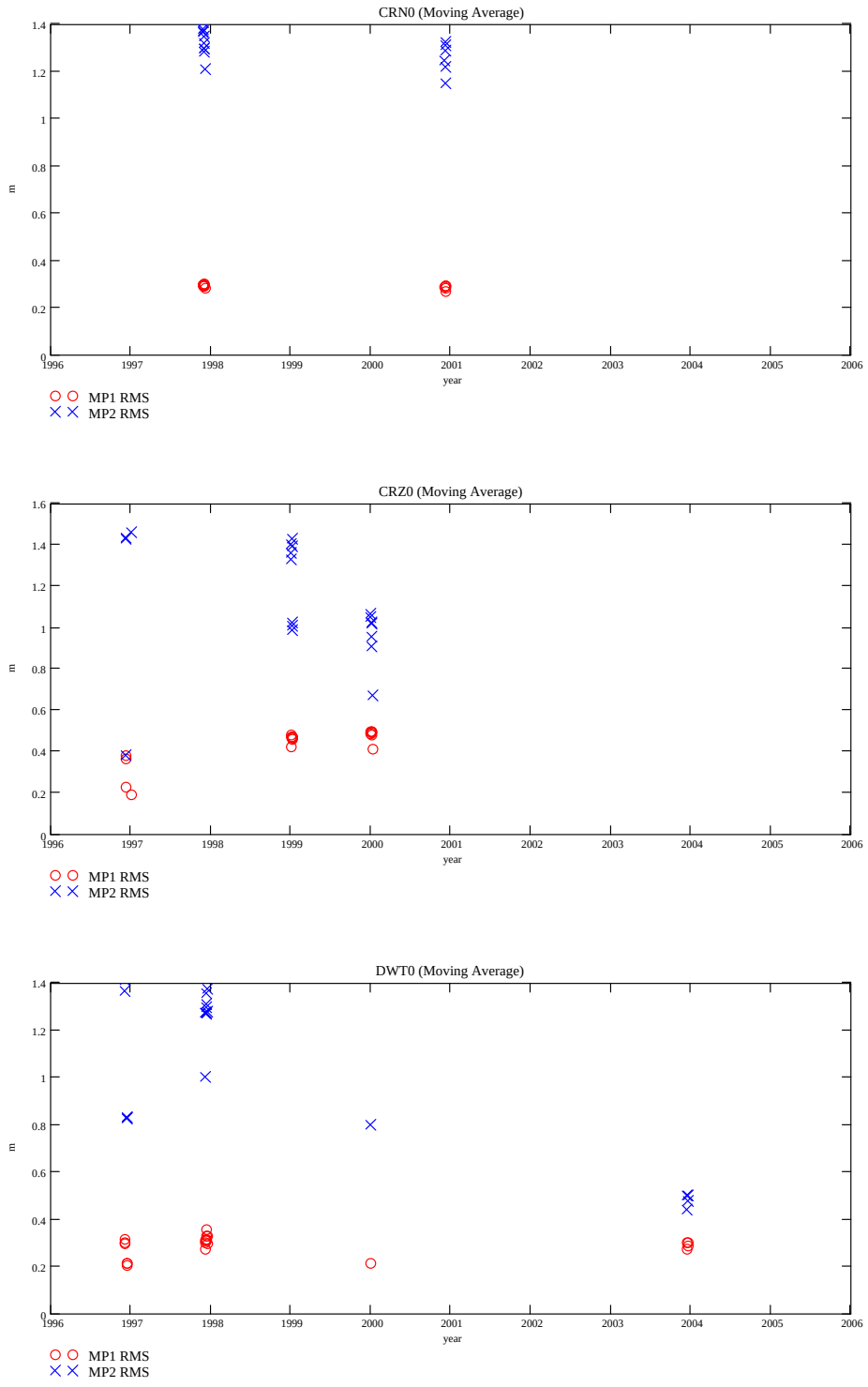

Figure C.5: MP1 RMS and MP2 RMS at the CRN0, CRZ0 and DWT0 sites.

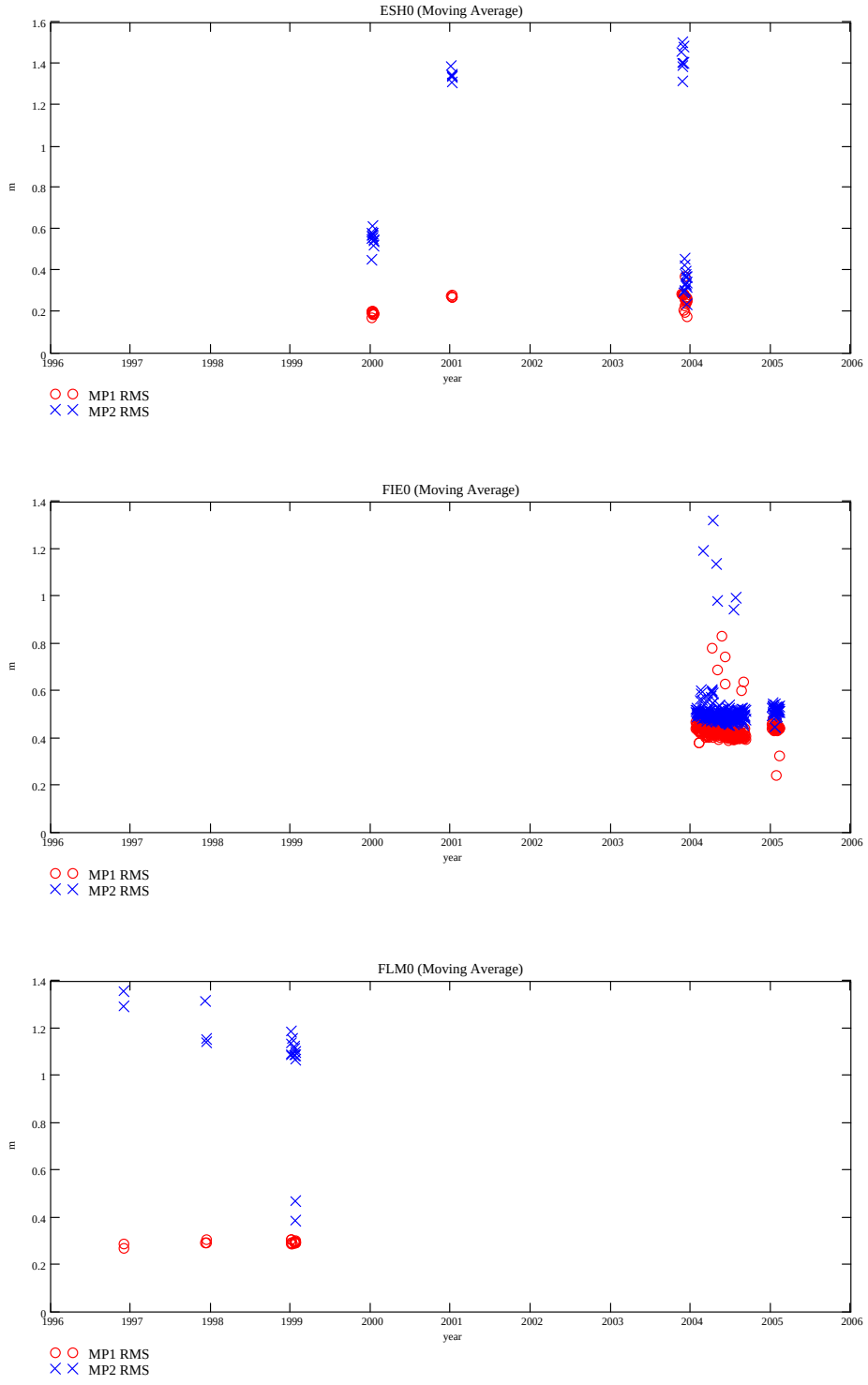

Figure C.6: MP1 RMS and MP2 RMS at the ESH0, FIE0 and FLM0 sites.

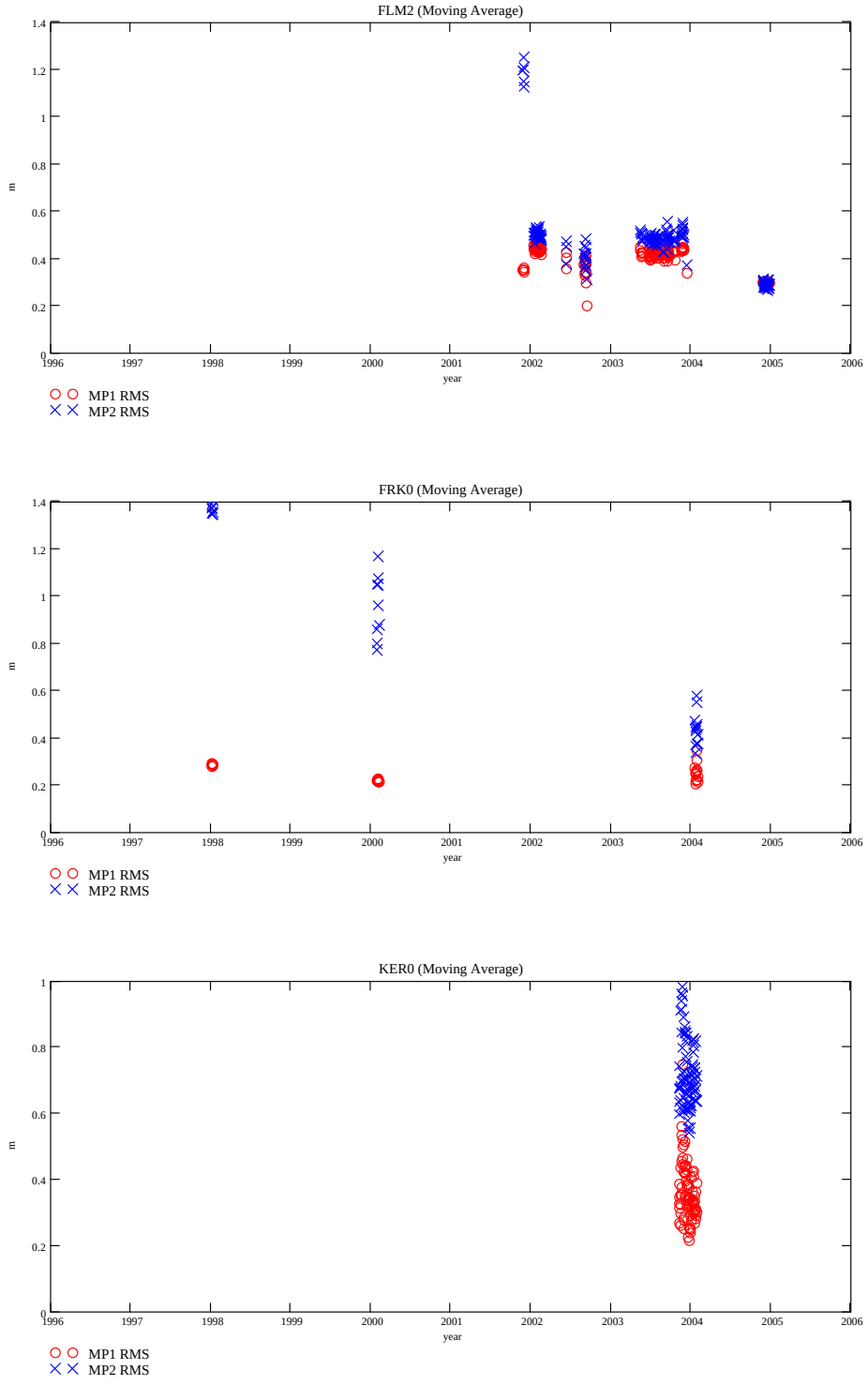

Figure C.7: MP1 RMS and MP2 RMS at the FLM2, FRK0 and KER0 sites.

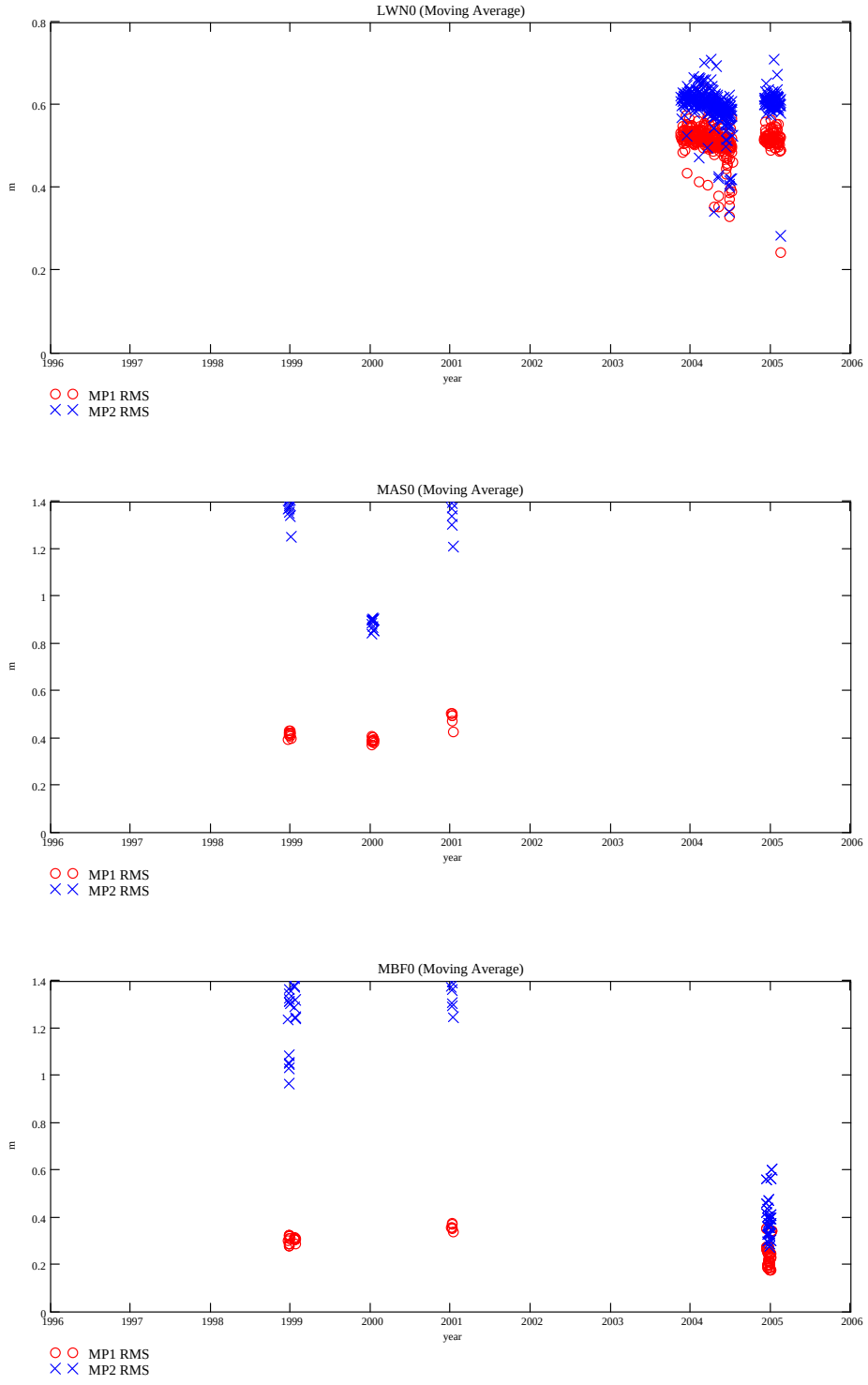

Figure C.8: MP1 RMS and MP2 RMS at the LWN0, MAS0 and MBF0 sites.

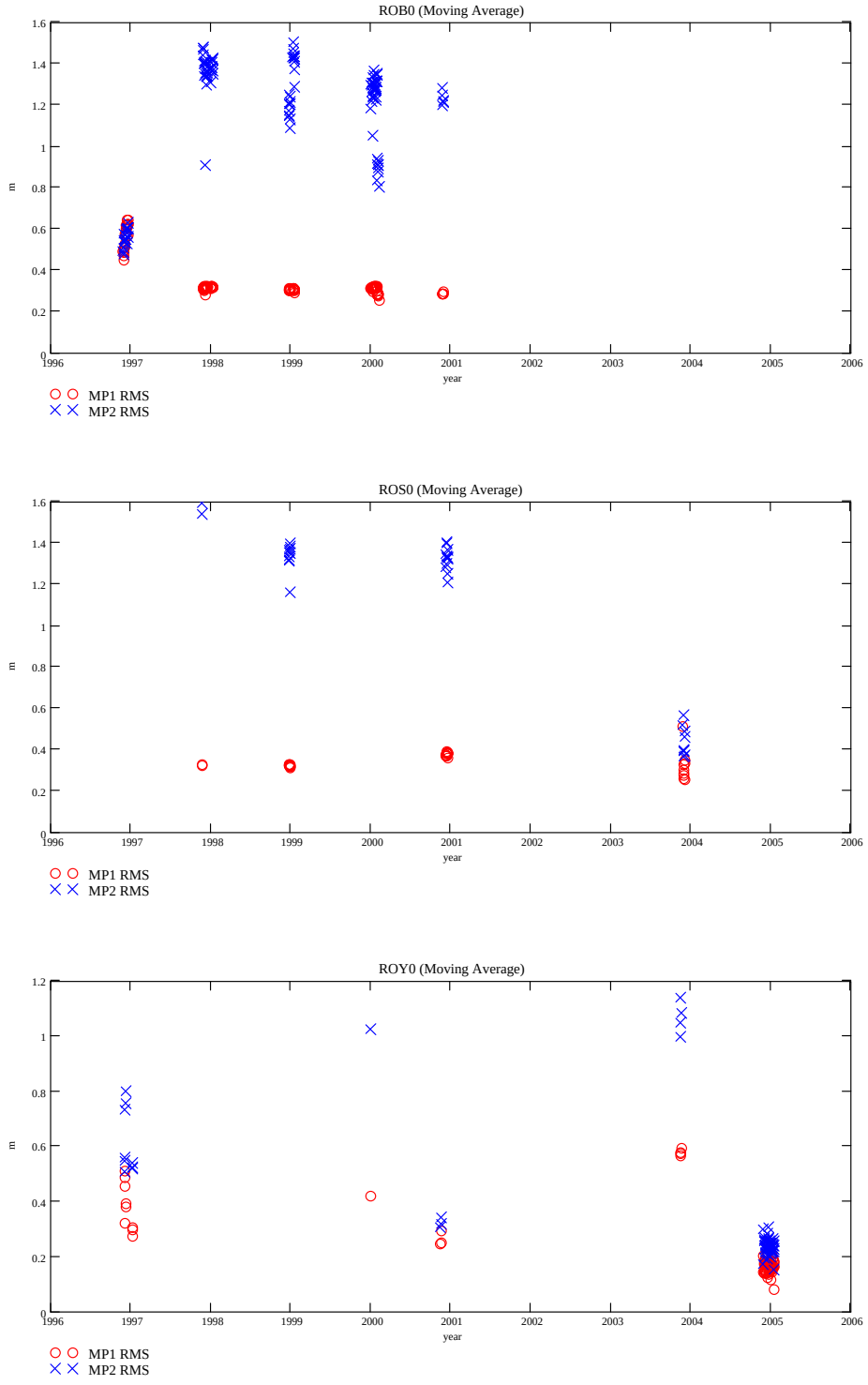

Figure C.9: MP1 RMS and MP2 RMS at the ROB0, ROS0 and ROY0 sites.

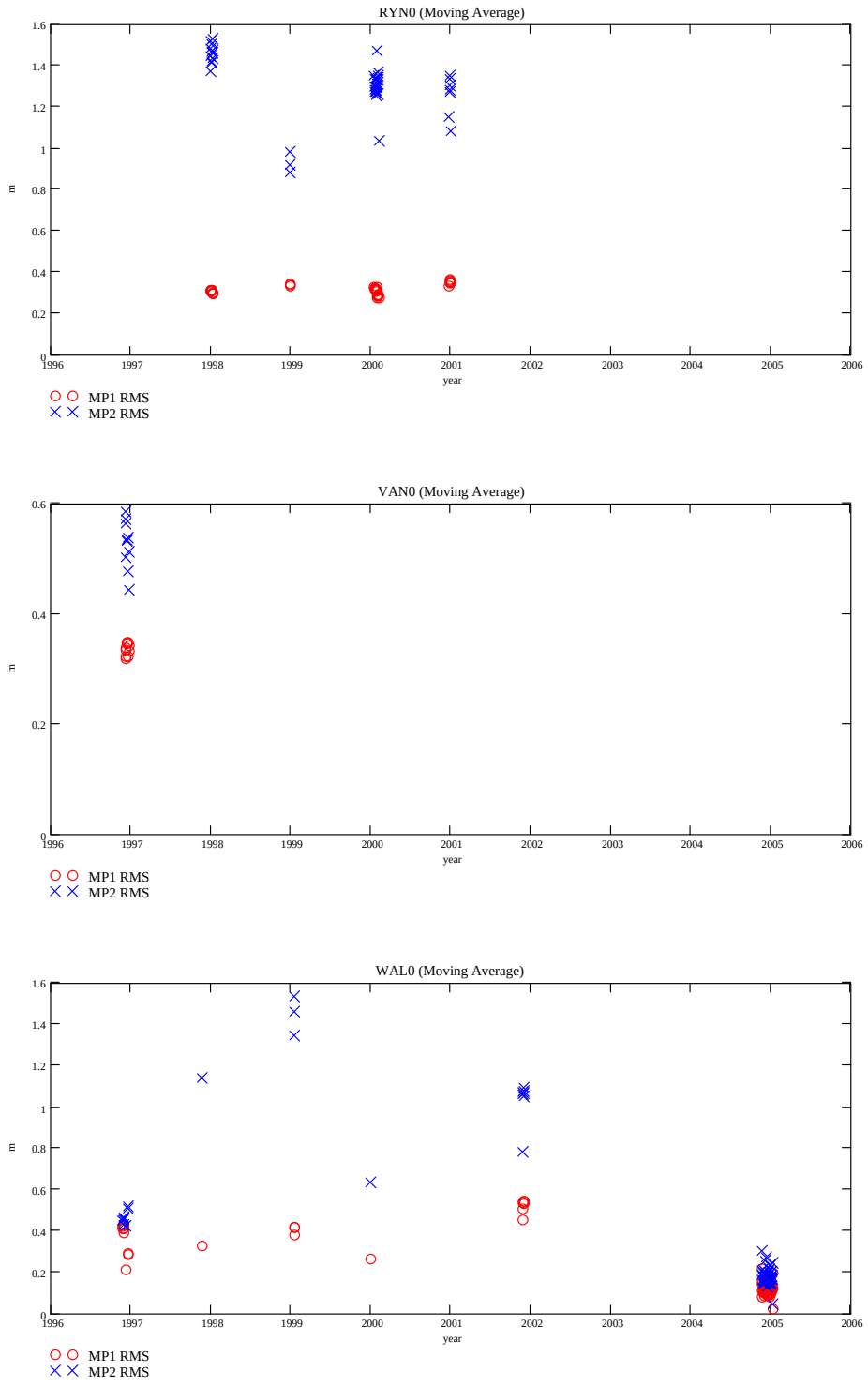

Figure C.10: MP1 RMS and MP2 RMS at the RYN0, VAN0 and WAL0 sites.

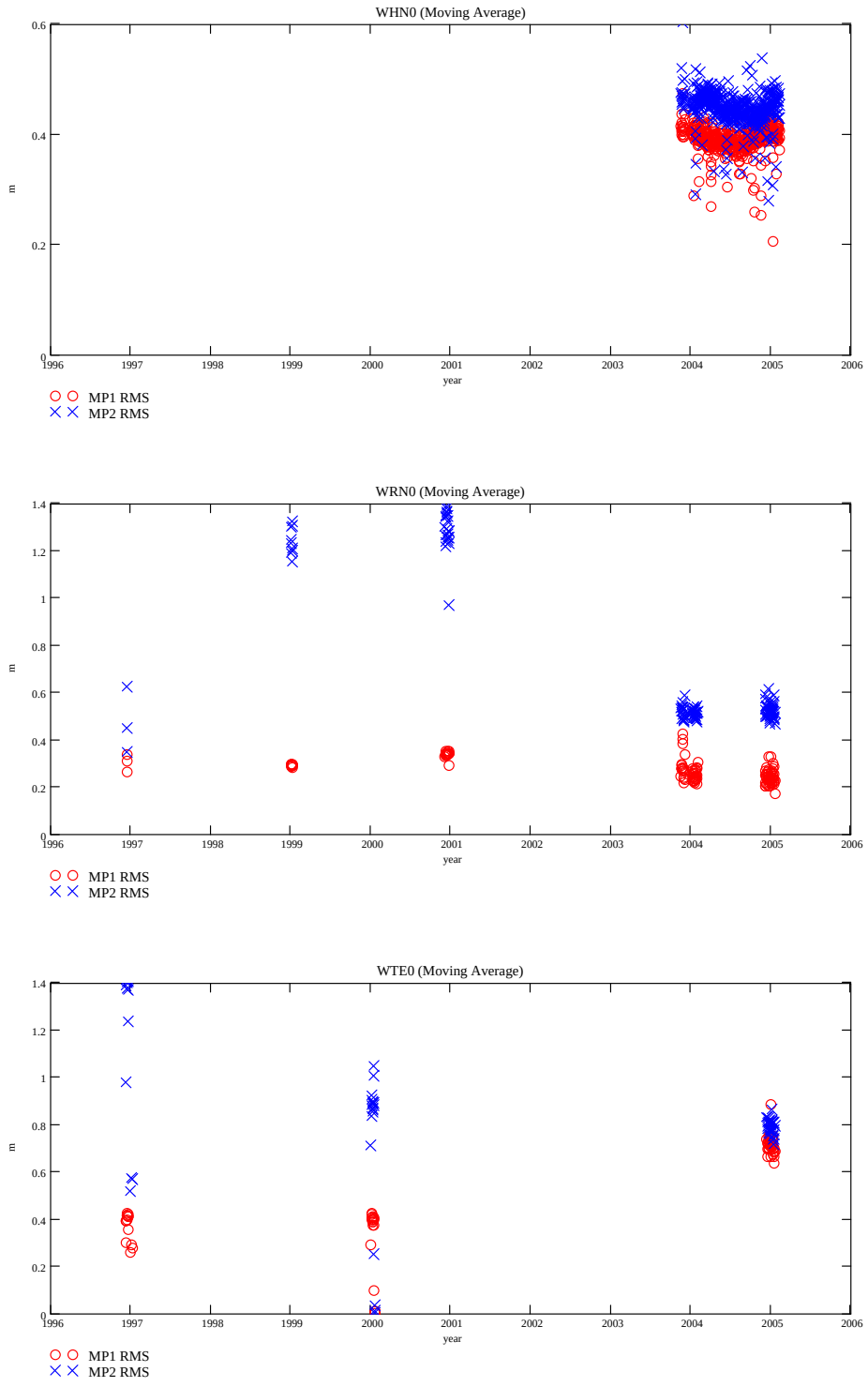

Figure C.11: MP1 RMS and MP2 RMS at the WHN0, WRN0 and WTE0 sites.